EVALUATION OF CURVED SURFACES WITH X-RAY REFLECTOMETRY

by

Jacob A. Cole

A dissertation submitted to the faculty of
The University of North Carolina at Charlotte
in partial fulfillment of the requirements
for the degree of Doctor of Philosophy in
Mechanical Engineering

Charlotte

2022

Approved by:

_____
Dr. Stuart T. Smith

_____
Dr. Chris J. Evans

_____
Dr. Greg Gbur

_____
Dr. Jimmie Miller

_____
Dr. Greg Snyder

ABSTRACT

JACOB A. COLE. Evaluation of curved surfaces with x-ray reflectometry. (Under the direction of DR. STUART T. SMITH)

This dissertation presents a body of work developing novel models and methods for surface evaluation with X-ray reflectometry (XRR). At the time of this work, XRR is a highly used tool for the measurement of flat wafers and laminated semiconductors and surfaces having additional geometric features have not been addressed. Surfaces having mid-spatial frequency features at the scale of several millimeters per cycle and surface having constant curvature are measured with XRR and models are developed to predict the effect of surface roughness on the measurements of these surfaces.

First, a model is developed to investigate the effect that mid-spatial frequency errors have on the X-ray reflectivity of a surface. The model predicts the effect of RMS surface roughness, RMS surface waviness, and the cutoff spatial frequency between the feature bandwidths. Measurements on BK7 glass samples are used to verify the ability to simultaneously measure RMS surface roughness at spatial wavelengths less than 16 μm within 0.5 nm of AFM measurements and within 1.1 nm of surface profilometry measurements and the RMS surface waviness at spatial wavelengths greater than 16 μm and less than 4 mm within 7.0 nm of Fizeau interferometry and surface profilometry measurements. The result of this development is to extend the use case of X-ray reflectometry to include the measurement of longer-range surface waviness.

Additionally, a comprehensive model for the evaluation of surface roughness of curved surfaces is presented. This work explores X-ray reflectometry as a technique for measuring the surface roughness of cylinders and spheres as well as the surface roughness of the inner surface of hollow cylinders and spherical shells. Measurements are presented on polished Silicon wafers having different surface roughness as mea-

sured by AFM that are bent to various radii to verify the ability of this model to predict the surface roughness of the curved surface. XRR RMS surface roughness measurement results from Silicon wafers bent between 1.5 and 2.5 m deviate less than 1.1 nm from AFM measurements.

ACKNOWLEDGEMENTS

I would like to thank my advisor Dr. Stuart Smith for his mentorship, patience, and guidance during this work without which many of the solutions in this dissertation would not have existed. A special thank you to my wife and son for their motivation and support. Additional thanks to my committee members for their time and assistance; especially Dr. Jimmie Miller for his assistance with many AFM measurements. I would also like to thank Jennifer Chastain for her administrative support and attention to detail, Brian Dutterer and the UNCC machine shop for assistance with experimental set-up and fixturing, and many thanks to the resources and individuals at Lawrence Livermore National Laboratory and the Advanced Light Source including Jefferson Cuadra, Aditya Mohan, and Dula Parkinson. Finally, I would like to thank the Materials Engineering Division at Lawrence Livermore National Laboratory for the financial support and resources that made this work possible.

TABLE OF CONTENTS

LIST OF TABLES

LIST OF FIGURES

CHAPTER 1: INTRODUCTION

1.1 Research Objectives and Outline

The main objective of this work is to expand the types of surfaces and surface geometries measurable with X-ray reflectometry.

First, based on a model of a surface as a distribution of surface slopes, the effect of surface features of distinct spatial wavelengths on X-ray reflectivity is developed and validated with experiments at the Advanced Light Source at Berkeley National Laboratory [3].

Additionally, theoretical models for reflectivity from curved external and internal surfaces are presented for the extraction of surface roughness. This model can be used for the reversal of radiographs to extract internal and external surface features from spheres and cylinders. Experiments conducted on incrementally bent wafers provide results for a comparative study.

This opening chapter provides the necessary theoretical background in the form of a historical review of the major advances in the field of X-ray reflectivity. Additionally, relevant concepts, definitions, and their mathematical formulation are addressed to provide the foundation for subsequent chapters.

1.2 A History of X-Ray Reflectometry

The discovery of X-rays by Wilhelm Conrad Röntgen on 8 November 1895 instantly revolutionized the fields of medicine and physics. In February of the following year, the first radiographs of a wrist fracture were made by Edwin Brant Frost in Dartmouth, MA [4]. A radiograph taken by Röntgen is shown in Figure 1.1.

Despite the excitement around this new type of radiation, Röntgen did not believe

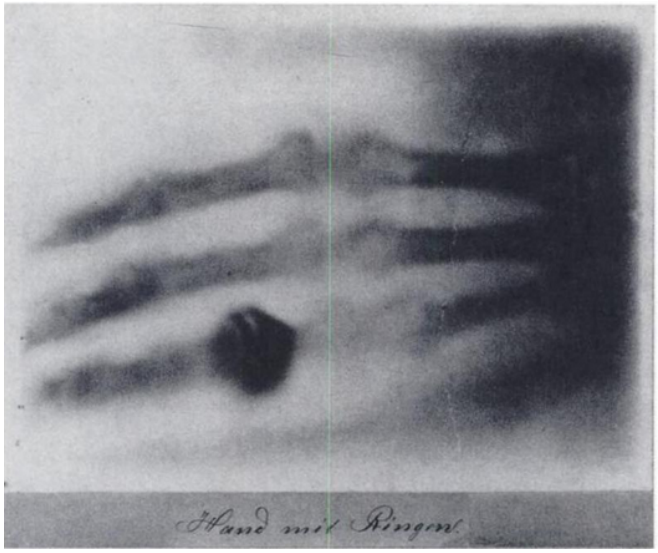

Figure 1.1: Radiograph taken by Wilhelm Röntgen of his wife Anna's hand, December 1895 [1].

that reflections of X-rays were possible [5], stating

> ...the conclusion is reached that there is, as before remarked, no regular reflection, but that the bodies behave toward X-rays in the same matter as a turbid medium with no reference to light.

Partly due to this stance, the topic of X-ray reflectivity remained absent until Compton [6] in 1923 ascertained that the index of refraction for X-rays is less than one (for most light, the index of refraction is greater than one, allowing for, for example, total internal reflection in fiber optics). With this information, it was postulated that the X-rays would experience total external reflection from a smooth surface. In 1928, Compton's theory was experimentally proven when Prins [2] measured some of the first rocking curves, reflectivity curves, and total external reflections as functions of incident angle of iron samples. The experimental setup for these measurements is shown in Figure 1.2.

From there, work continued resulting in an abundance of theory among which was evidence that X-ray reflection and refraction was consistent with the general Fresnel equations for light [7]. Kiessig [8] made many measurements of the reflection of X-rays

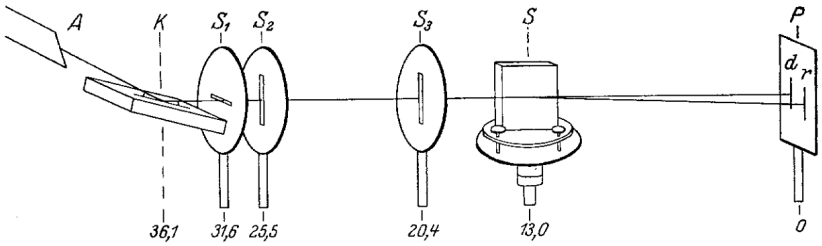

Fig. 6. Apparatur (Methode B) zur Aufnahme der Totalreflexion spektral zerlegter kontinuierlicher Strahlung.

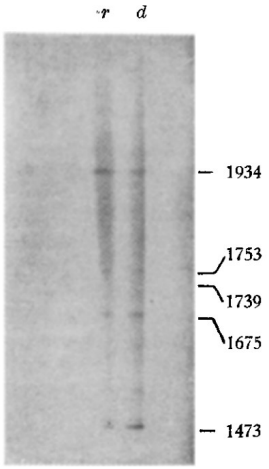

Fig. 8.

Figure 1.2: (left) J. A. Prins [2] experimental setup for measuring the first reflections of X-rays and (right) the recorded reflections from a steel mirror. The incident (direct) beam is labeled d and the reflected beam is labeled r. The labeled lines are the X-ray transition wavelengths associated with Fe$K\beta_1$ (1753), FeK-edge (1739), WLl (1675), and W$L\alpha$ (1473).

from thin nickel films evaporated on glass which resulted in the discovery of "Kiessig fringes" allowing for the measurement of thin film thickness, a vital measurement technique in semiconductor manufacturing [9,10]. In 1954, Parratt [11] published pivotal work on measurements on the reflection of X-rays from oxidation layers on copper films. These oxidation layers were porous which lead to a reduction of density at the surface as the layers grew which would change the shape of the reflectivity curve. This connection between surface density and reflectivity opened an enormous amount of work on surface density distribution and its effects on reflectivity and transmission of X-rays with the most dramatic of these effects being asymmetric reflections on either side of the specular peak known as Yoneda wings [12]. The theoretical foundation for the analysis of this off-specular reflection (subsequently named diffuse scatter) was developed in 1972 by Croce et al. [13]. With the development of neutron reflectometers and the emergence of second and third generation synchrotrons, the late 1980's and 1990's brought about a large number of studies using X-ray and neutron reflection [14–30].

With the theoretical foundation for the measurement of smooth, thin multilayers being mostly complete, X-ray reflectometry has been used extensively in the semiconductor manufacturing industry for the last three decades. During this time, the literature remained relatively unchanged. The use of multipixel detectors with scintillating crystals has seen, lately, a rise in the number of studies aimed at "quick" X-ray reflectometry (qXRR); a new method of X-ray reflectometry used to study fast processes. This method requires fast collection of reflectivity than traditional scanning-type XRR [31–35]. This method uses the geometry of surfaces, typically curved mirrors of several 100's to 1000's of meters in radius, to capture the entire reflectivity curve in one image. Fast data collection enables the measurement of time varying chemical, thermal, and mechanical changes to the surface or interfaces of materials.

1.3 Definitions and General Principles

To understand the models developed in this thesis it is important to first define the parameters used and the foundational principles for predicting the reflection of X-rays. A plane wave of one frequency (monochromatic) is typically written with the equation

$$\psi = a \exp(i\mathbf{k} \cdot \mathbf{r}), \tag{1.1}$$

where $\mathbf{k}$ is the wave vector (in radians per meter) and $\mathbf{r}$ is the position vector (in meters) of the wave. In a scattering event, the transfer of momentum is given by the *wave vector transfer* or *scattering vector*,

$$\mathbf{q} = \mathbf{k}_0' - \mathbf{k}_0, \tag{1.2}$$

usually expressed in Å^{-1}. The wave vectors for a typical scattering event are depicted in Figure 1.3.

The index of refraction n for a material changes with the frequency of the light.

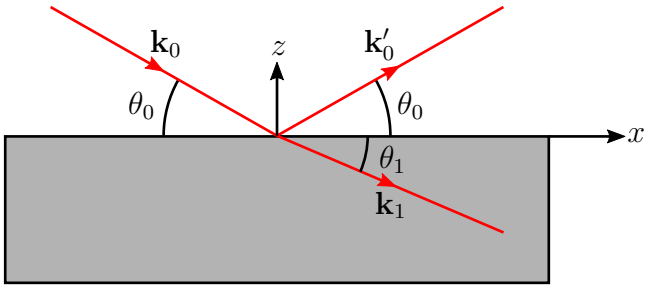

Figure 1.3: Light will change direction at an interface. Continuity of the wave and its derivative at the interface is the basis for the derivation of Snell's law and the Fresnel coefficients.

For frequencies of light that are lower than the resonant frequency of the electronic transitions of the atoms in a material, the index of refraction increases with frequency (e.g. blue light refracts more than red light). The index of refraction begins to decrease with frequency immediately above the resonance and decreases more with every resonance passed. X-ray frequencies are typically higher than all of the transition frequencies; thus, the index of refraction for X-rays is *less* than unity. The phase velocity c/n therefore is greater than the speed of light; however, the group velocity $d\omega/dk$ is still less than c.

For X-ray frequencies, the index of refraction can be written as

$$n = 1 - \delta, \tag{1.3}$$

where the deviation of the index of refraction from unity is called the unit decrement δ and is very small; on the order of 10^{-5}. The result of an index of refraction less than one is a phenomenon called *total external reflection* where, for incident angles less than a critical angle θ_c, the wave will no longer penetrate into the medium and will instead propagate along the surface as a so-called *evanescent wave*. The amplitude of the evanescent wave depends on the phase difference between the incident and

reflected wave and becomes almost twice that of the incident wave when the incident and reflected waves are in phase at $\theta_0 \approx \theta_c$. The X-ray properties for some common materials are tabulated in Table 1.1.

Table 1.1: X-ray properties of selected elements at 10 keV (1.2398 Å).

	Z	Mass Density (kg/m^3)	Dispersion δ	Absorption β	Critical Angle θ_c
Si	14	2330	4.8889×10^{-6}	7.3544×10^{-8}	0.179° [3.12 mrad]
W	74	19250	2.7946×10^{-5}	1.7778×10^{-6}	0.428° [7.47 mrad]
Ir	77	22560	3.4163×10^{-5}	2.3386×10^{-6}	0.474° [8.27 mrad]
Au	79	19300	2.9912×10^{-5}	2.2073×10^{-6}	0.443° [7.73 mrad]

X-rays transmitted into a material will undergo *photoelectric absorption*; X-ray photons are absorbed by atoms in the material and the excess energy is transferred to an electron which is subsequently ejected from the atom, leaving it ionized. This absorption will attenuate the amplitude of the X-rays by a factor $e^{-\mu z/2}$ where z is the distance travelled through the material and μ is called the absorption coefficient. Inside of the medium, the wave vector is $n\mathrm{k}$ and, allowing the index of refraction to be complex

$$n = 1 - \delta - i\beta, \tag{1.4}$$

the wave equation becomes

$$\exp(in\mathrm{k}z) = \exp(i(1-\delta)\mathrm{k}z)\,\exp(-\beta\mathrm{k}z). \tag{1.5}$$

From above it can be inferred that $\beta\mathrm{k} = \mu/2$; therefore,

$$\beta = \frac{\mu}{2\mathrm{k}}. \tag{1.6}$$

β is referred to as the coefficient of absorption and is typically in the range of 10^{-8}, depending on the electron density of the material.

At a penetration distance $z = (2\beta \mathrm{k})^{-1}$, the intensity is reduced to $1/e$. This distance is typically referred to as the *attenuation length*. For X-rays having energy of 10 keV incident upon Silicon, using the values in Table 1.1, the attenuation length is approximately 134 μm.

1.4 Snell's Law and the Fresnel Equations

Light propagating through a medium will change direction when it enters another medium. This change in direction, depicted in Figure 1.4, is described quantitatively by Snell's law.

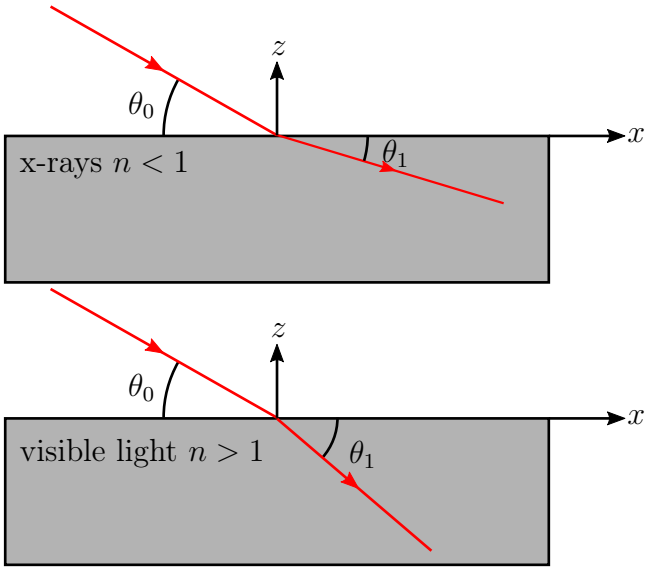

Figure 1.4: The index of refraction indicates the amount the light will be refracted by an interface. For visible light, the index of refraction is greater than 1 (typically 1.2 - 2); for X-rays, the index of refraction is less than 1. The result of this difference is that X-rays will refract at a smaller angle than incidence.

For an interface, the boundary conditions require that the light wave is continuous at the interface, i.e. the sum of the transmitted (a_1) and reflected (a_0') amplitudes must equal the incident amplitude (a_0). This relationship can be written as

$$a_0 = -a_0' + a_1. \tag{1.7}$$

Additionally, taking the condition that the derivative of the wave at the interface must also be continuous; remembering that the wave equations are

$$\psi_0 = a_0 \exp\left(i\mathbf{k}_0 \cdot \mathbf{r}\right) \tag{1.8}$$

$$\psi_0' = a_0' \exp\left(i\mathbf{k}_0' \cdot \mathbf{r}\right) \tag{1.9}$$

$$\psi_1 = a_1 \exp\left(i\mathbf{k}_1 \cdot \mathbf{r}\right), \tag{1.10}$$

the relationship between the derivatives is

$$a_0\mathbf{k}_0 = -a_0'\mathbf{k}_o' + a_1\mathbf{k}_1. \tag{1.11}$$

The wavelength of the light does not change at the interface; therefore, the wave vector for the two materials is

$$|\mathbf{k}_0| = |\mathbf{k}_0'| = n_0 k \tag{1.12}$$

$$|\mathbf{k}_1| = n_1 k; \tag{1.13}$$

thus, the x-component (parallel to the interface) can be written, using Equation 1.7, to derive Snell's law

$$\begin{aligned}(a_0 + a_0')n_0 k\cos\theta_0 &= a_1 n_1 k\cos\theta_1 \\ n_0\cos\theta_0 &= n_1\cos\theta_1.\end{aligned} \tag{1.14}$$

The critical angle is the angle for which the reflected X-rays are parallel to the surface ($\theta_1 = 0$). Using Equation 1.14,

$$n_0\cos\theta_c = n_1. \tag{1.15}$$

Using the index of refraction for the material $n_1 = 1 - \delta$ and assuming that $n_0 \approx 1$,

$$\cos\theta_c = 1 - \delta. \tag{1.16}$$

The critical angle for a material is small (typically less than 1°); therefore it can be approximated to be

$$\theta_c \approx \sqrt{2\delta}. \tag{1.17}$$

The z-component (perpendicular to the interface) of the wave vector is

$$(a_0 - a_0')n_0 \sin\theta_0 = a_1 n_1 \sin\theta_1. \tag{1.18}$$

Rearranging Equation 1.7,

$$a_1 = a_0 + a_0'; \tag{1.19}$$

therefore,

$$\frac{a_0 - a_0'}{a_0 + a_0'} = \frac{n_1 \sin\theta_1}{n_0 \sin\theta_0}. \tag{1.20}$$

This can be re-written to solve for the Fresnel equations of the reflected and transmitted amplitudes;

$$r = \frac{a_0'}{a_0} = \frac{n_0 \sin\theta_0 - n_1 \sin\theta_1}{n_0 \sin\theta_0 + n_1 \sin\theta_1} \tag{1.21}$$

$$t = \frac{a_1}{a_0} = \frac{2n_0 \sin\theta_0}{n_0 \sin\theta_0 + n_1 \sin\theta_1}. \tag{1.22}$$

These Fresnel equations form the geometric basis for the natural reduction of reflectivity as a function of incident angle and are used as the framework for the models presented in the following chapter. Chapters 3 and 4 expand upon these models for the application to non-planar surfaces.

CHAPTER 2: X-RAY INTERACTION WITH MATTER

The theory developed in the previous Chapter is used below to address the effect of interface interactions between X-rays and material. In particular, the influence of interface roughness and stratified layers is presented.

2.1 Reflection from a Homogeneous Slab

When X-rays are incident upon a surface at small angles above the critical angle, there are two major types of scatter; shown in Figure 2.1. One can observe specular reflections or diffuse (off-specular) scatter; the ratio of specular to diffuse scatter will give an indication of the surface texture as rough surfaces will have more diffuse scatter than smooth surfaces. For a single, homogeneous slab, X-rays will interact with the interface as shown in the previous section.

For samples of finite thickness or multiple layers, there will be interference between specular scatter from the top surface and specular scatter from subsequent interfaces (layers). Models for determining these interactions as well as the influence of surface roughness are developed in this chapter.

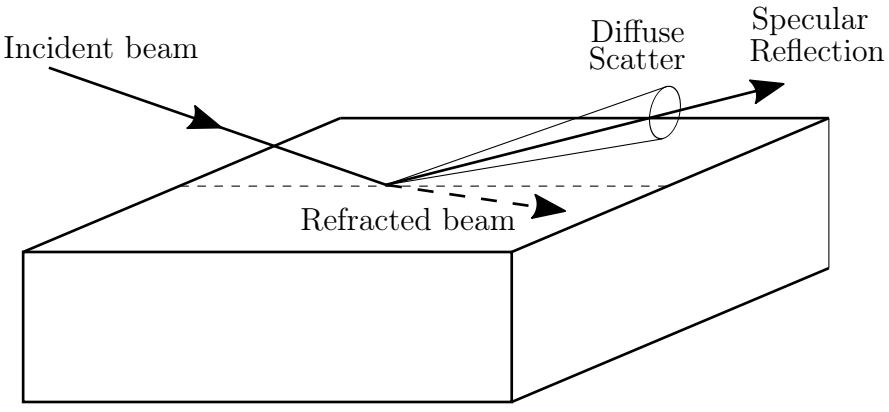

Figure 2.1: Diagram of the diffraction processes in X-ray reflectivity.

2.2 Reflection from Multilayers

For a single plate of homogeneous material and finite thickness Δ, there will be an infinite number of reflections from the top and bottom surfaces; this will create a kind-of Fabry-Pérot cavity between the interfaces. The first three of these reflections are shown in Figure 2.2 can be summarized:

1. A reflection off of the top interface r_{01},

2. A transmission into the plate t_{01}, reflection at the bottom of the plate r_{12}, then a transmission through the top of the plate t_{10}. There will be a phase difference $\varphi = \exp\left(i\left(\mathbf{k}\cdot\mathbf{\Delta}_0\right)\right)\exp(i2\mathrm{k}_1\sin\theta_1\Delta_0)$ between the exiting X-rays in this case and the X-rays reflected from the interface in the previous case,

3. A transmission into the plate t_{01}, a reflection off of the bottom of the plate r_{12}, a reflection at the top back into the plate r_{10}, a second reflection off of the bottom of the plate r_{12}, and finally a transmission through the top of the plate t_{10}. As twice the distance was travelled, there will be twice the phase change in this case as the previous case.

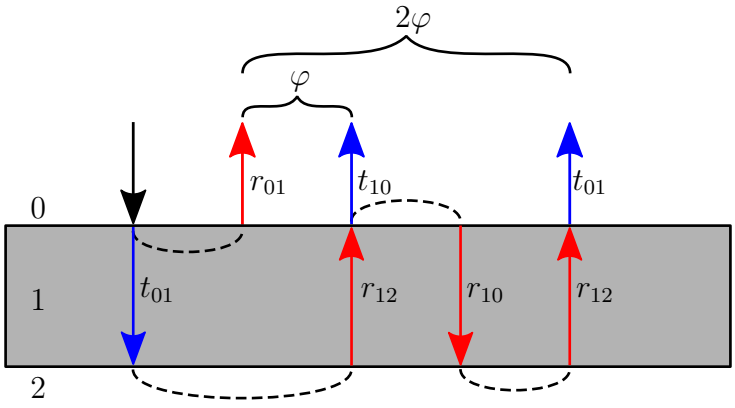

Figure 2.2: Diagram of the first three reflections in a multilayer reflection scenario. The outgoing X-rays will have a phase difference $n\varphi$ depending on the total distance travelled. Dashed lines indicate continuity of the ray through a reflection.

The total reflectivity of the plate is the sum of all of the reflections and is therefore

$$\begin{aligned} r_{total} &= r_{01} + t_{01}r_{12}t_{10}\varphi + t_{01}r_{12}r_{10}r_{12}t_{10}\varphi^2 + \cdots \\ &= r_{01} + t_{01}r_{12}t_{10}\varphi \sum_{j=1}^{\infty} \left(r_{10}r_{12}\varphi\right)^j. \end{aligned} \tag{2.1}$$

Using the identity

$$\sum_{j=1}^{\infty} x^j = \frac{1}{1-x}, \tag{2.2}$$

the total reflectivity of the plate becomes

$$r_{total} = r_{01} + t_{01}r_{12}t_{10}\varphi \frac{1}{1 - r_{10}r_{12}\varphi}. \tag{2.3}$$

Recalling that, from Equation 1.22, for small angles,

$$r_{01} = \frac{n_0\theta_0 - n_1\theta_1}{n_0\theta_0 + n_1\theta_1} = -r_{10}, \tag{2.4}$$

and

$$r_{01}^2 + t_{01}t_{10} = \frac{(n_0\theta_0 - n_1\theta_1)^2}{(n_0\theta_0 + n_1\theta_1)^2} + \frac{4n_0\theta_0 n_1\theta_1}{(n_0\theta_0 + n_1\theta_1)^2} = 1. \tag{2.5}$$

Hence Equation 2.3 can be simplified to

$$\begin{aligned} r_{total} &= \frac{r_{01} - r_{01}r_{10}r_{12}\varphi + t_{01}r_{12}t_{10}\varphi}{1 - r_{10}r_{12}\varphi} \\ &= \frac{r_{01} + r_{12}\varphi}{1 + r_{01}r_{12}\varphi}. \end{aligned} \tag{2.6}$$

The method for extending this formalism to a slab of N layers was first introduced by Parratt [11]. Here the n-th layer is directly on top of an infinitely thick slab and each layer has refractive index $n_j = 1 - \delta_j + \beta_j$ and thickness Δ_j.

Ignoring multiple reflections, the reflectivity of each layer is

$$r_{j,j+1} = \frac{n_j\theta_j - n_{j+1}\theta_{j+1}}{n_j\theta_j + n_{j+1}\theta_{j+1}}, \tag{2.7}$$

where $\theta_j = \sqrt{2\left(1 - \frac{n_j}{n_{j+1}}\right)}$. For the n-th layer, there will be no multiple reflections and thus the reflectivity is

$$r_{N,\infty} = \frac{n_N\theta_N - n_\infty\theta_\infty}{n_N\theta_N + n_\infty\theta_\infty}. \tag{2.8}$$

The reflectivity of the layer on top of the n-th layer is

$$r_{N-1,N} = \frac{r_{N-1,N} + r_{N,\infty}\varphi_N}{1 + r_{N-1,N}r_{N,\infty}\varphi_N}, \tag{2.9}$$

where $\varphi_j = \exp(2xk_j \sin\theta_j\Delta_N)$. This process can be repeated recursively until the total reflectivity is obtained. Figure 2.3 shows a plot of the calculated reflectivity for an Iridium/Silicon multilayer having 10 bilayers each being 1 nm Iridium and 4 nm Silicon illuminated by a 10 keV X-ray source. The material parameters are taken from Table 1.1 in Chapter 1. Figure 2.4 depicts how surface roughness, density, and layer thickness effect the reflectivity curve of a multilayer. Layer thickness will spread the fringes, surface density will increase the depth of the valleys, and surface roughness will increase the decay rate of the reflectivity.

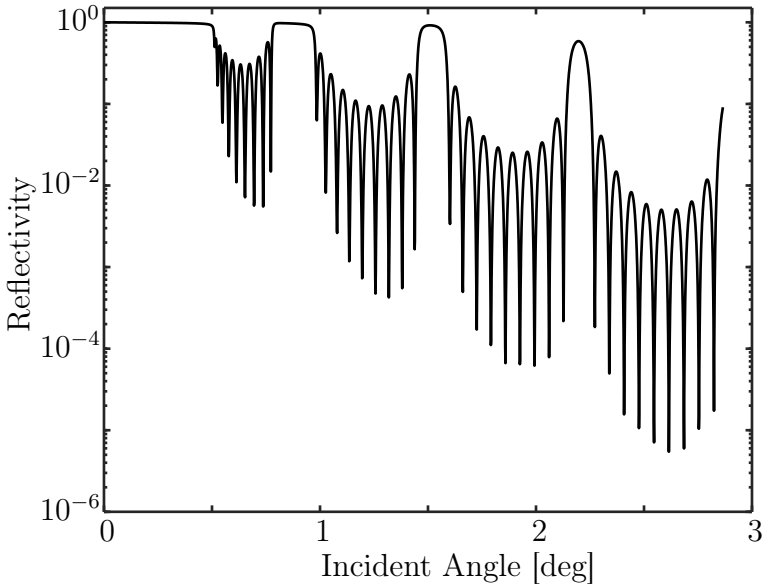

Figure 2.3: Specular reflectivity from a Iridium/Silicon multilayer calculated using the Parratt formalism. There are 10 bilayers consisting of 1 nm Ir on 4 nm Si.

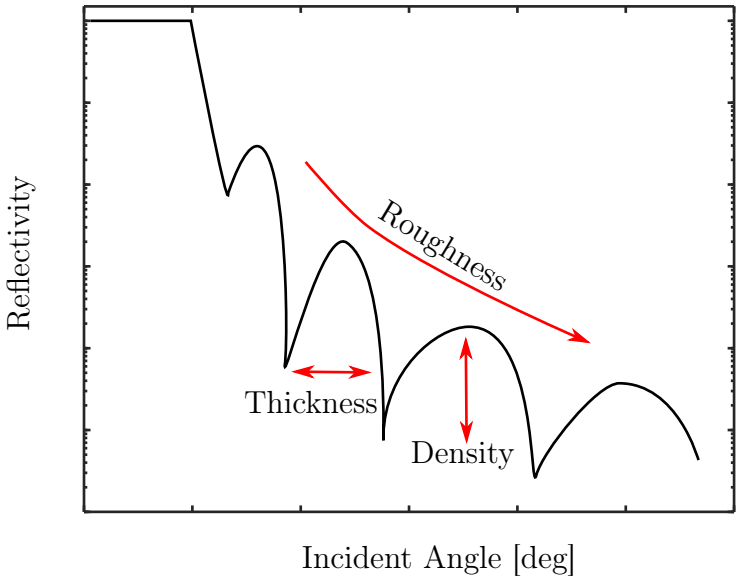

Figure 2.4: The XRR curve for multilayers is effected by surface roughness, layer thickness and layer density. These variables can be determined from the XRR curve to characterize a sample.

2.3 Rough Surfaces and Interfaces

The presence of surface roughness causes the reflections from an interface to develop a diffuse component called off-specular scatter. This diffuse component reduces the in-

tensity of the specularly scattered radiation by a factor $f(\sigma)$ where σ is the root-mean-square (RMS) roughness of the interface. There are many factors that can be used to approximate the change in intensity due to surface roughness; common factors are: the Névot and Croce (NC) factor [13,22] $f(\sigma) = \exp(-2\mathrm{k}_{0(z)}\mathrm{k}_{1(z)}\sigma^2)$ which holds for small $\mathbf{k}_0$ such that $k\sigma \leq 1$, the Debye-Waller factor (DWF) [36] $f(\sigma) = \exp(-2\mathrm{k}_{0(z)}{}^2\sigma^2)$ which is a good approximation for large $\mathbf{k}_0$ such that $k\sigma >> 1$, the second-order distorted wave Born approximation (DWBA) factor [28] $f(\sigma) = \exp(1 - 2\mathrm{k}_{0(z)}{}^2\sigma^2)$ which holds for most $\mathbf{k}_0$, and a factor by Sinha [18] $f(\sigma) = \exp(-4k^2 \sin\theta_0 \sin\theta_1 \sigma^2)$ which tends to be an accepted general formula that slightly under-estimates reflectivity at low $\mathbf{k}_0$ and slightly over-estimates reflectivity at high $\mathbf{k}_0$.

For a gold sample having constant surface roughness, Figure 2.5 shows the effect of RMS roughness from perfectly smooth to $\sigma = 4$ nm.

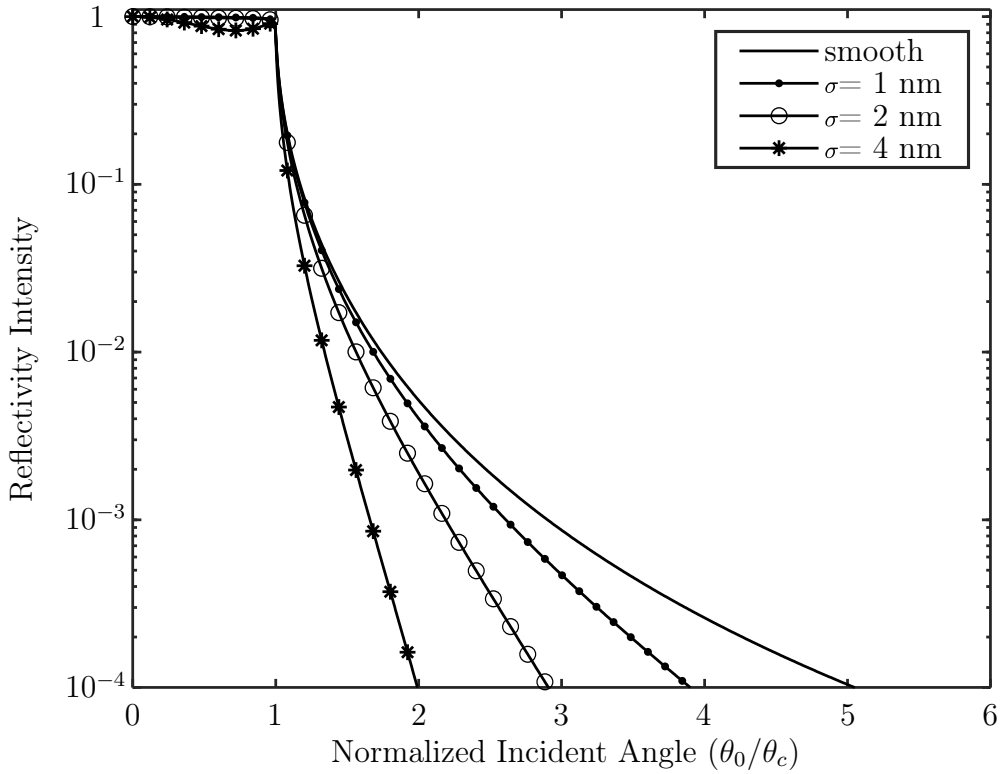

Figure 2.5: Calculated specular reflectivity vs. normalized incident angle for Mo $K\alpha_1$ radiation on a gold sample with average roughness $\sigma = 0$ nm, 1 nm, 2 nm, 4 nm using the NC factor. Surface roughness has a dramatic effect on the intensity of the specular reflections.

Figure 2.6 compares the output of different roughness models for a gold surface having RMS roughness $\sigma = 5$ nm.

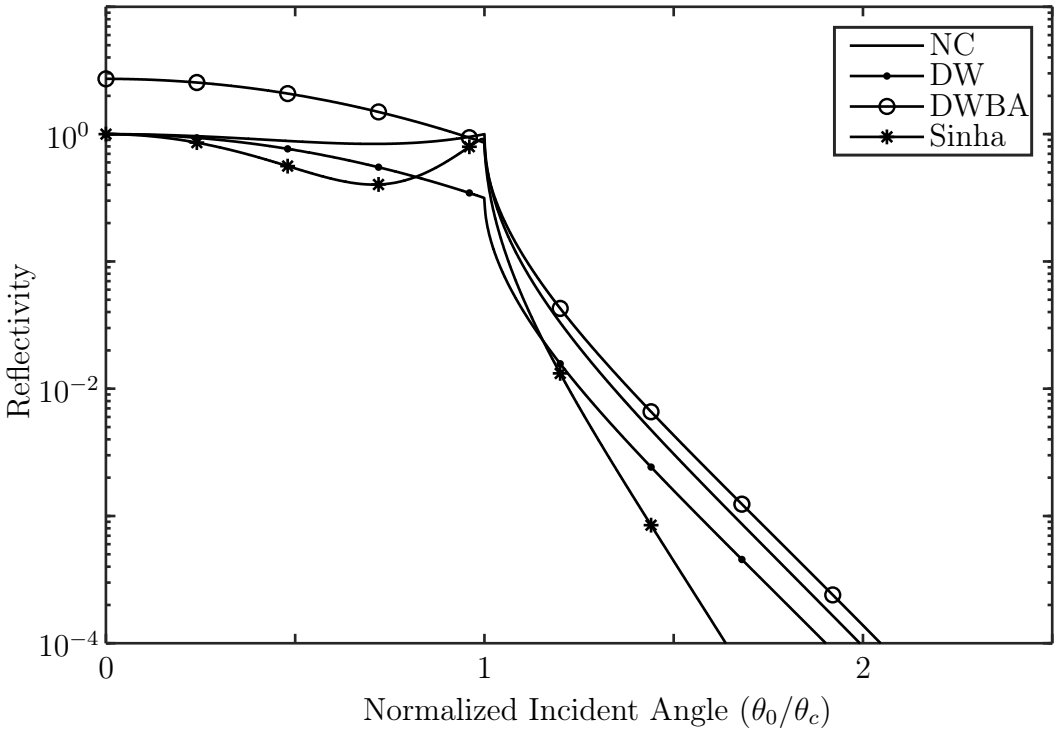

Figure 2.6: Calculated specular reflectivity vs. normalized incident angle for Mo $K\alpha_1$ radiation on a gold sample with RMS roughness $\sigma = 5$ nm using the Névot-Croce (NC), Debye-Waller (DW), distorted wave Born approximation (DWBA) and Sinha models. Each model over estimates or under estimates the reflectivity. Selection of the correct model depends on the parameters of the surface and the X-ray wavelength.

2.4 Alignment and Experiment Guide

This section serves to assist in the setup and execution of a standard X-ray reflectivity measurement for the purpose of surface roughness extraction. Experimentally the relatively low grazing incidence angles requires precise alignment and positioning of the sample relative the incident beam. These procedures are critical for matching results to theoretical models.

2.4.1 Sample Alignment

The goal of the sample alignment procedure is to align the sample face parallel to the incoming X-ray beam, with the center of rotation about the sample face, and for the sample face to be in the center of the beam. Figure 2.7 depicts the ideal alignment of the sample after the sample alignment procedure and Figure 2.8 represents a typical orientation after mounting a sample for the first time.

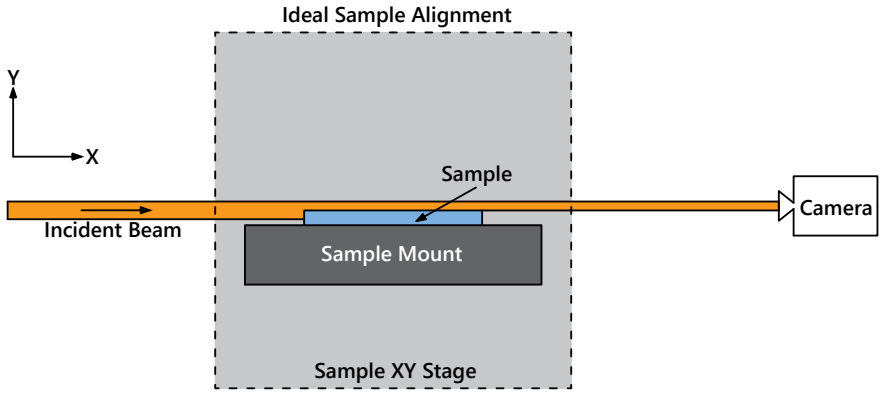

Figure 2.7: Ideal sample alignment after alignment procedure has been completed. The sample face is in the center of and parallel to the beam.

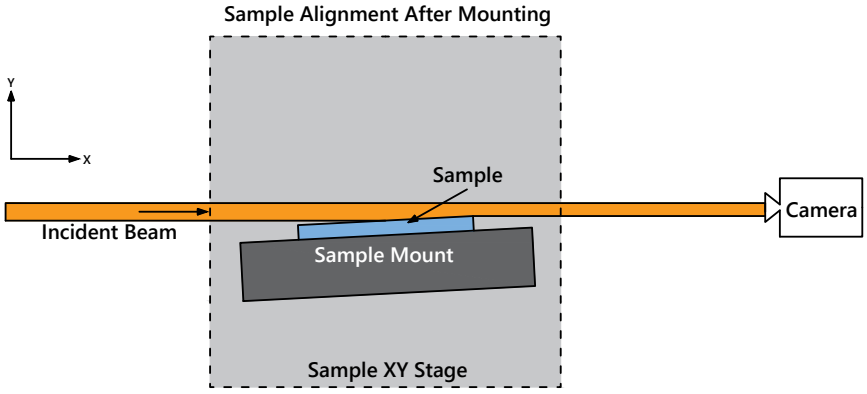

Figure 2.8: Initial sample alignment before alignment procedure has been completed. The sample face is not in the center of and is not parallel to the beam. A "Y-scan" and "θ-scan" is necessary to correct the alignment.

Alignment: Y-Scan

The first step in the alignment process is to roughly place the sample in the center of the incident beam. To do this the sample is translated in the Y direction in

sufficiently small steps (approximately 50 steps depending on required exposure time) while logging the integrated detector intensity. A plot of the Y displacement verses Integrated Detector Intensity can then be used to find a first estimate for the Y displacement value associated with the center of the beam, indicated in Figure 2.9 as $Y_{1/2}$.

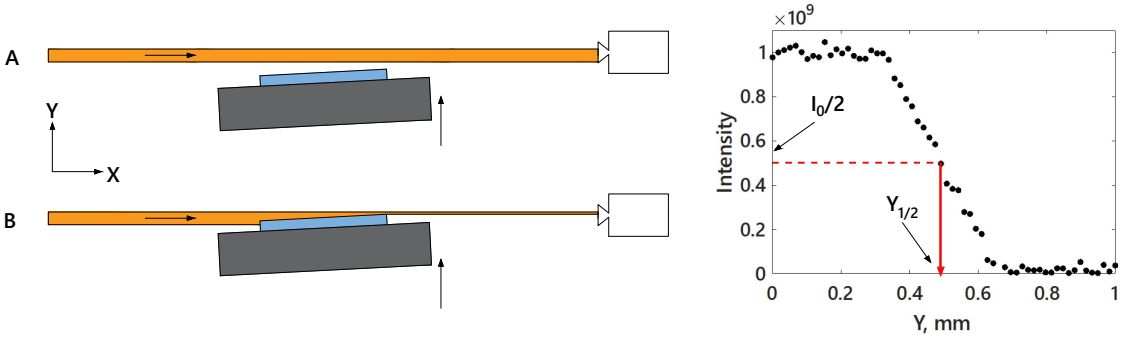

Figure 2.9: Performing a Y scan will provide a graphical representation of the beam size as a function of Y displacement of the sample. When the sample is blocking half of the X-ray beam, the detector will measure half the initial intensity, A depicts the starting position of the scan; B depicts a position during the scan.

Alignment: θ-Scan

A θ-scan or "rocking scan" consists of rocking the sample surface in the X-ray beam (approximately $\pm$ 1°) and recording the detector intensity for each step in θ. Figure 2.10 shows the typical result from a θ-scan. The location where the sample surface is most parallel to the beam will correspond to the maximum intensity in the detector.

Alignment: Fine Alignment

After the initial Y- and θ- scans, additional scans may be performed with smaller step sizes to fine-tune the sample alignment. It is suggested that at least two Y- and θ- scans be performed; typically three to four scans with converging limits are necessary.

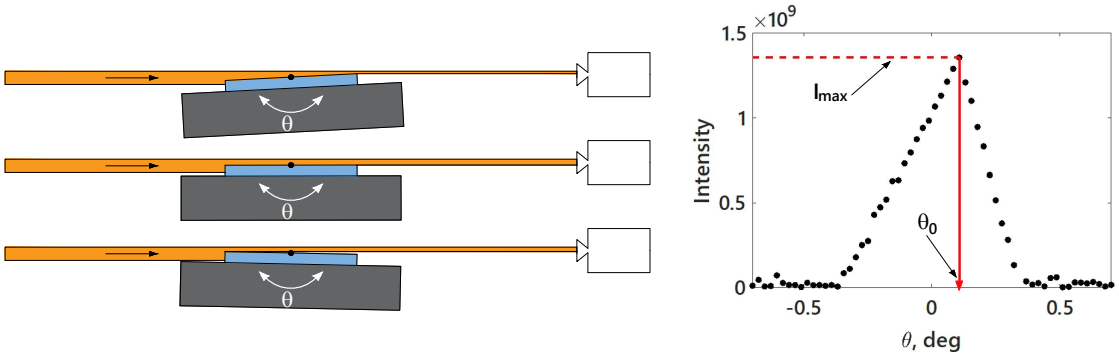

Figure 2.10: A θ scan will result in an intensity versus θ plot where the maximum intensity corresponds to the θ value where the sample surface is most parallel to the incident X-ray beam. After the θ scan, the position corresponding to the maximum intensity on the plot should be set to the starting angle, θ_0.

2.4.2 Experimental Procedure

The goal of an XRR experiment is to obtain the reflectivity intensity vs θ plot and fit the measured plot to a model of a surface that includes roughness. An example reflectivity curve is shown in Figure 2.11. Two pieces of information must be gathered for each step in θ: the angle relative to the incident beam (relative to θ_0 set in the alignment procedure) and the intensity of the reflected X-ray beam measured using an X-ray camera.

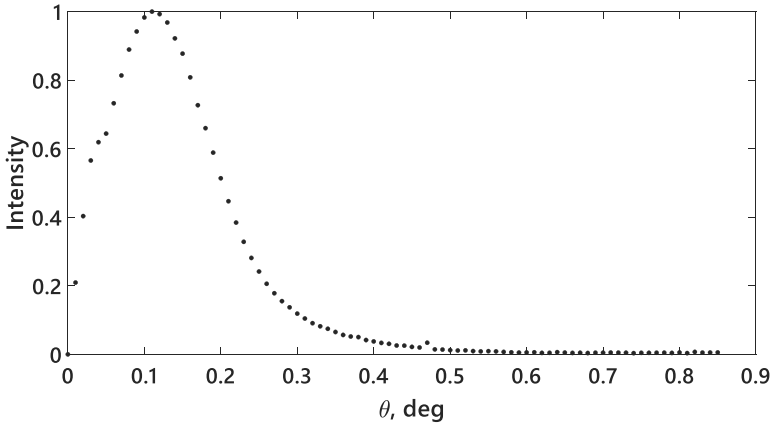

Figure 2.11: A small step size in θ is important to gathering enough information in a reflectivity scan. The data above is for a Tungsten Carbide surface and was taken with 0.005° steps.

For most materials with reasonable roughness, the first $\sim$ 0.2° of the scan will

produce strong reflections after which the intensity will drop with $\sim \theta^4$. Because of this strong drop-off in intensity, most reflectivity scans span only 1 - 5° of rotation of the sample. Small steps in θ typically around $0.001° - 0.005°$ must be taken to obtain sufficient data to estimate the parameters of the model.

Reflectivity Intensity Extraction from Multi-pixel Detectors

The simplest data collection method for XRR experiments is to use a single-pixel detector and correct geometry to separate the incident beam from the reflected beam; however, for very small angles, it can be difficult to ensure that the incident beam is not on the detector. Figure 2.12 depicts the relatively small separation between the incident beam and the reflected beam on the detector.

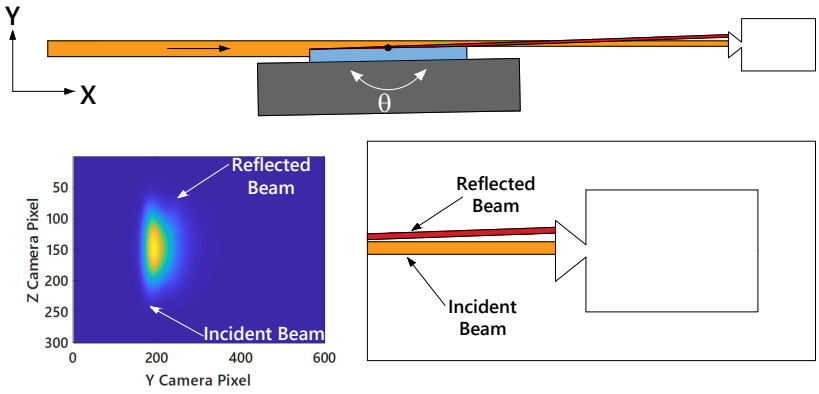

Figure 2.12: At low angles, the incident beam and reflected beams are not separated. Images can be summed in the Z direction without losing information.

On a multi-pixel detector, the reflectivity can be extracted by summing in the direction parallel to the rotation axis (Y axis in the example figures), subtracting the image of the incident beam, and integrating over all intensity that is greater than zero. When the incident beam is subtracted from an image, only light that has been reflected off of the part will remain. This process is shown in Figure 2.13.

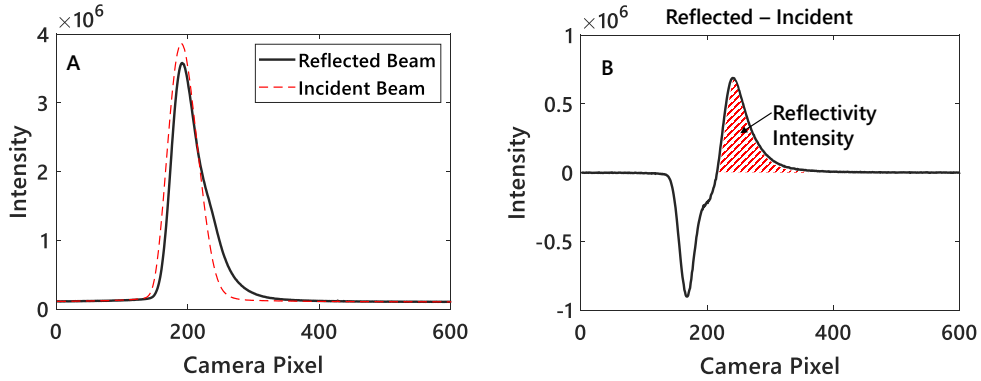

Figure 2.13: Once the images are summed (A), the image with reflections has a visible "hump" where the incident beam is being diverted in another direction. Subtracting the incident beam from the reflected beam (B) leaves only the reflectivity intensity above zero. Summing under this curve gives the reflectivity intensity for any given angle.

CHAPTER 3: THE INFLUENCE OF MID SPATIAL FREQUENCY ERRORS ON X-RAY REFLECTIVITY MEASUREMENTS

In the previous Chapters, reflectivity models are presented that are based on flat surfaces with small perturbations (roughness). This chapter addresses the effect of features having larger spatial wavelength than that of the high-frequency roughness considered above.

3.1 Motivation

Mid Spatial Frequency (MSF) errors are geometrical errors on a surface that are in a spatial wavelength range of approximately 0.08 mm to 3 mm and can have peak-valley (PV) amplitudes of several nm up to approximately 100 nm. MSF wavelengths fall between the features of form and roughness as broadly specified in ISO 4287 for profile measurements and ISO 25178 for areal measurements. These errors are often remnants of non-uniform material removal during final grinding and polishing operations [37, 38]. MSF errors decrease the performance of optical components and, while in-process mitigation is important but not yet fully developed, failure to quantify these errors can lead to over specification of ineffective components [39, 40]. Optics that are of particular relevance for these tolerance specifications can be found in many critical applications such as X-ray optics, lithography, and precision imaging applications. Many anecdotal experiences with optics meeting both figure and finish specification yet are "useless for its intended purpose" can be found in [41]. Therefore, tools that measure MSF errors are particularly relevant to many fields where optical components having complex surfaces are becoming more common and topographic tolerances are increasingly critical to function.

Many tools exist and are commonly used for MSF error measurement such as laser Fizeau interferometers for areal characterization and tactile profilometers for profile traces. Typically instruments that are capable of MSF error measurement are also capable of figure measurement but, for surface roughness measurement, often a second instrument such as atomic force microscopy (AFM) or scanning tunneling microscopes (STM) must be used and instrument transfer function matching must be considered. A non-contact tool for simultaneous measurement of MSF and finish statistics would be highly effective in the field of optical metrology and manufacturing and can be achieved with a standard X-ray reflectivity (XRR) measurement if a different approach to analysis is used. X-ray reflectivity is known to be a highly sensitive surface roughness measurement tool, even more sensitive than STM [25] with its ability to probe surface features on the sub-nanometer level. However, X-ray reflectivity is traditionally limited to flat and smooth surfaces with mid-spatial "ripples" affecting the ability for fitting algorithms. This hindrance has limited XRR measurements to the spatial wavelength region that is occupied by AFM and, with the added setup complications of XRR, AFM is often chosen as industry standard. A novel reflectivity model presented here addresses this limit and allows surfaces containing larger spatial wavelengths to be fit to traditional XRR models and provides a measure of the surface roughness and mid-spatial frequency errors. Using this model does not change the experimental procedure of XRR but rather expands the capabilities of XRR to simultaneous measurement of both high- and mid-spatial frequency errors of high-performance surfaces.

3.2 Model Formalism

Modelling of X-ray specular and diffuse scatter from surfaces having nanometer level surface roughness can be considered relatively well understood [11, 13, 18, 26, 27, 30]. To determine the effect of longer-range waviness features on these measurements, it is reasonable to consider a surface initially having a uniform spectral density, $S_0(\omega)$,

for which the higher frequency components are substantially attenuated using a low pass filter. In terms of a manufacturing process this smoothing might correspond to a final fine finishing process where roughness values are reduced to a few nanometers or less but waviness features remain. In this case, the reduction of the high-frequency components will result in a shorter correlation length surface roughness that is considered in most reflectivity models, for a review see [42]. Typically, the longer-range features that remain from previous surface modification processes are considered to represent the waviness features of the final surface. Such a surface is modeled as two, superposed topographies, one containing relatively long correlation lengths and large amplitude; the other being the short spatial wavelengths representing the nanometer or sub-nanometer roughness of the final finishing process. Modelling the long wavelength features by a first order filter with a spatial frequency cut-off at ω_0, the spectral density S_f of the filtered surface profile is given by

$$S_f(\omega) = \frac{S_0(\omega)}{1 + \left(\frac{\omega}{\omega_0}\right)^2}. \tag{3.1}$$

Using the Weiner-Kintchine theorem, the auto-correlation function $R_L(\tau)$ corresponding to this spectral density is given by the inverse Fourier transform

$$\begin{aligned} R_L(\tau) &= 2{\omega_0}^2 \int_0^\infty \frac{S_0}{{\omega_0}^2 + \omega^2} e^{j\omega\tau}\, d\omega \\ &= 2{\omega_0}^2 \int_0^\infty \frac{S_0}{{\omega_0}^2 + \omega^2} \cos(\omega\tau) d\omega \\ &= \begin{cases} S_0 \pi \omega_0 e^{-\omega_0 \tau} & \text{if } \tau > 0; \\ S_0 \pi \omega_0 e^{\omega_0 \tau} & \text{if } \tau < 0. \end{cases} \end{aligned} \tag{3.2}$$

This can be written in the form

$$R_L(\tau) = {\sigma_L}^2 e^{-|\omega_0 \tau|}, \tau > 0, \tag{3.3}$$

where

$$\sigma_L{}^2 = S_0 \pi \omega_0 \tag{3.4}$$

is the root-mean-square (RMS) of the waviness. Therefore, ω_0 can be considered as the correlation length of the filtered surface. From Longuet-Higgins [43], for small slopes, the probability density $p(\zeta)$ of the local slope ζ of a random surface is approximately Gaussian,

$$p(\zeta) = \frac{1}{\sqrt{2\pi m_2}} e^{-\frac{\zeta^2}{2m_2}}, \tag{3.5}$$

where m_2 is the mean square surface slope that can be computed from the integral of the second moment of the power spectral density, see [44, 45]. Hence

$$\begin{aligned} m_2 &= \int \omega^2 S_f(\omega)\, d\omega \\ &= \frac{\sigma_L{}^2 \omega_0}{\pi} \int \frac{\omega^2}{\omega_0{}^2 + \omega^2}\, d\omega. \end{aligned} \tag{3.6}$$

This integral does not converge over all limits. However, it is reasonable to consider only the spatial frequencies longer than the correlation length corresponding to the X-ray scale surface roughness (or integer divisors thereof). Based on this assumption, the mean slope is given by

$$\begin{aligned} m_2 &= \frac{2\sigma_L{}^2 \omega_0}{\pi} \int_0^{\frac{\omega_0}{n}} \frac{\omega^2}{\omega_0{}^2 + \omega^2}\, d\omega \\ &= \frac{2\sigma_L{}^2 \omega_0}{\pi} \left[\frac{1}{n} - \tan^{-1}\left(\frac{1}{n}\right) \right]. \end{aligned} \tag{3.7}$$

For $n = 1$ the mean slope is given by

$$\begin{aligned} m_2 &= \sigma_L{}^2 \omega_0{}^2 \left[\frac{4 - \pi}{2\pi} \right] \\ &= 0.137 \sigma_L{}^2 \omega_0{}^2. \end{aligned} \tag{3.8}$$

To determine the influence of these waviness features on X-ray reflectivity, it is necessary to consider the distribution of slopes encountered by a beam incident at an angle θ. For a flat surface with RMS roughness σ greater than about 3 nm, first-order distorted wave Born approximation (DWBA) models break down and the specular reflectance $R(\theta)$ can alternatively be obtained analytically with a hyperbolic tangent interface function from [26],

$$R(\theta) = \frac{\sinh\left[\sigma\left(\frac{\pi}{2}^{\frac{3}{2}}\left(q_z(\theta) - q_{z,t}(\theta)\right)\right)\right]}{\sinh\left[\sigma\left(\frac{\pi}{2}^{\frac{3}{2}}\left(q_z(\theta) + q_{z,t}(\theta)\right)\right)\right]} G. \tag{3.9}$$

For engineering surfaces with high polish, i.e. $\sigma < 10$ nm, the phase factor $G \approx 1$ [22]. In the above equation, q_z and $q_{z,t}$ are the normal components of the wave-vector transfers in and out of the medium shown in Figure 3.1 and are given by

$$q_z = \mathbf{k} - \mathbf{k}' = 2k_0 \sin\theta \tag{3.10}$$

$$q_{z,t} = \mathbf{k}_t - \mathbf{k}'_t = 2k_0 \sin\theta', \tag{3.11}$$

where θ and θ' are the incident and refracted angles of interaction by the X-rays, related by

$$\cos\theta' = \frac{\cos\theta}{\cos\theta_c}. \tag{3.12}$$

The critical grazing incidence angle, $\theta_c = \sqrt{2\delta}$, is the angle below which the X-rays experience total external reflection where δ is the refractive index unit decrement corresponding to the specific material and X-ray energy.

The intensity of the reflected X-rays can be determined from the square of the reflectance. To determine the effect of the waviness on the measured intensity, it is necessary to determine the scattering by this mosaic of slopes that will result in an effective specular blurring over the range of surface slopes which can be considered to span $\pm 3\sqrt{m_2}$. So, for any incident angle θ, the effect of the surface mosaic on the

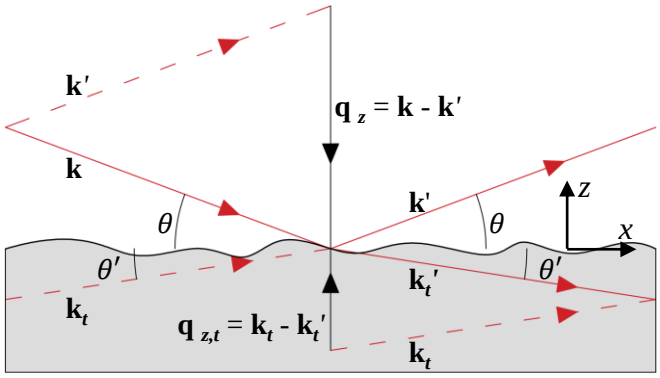

Figure 3.1: Diagram of the reflection and refraction of X-rays about an interface. x is along the surface average, z is normal to the surface, θ is the angle of incidence and angle of reflection, and θ' is the angle of refraction.

measured intensity can be determined from the integral

$$\begin{aligned} I(\theta) &= \int_{-3\sqrt{m_2}}^{3\sqrt{m_2}} R(\theta) * R(\theta) P(\zeta)\, d\zeta \\ &= 2\int_{0}^{3\sqrt{m_2}} |R(\theta+\zeta)|^2 P(\zeta)\, d\zeta. \end{aligned} \tag{3.13}$$

Equation 3.13 contains both of the surface roughness and waviness terms and is used to fit the experimental data. A comparison of Equations 3.9 and 3.13 are presented in Figure 3.2.

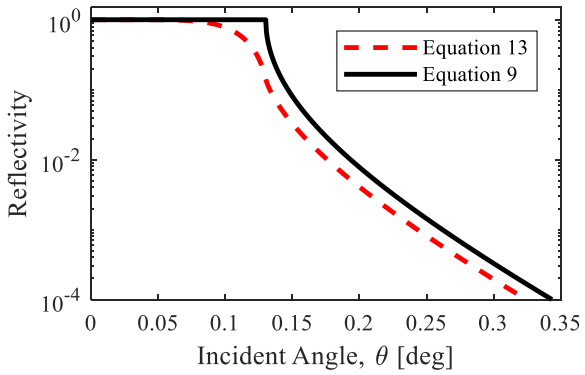

Figure 3.2: The computed reflectivity of Schott glass at 14 keV using Equation 3.9 and Equation 3.13. Surface properties were $\sigma = 2$ nm, $\sigma_L = 20$ nm, and $\omega_0 = 1/15\,\mu$m. The waviness contributes to an overall decrease in reflectivity and a rounding-off at the critical angle.

3.3 Experiments

Measurements were carried out at the Advanced Light Source at Lawrence Berkeley National Laboratory, Micro-CT Beamline 8.3.2 [46]. Shown in Figure 3.3.

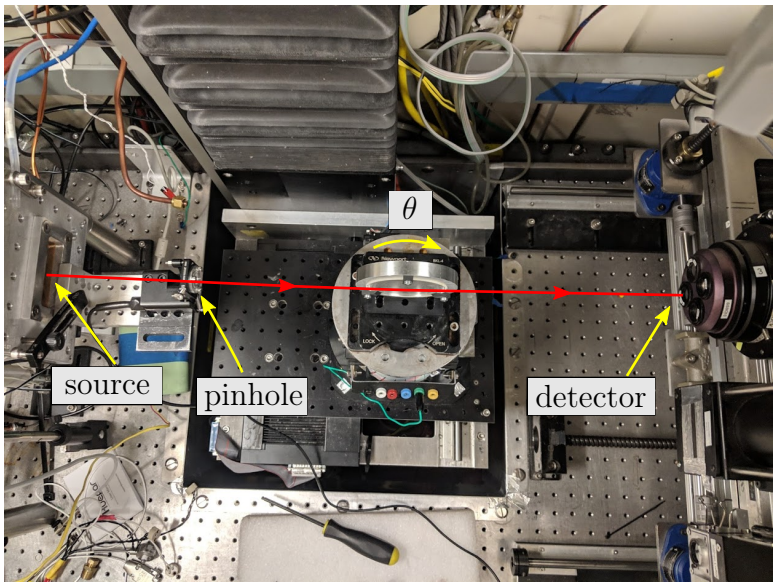

Figure 3.3: Experimental setup at Beamline 8.3.2 at the Advanced Light Source. The source beam passed through a 100 μm Tungsten pinhole, the sample was mounted on an air bearing rotary stage and the radiographs were collected on a detector that imaged a scintillator with a 2 X magnification objective lens.

X-ray energies from 14 - 22 keV were selected with a monochromator. The beam was constrained with a 100 μm Tungsten pinhole and had a flat intensity distribution. The sample to detector distance was 250 mm. The optical system consisted of a 50 μm LuAG scintillator and 2 X objective with a multipixel detector (PCO Tech PCO.Edge) , resulting in a pixel size of 3.22 μm. For each reflectivity scan, 100 images were collected over 0.5° of total rotation with an angular resolution of 0.005° using up to 500 ms exposure time depending on the energy selected.

A reference image of the beam was collected for the use of normalization. Starting with the sample face parallel to the axis and located at the center of the beam, the sample angle was incremented and a single image collected for each point on the reflectivity curve. From each image, the initial ($\theta = 0°$) reference image was subtracted

and the image was summed in the vertical direction. Non-negative intensity in the subtracted, vertically summed images, was integrated to extract the total intensity of the reflected beam for each incident angle.

A BK7 optical flat was chosen for measurement. This sample had a nominal flatness of $\lambda/4$ ($\lambda = 633$ nm) and a sinusoidal profile was polished into the planar surface using magnetorheological finishing [47]. To test the robustness of the theory, a large amplitude (approximately 75 nm P-V) and relatively high frequency (approximately 0.5 cycles/mm) waviness was polished into the surface; providing an extreme example of the type of surface that might be seen in high-performance optics. The reflecting surface was measured using atomic force microscopy (AFM) with a Dimension 3100 manufactured by Digital Instruments to investigate the high-frequency, low amplitude roughness. Profile traces, performed with a Mahr MarSurf LD260 profilometer capable of 0.8 nm resolution, were taken along the beam footprint path to measure the higher amplitude, lower-frequency waviness features. 2D areal measurements of the waviness were performed with a Zygo Verifire Fizeau interferometer with a 4 inch field of view and RMS repeatability of < 0.06 nm. Measurement results from the profilometer are presented in Figure 3.4 and Fizeau interferometer results are presented in Figures 3.5 and 3.6.

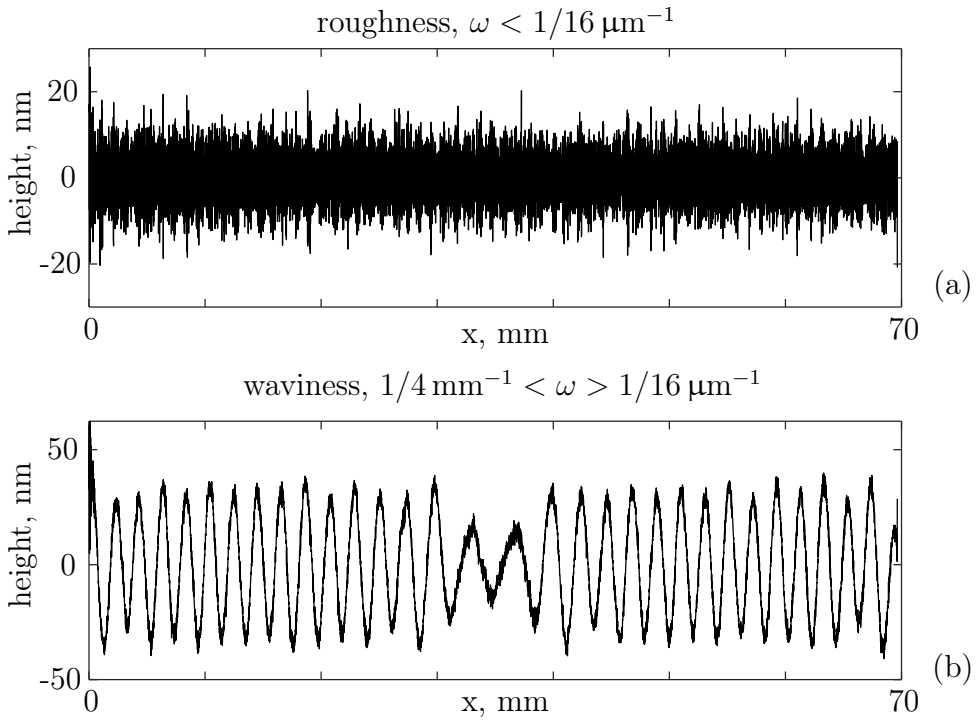

Figure 3.4: Filtered profilometer results, filtered at $(1/16)\,\mu\text{m}^{-1}$. While the profilometer could easily measure the waviness features (a), the high frequency content includes instrument noise (b).

3.4 Results

The extracted reflectivity information for various energies is shown in Figure 3.7.

All data was normalized to the reference image for each energy data set. A MATLAB program was used to iteratively search for best fit of the experimental data against Equation 3.13. The fitting algorithm consisted of a Nelder-Mead simplex multi-dimensional unconstrained optimizer to minimize a squared cost function solving for RMS surface roughness σ, RMS surface waviness σ_L and cut-off frequency ω_0. Data obtained below 0.05° do not lie on the curve fit due to the beam footprint being larger than the sample at these small incident angles. The resulting fit is presented with experimental results in Figure 3.7.

The extrapolated parameters from the best fit for each of the four energies were averaged resulting in $\sigma = 2.9 \pm 0.2$ nm, $\sigma_L = 14.6 \pm 0.5$ nm with a cut-off frequency

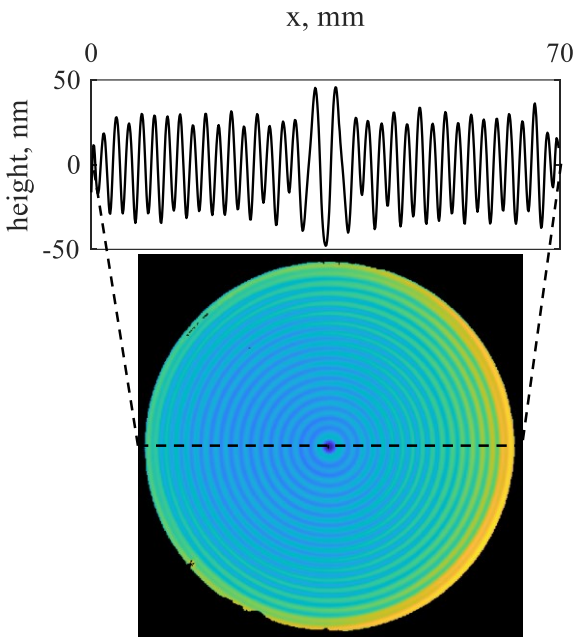

Figure 3.5: Result from the 2D areal Fizeau interferometer measurement of the BK7 flat. The highlighted trace is along the path that the XRR measurement was performed.

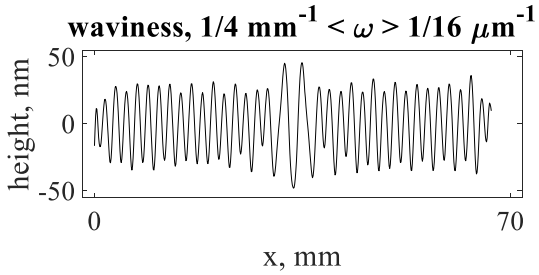

Figure 3.6: Decomposed and filtered Fizeau measurement data. The data was filtered at $(1/16)\ \mu\text{m}^{-1}$; however, the Fizeau interferometer cannot measure frequencies in the higher, roughness range and therefore the roughness plot contains no information.

between roughness and waviness of $\omega_0 = 1/(18 \pm 2)\ \mu\text{m}^{-1}$. Table 3.1 displays the results from the fitting algorithm for each energy.

The sample was also subject to AFM, Fizeau interferometry, and surface profilometry measurements. These measurements were bandwidth limited to extract both the surface roughness and waviness at the average frequency based on the XRR data fit results above.

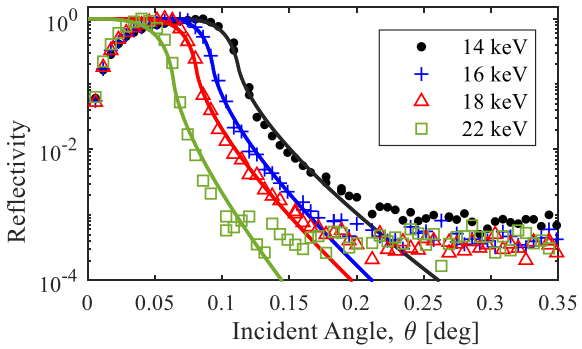

Figure 3.7: Experimental result of reflectivity for the measurement of a BK7 surface with roughness and waviness features for $E = 14 - 22$ keV. Theoretical fits to the data using Equation 3.13 are shown as solid lines.

Table 3.1: Tabulated results from the XRR curve fits in Figure 3.7.

	σ (nm)	σ_L (nm)	ω_0 (μm^{-1})
14 keV	2.8	14.2	1/17
16 keV	3.1	14.0	1/20
18 keV	2.8	15.3	1/20
22 keV	3.1	14.8	1/15

When limited to feature frequencies of (1/20) μm^{-1} or greater, the AFM measurements resulted in an average roughness of $\sigma_{\text{AFM}} = 3.4 \pm 0.4$ nm. When limited to frequencies of $(1/16)\,\mu\text{m}^{-1}$ to $(1/4)\,\text{mm}^{-1}$, the Fizeau measurements resulted in a waviness of $\sigma_{L,\text{Fizeau}} = 21.6$ nm. When limited to frequencies of $(1/16)\,\mu\text{m}^{-1}$ to $(1/4)\,\text{mm}^{-1}$, the profilometry measurements resulted in an average roughness of $\sigma_{\text{Prof}} = 4.0 \pm 0.1$ nm and a waviness value of $\sigma_{L,\text{Prof}} = 21.4 \pm 0.1$ nm.

A summary of the AFM and profilometry measurements is shown in Table 3.2.

Spurious scattering and absorption of higher slopes on the surface will impact the reflectivity and influence the waviness result which could explain differences seen here and must be investigated in further studies. Additionally, the roughness values from X-ray reflectivity are sensitive to the reflectivity intensity being artificially high due to unfiltered diffuse scatter reaching the detector. This will cause the measurement result to be smoother and may contribute to variations seen in this work. Additions of slits

Table 3.2: Tabulated results from the AFM measurements and the profilometry measurements. It is important to note that all XRR and profilometry measurements were taken along a single, longitudinal trace across the surface; while the AFM measurements are at 5 different 40 μm × 40 μm patches along the same trace.

	σ_{AFM} (nm)	σ_{prof} (nm)	$\sigma_{L,prof}$ (nm)
Run 1	2.7	3.8	21.4
Run 2	3.3	4.0	21.5
Run 3	4.0	4.0	21.2
Run 4	3.5	4.1	21.6
Run 5	3.4	4.1	21.5

or longer sample to detector distance may reduce the collected diffuse scatter. The model presented here assumes both the roughness and waviness are approximately Gaussian whereas some processed surfaces may have a height distribution that is non-Gaussian. This is a known disadvantage with XRR due to the dependence of the extracted parameters on the theoretical model of the surface [48]. As mentioned in the introduction, many models for simulating X-ray reflectivity exist with different interface probability density functions: Gaussian [13], tanh [26], $\cos^{-2}$ [49]. It is important to use the correct model to approximate the reflectivity of the surface; however, surfaces subject to many fine finishing steps such as mechanical, ion beam, elastic emission, and magneto-rheological polishing will approach Gaussian height distributions as the 'fingerprints' of previous processes are removed.

Upper limits on roughness amplitude typically are related to the radiation wavelength [18], and the application of this method with soft X-ray sources could extend the range of amplitudes measurable but will increase the low spatial wavelength cut-off. Further evaluation of more complex surfaces is required to set formal limits on this technique.

3.5 Remarks on Instrument Comparisons

XRR measurements are laterally averaged over 10's of mm and often are influenced by large amplitude surface asperities; whereas, AFM measurements are typically ac-

quired in a small region (i.e. 40 μm × 40 μm in this experiment). Given a stationary, ergodic surface, the larger area averaging of the XRR measurement will result in lower variance than AFM measurement. With this large difference in measurement area, comparison between measurements at these levels is difficult. Profilometry measurements use a tactile probe with a finite radius, typically around 1 μm or larger and considerably larger than AFM tip radii. This stylus probe tip size will apply a low-pass filter to the measurement; whereas, XRR measurements, due to the short wavelengths of X-rays, can probe surface features having significantly higher spatial frequencies than AFM and profilometry. Optical surface measuring instruments such as Fizeau interferometers are typically unable to resolve lateral features comparable or smaller than the optical wavelength or features containing large slopes and are typically only used for mid-spatial frequency and form measurements. Figure 3.8 shows the power spectral density (PSD) for the Fizeau and profilometer. The PSDs of these instruments overlap in the waviness region, but the profilometer measures well into the roughness region but with additional electrical noise. While there are many nuances to these statements the above comments are reflected by the occupied regions of these instruments on a Stedman [50–52] (Amplitude-Wavelength) map.

In this case, the profilometry and Fizeau bandwidth limited waviness values agreed within about 1%.

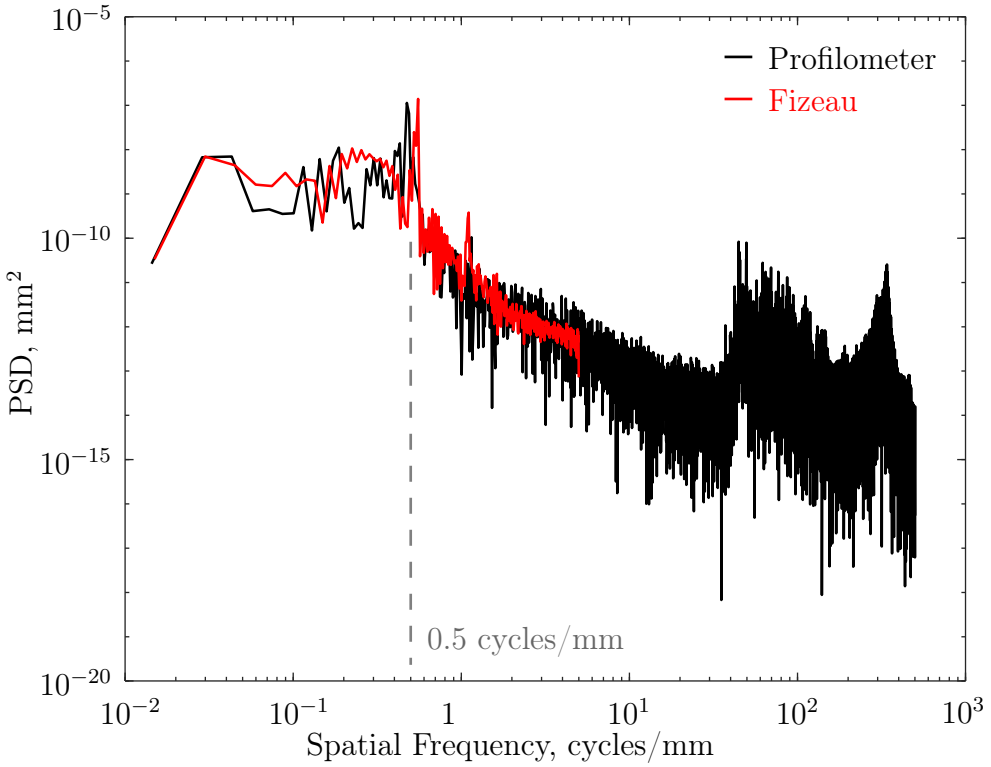

Figure 3.8: The power spectral density of the Fizeau interferometer and the stylus profilometer overlap in the waviness region; however, the profilometer is capable of measurements in the higher-frequency roughness region. The main MSF error in the optic is in the 0.5 mm/cycle region and is shown by a peak in the PSD.

CHAPTER 4: X-RAY REFLECTIVITY OF CURVED SURFACES

As with the previous Chapter, the following discusses the effect of non-traditional surface geometry on traditional X-ray reflectivity models. Here, surfaces having constant curvature are considered to explore the effect of form error on X-ray reflectivity.

4.1 Motivation

Advances in manufacturing have made it possible to control surface topography across spatial wavelength scales. In particular, recent developments in ultra precision manufacturing processes such as ion beam machining, diamond turning, magneto-rheological finishing, elastic emission machining, and small pad polishing for mid-spatial frequency control combine to provide methods for surface modification across these scales. Modern applications include freeform optics, smart phone micro optics, internal confinement fusion targets, and liquid droplet devices, all of which have relatively high curvature (mm - cm) and require precise topographical control. For fine surfaces, determination of localized surface topography is challenging for traditional surface finish measurement devices such as atomic force microscopy (AFM) and stylus profilometry; whereas, these small surface perturbations still significantly influence small angle scattering of X-ray beams suggesting that this could be an important diagnostic tool. These tight-radius, typically convex, surfaces cannot be treated as flat reflectors for the purpose of established grazing incidence X-ray reflectivity measurements. The purpose of this work is to expand XRR models to include the effect of surface curvature; allowing the extraction of X-ray reflectivity information. In this study, we confine ourselves to two-dimensional geometries (i.e. single curvature); however, in the development of this model, a vector approach has been used that also

enables future extension to surfaces with arbitrary, localized curvature.

Objects having curved surfaces have many applications in optics, biophysics, high energy physics, and chemistry. In all of these fields, surface roughness and composition has significant influence on function, often at nanometer scales. An example that forms the motivation for this study is the evolution of the functional requirement for fusion target ablator layer surface roughness. In the mid-1990's the influence of surface roughness on hydrodynamic instabilities during the ablation phase of implosion was identified as a major factor limiting neutron yield. Cook [53] identified that high frequency surface perturbations are associated with large Rayleigh-Taylor instability growth and low frequency surface perturbations have little-to-no effect on implosion. The same year, Haan [54] postulated a maximum tolerable ablator roughness of 50-80 nm RMS. Seven years later, Dumay [55] revised the surface roughness requirement to less than 20 nm. Since this time, measurements have revealed that capsules can be manufactured with sub-10 nm RMS surface roughness [56]; however, significant surface imperfections arise during cooling (from 14 K to 12 K), a necessary part of capsule preparation prior to implosion [57]. In present day, concerns remain about the adequacy of the surface roughness requirements to obtain desired neutron yield [58, 59]. Smooth curved surfaces are also used for studying intermolecular and surface forces and have been since the 1970's. Early studies used cleaved mica surfaces bent over cylindrical forms to create ideal surface-to-surface interactions [60]. Today, available AFM probes with attached microspheres provide a substantially more sensitive measure of forces. Recent work has identified the need for ultrasmooth (sub-nm RMS roughness) microspheres to improve precision and accuracy of modern surface interaction force measurements [61].

X-Ray reflectivity (XRR) is an established, non-destructive tool for evaluating the surface and interfaces of highly polished optics, semiconductor wafers, and multilayered thin films used for many decades; for broad reviews, see [42, 62]. XRR is

one of the most sensitive methods for average roughness measurements, even more sensitive than scanning tunneling microscopes [20]. The upper spatial wavelength cut-off is proportional to the X-Ray beam size and the lower cut-off is on the order of the X-Ray wavelength ($\sim$ 1Å). This sensitivity to roughness makes XRR a powerful tool for the measurement of precision processed surfaces [27]. At glancing angles, X-Rays are totally reflected from solid surfaces [6]. For incident angles larger than the so-called critical angle, XRR intensity falls approximately with θ^{-4} for ideally smooth surfaces. The rate of decay of reflectivity is exceptionally sensitive to, and increases with, micro-scale roughness of the reflecting surface [11]. To extract quantitative topographical values, it is necessary to compare the measured decay with theoretical models of the reflectivity. Most models utilize the Born approximation for modelling reflection from weakly interacting rough surfaces and, while this is valid for incidence angles greater than the critical angle, a perturbation approach called the distorted wave Born approximation (DWBA) is typically used to determine both specular and diffuse scatter throughout the region of grazing-incidence angles [16, 18, 22]. While further, higher-order approximations have demonstrated increased accuracy [28], the first-order DWBA approximation remains a common approach for many applications [63–65].

Recent approaches to the calculation of X-Ray reflectivity from multilayers including interface roughness effects have employed Fresnel tensors based on the original Paratt formalism [66]. These methods, unlike other roughness considerations, take into account the effect of roughness-induced diffuse scattering in the combined signal. This approach is used in the models developed in this work. With very few exceptions, X-ray reflectivity studies have concentrated on measuring flat surfaces and stratified media to evaluate surface and interface roughness. Large radius curved surfaces have been utilized for beam conditioning for some time, for example soft X-ray telescopes such as the Chandra X-ray Observatory and Kirkpatrick-Baez focusing mirrors. Only

recently have papers emerged addressing the direct extraction of topographic information from substantially curved surfaces for which changes in the incident angle over the beam footprint and propagation through the curved portion are significant in the detected image. Little experimental data was found for curvatures relevant to the engineering applications discussed above. In an indirect effort to evaluate surface layer topography on Silicon spheres for the redefinition of atomic mass in terms of the newly defined Avogadro's number, Busch et al. [67] utilized X-ray reflectivity to calibrate an ellipsometer. Calibration was on a flat Silicon wafer with varying thickness Silicon Dioxide layers. As indicated in the article, it would have been desirable to have used the traceable XRR system. The large sphere and its curved surface could not be directly measured and therefore it was necessary to use an ellipsometer calibrated from the XRR system. Clearly, the direct measurement of curved surfaces using XRR would be of great benefit in this and related applications. A more applicable example is the work of Festersen [68] who theorized the geometric effect of XRR from the curved surface of a liquid droplet for the proposed use as liquid X-ray diffractometer. Measurements on free sessile droplets are discussed but not performed. Instead, the liquids that were measured were contained in large cells such that the center surface had low curvature; the values of which are not discussed. Stoev [33] proposed the utilization of large radius mirrors to create a divergent beam to measure all angles of an XRR curve in a single measurement named quick-XRR (qXRR). Using this method, it is proposed that a complete XRR curve can be extracted from a single image and a sequence of measurements can be used to measure dynamically varying surface effects. While this is extensively modelled for large concave mirrors, at the time of this study, experimental results have yet to be reported.

4.2 Geometry

Presented in the following sections is an approach for the measurement of surface roughness of curved surfaces with X-ray reflectivity which requires the modelling of both the geometry and the electric field of X-rays as they reflect from and pass through a part of circular cross-section. This section is broken into three subsections in which the propagation vectors (denoted $\mathbf{r}$) are derived for X-rays that are; (1) reflecting from the surface, (2) transmitting through the object, and (3) reflecting from an inner surface inside the object. In this section, positions are typically denoted as non-bold, italicised letters (e.g. P) and vectors are presented as bold, lowercase letters (e.g. $\mathbf{r}$). Additionally, in some diagrams, vector endpoints are shown as filled circles where arrows would occlude details relevant to the figure. The propagation vectors in this section are used in the following section to define the electric field of the X-rays as they propagate through the part.

For a surface of constant curvature such as a sphere or cylinder, there are three possible paths a monochromatic, collimated beam of X-rays will take: first, X-rays can scatter from the outer surface, second, X-rays can transmit through the part, and third, in the case of thin shells, X-rays can transmit through the outer surface, reflect off the inner surface, and transmit back through the outer surface. These interactions occur simultaneously for each incoming X-ray with reflections dominating at small incident angles and transmission dominating at high incident angles. The paths, depicted in Figure 4.1, will converge on the detector. Proper geometrical modelling of the X-ray interactions is required to determine where the X-rays will interact at the detector.

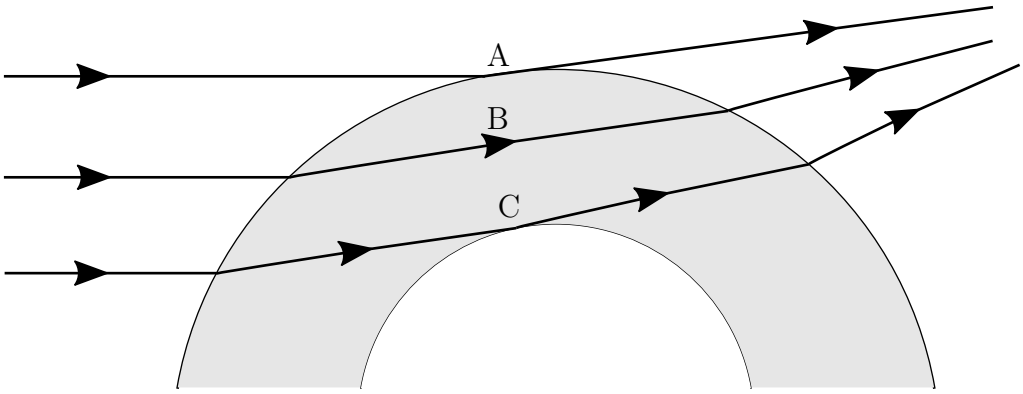

Figure 4.1: Three paths that X-rays will take when incident upon a cylindrical part of constant curvature. Path A is scattered from the exterior surface, Path B is transmission through the bulk material, and Path C is transmission through the material that is incident upon and scatters from an internal surface. These components will combine at the detector.

Consider a curved surface of constant radius R_{outer} (hereafter radii of surfaces is denoted by a roman R to distinguish from reflectivity R) with X-rays originating from a point P_{source} and incident at a point P_i shown in Figure 4.2. The X-rays are incident at varying angles from parallel ($\theta_0 = 0$) at the top of the part ($z = \mathrm{R}_{outer}$) to perpendicular ($\theta_0 = \pi/2$) at the center of the part ($z = 0$). The position of the source X-rays is tracked from the radius of the part in the x-direction and is related to the incident angle by

$$P_{source} = \mathrm{R}_{outer} \begin{pmatrix} -1 \\ 0 \\ \cos\theta_0 \end{pmatrix}. \tag{4.1}$$

The incident position is a function of the incident angle and is given by

$$P_i = \mathrm{R}_{outer} \begin{pmatrix} -\sin\theta_0 \\ 0 \\ \cos\theta_0 \end{pmatrix}; \tag{4.2}$$

therefore, the vector from the source to the point of incidence is

$$\mathbf{r}_0 = P_i - P_{source} = \mathrm{R}_{outer} \begin{bmatrix} 1 - \sin\theta_0 \\ 0 \\ 0 \end{bmatrix}. \tag{4.3}$$

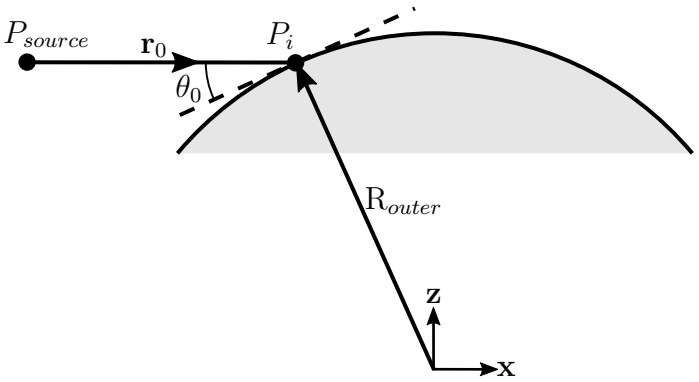

Figure 4.2: The location of incidence is a function of the incident angle and outer radius of the part. The coordinate system is defined with origin at the center of the part.

4.2.1 External Surface Reflection Measurement

X-rays specularly scatter at angle θ_0 from the surface tangent. If a detector is placed at a distance ODD (object-detector-distance) from the center of the part, the location of the scattered beam for case A $P_{d,A}$, from Figure 4.3, is

$$P_{d,A} = \begin{pmatrix} \text{ODD} \\ 0 \\ P_{i(z)} + (-P_{i(x)} + \text{ODD}) \tan 2\theta_0 \end{pmatrix}. \tag{4.4}$$

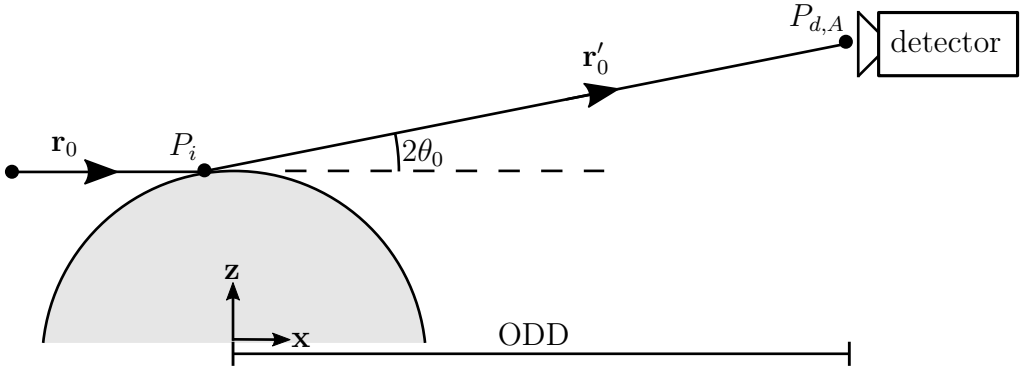

Figure 4.3: The location of the scattered beam for case A ($P_{d,A}$) is related to the incident position (P_i) and the distance between the object and the detector (ODD).

The distance from the point of reflection to the detector can be defined

$$\mathbf{r}'_0 = P_{d,A} - P_i. \tag{4.5}$$

In experiments, ODD, R_{outer} and the z-component of $P_{d,A}$ can be determined. The object-detector-distance can be physically measured, or, more precisely, a crystal of known scattering angle can be placed at the object center and the diffraction pattern observed. The crystal will diffract the X-rays at a known angle, and the diffraction pattern position on the detector will give the distance of the detector from the object. The height of the scattered beam on the detector can be found by measuring the number of pixels between the beam and a reference point and multiplying by the pixel size. Typically this reference point can be the shadow of the top of the sphere. The part radius can be measured using a number of methods which must be selected based on the size and material of the part. Using these known parameters, the incident angle θ_0 can be determined.

For small incident angles, an approximation for θ_0 is

$$\begin{aligned} P_{d,A(x)} &= P_{i(z)} + (-P_{i(x)} + \mathrm{ODD}) \tan 2\theta_0, \\ &= \mathrm{R}_{\mathrm{outer}} \cos\theta_0 + (\mathrm{R}_{\mathrm{outer}} \sin\theta_0 + \mathrm{ODD}) \tan 2\theta_0, \\ &\approx \mathrm{R}_{\mathrm{outer}} \left(1 - \frac{{\theta_0}^2}{2}\right) + (\mathrm{R}_{\mathrm{outer}}\theta_0 + \mathrm{ODD}) 2\theta_0. \end{aligned} \tag{4.6}$$

Rearranging terms into a quadratic,

$${\theta_0}^2 + \frac{4}{3}\frac{\mathrm{ODD}}{\mathrm{R}_{\mathrm{outer}}}\theta_0 + \frac{2}{3}\left(1 - \frac{P_{d,A(z)}}{\mathrm{R_o uter}}\right) = 0, \tag{4.7}$$

then,

$$\theta_0 = -\frac{2}{3}\frac{\mathrm{ODD}}{\mathrm{R_{outer}}} + \sqrt{\left(\frac{2}{3}\frac{\mathrm{ODD}}{\mathrm{R_{outer}}}\right)^2 - \frac{2}{3}\left(1 - \frac{P_{d,A(z)}}{\mathrm{R_{outer}}}\right)},$$
$$= -\frac{2}{3}\frac{\mathrm{ODD}}{\mathrm{R_{outer}}} + \frac{2}{3}\frac{\mathrm{ODD}}{\mathrm{R_{outer}}}\sqrt{1 + \frac{3}{2}\frac{{\mathrm{R_{outer}}}^2}{\mathrm{ODD}^2}\left(\frac{P_{d,A(z)}}{\mathrm{R_{outer}}} - 1\right)}. \tag{4.8}$$

Using the approximation of $\sqrt{1+x}$,

$$\theta_0 \approx -\frac{2}{3}\frac{\mathrm{ODD}}{\mathrm{R_{outer}}} + \frac{2}{3}\frac{\mathrm{ODD}}{\mathrm{R_{outer}}}\left[1 + \frac{1}{2}\frac{3}{2}\frac{{\mathrm{R_{outer}}}^2}{\mathrm{ODD}^2}\left(\frac{P_{d,A(z)}}{\mathrm{R_{outer}}} - 1\right) - \cdots\right],$$
$$= \frac{1}{2}\frac{\mathrm{R_{outer}}}{\mathrm{ODD}}\left(\frac{P_{d,A(z)}}{\mathrm{R_{outer}}} - 1\right). \tag{4.9}$$

Thereby, the incident angle is

$$\theta_0 = \frac{P_{d,A(z)} - \mathrm{R}_{outer}}{2\,\mathrm{ODD}}. \tag{4.10}$$

Using Equations 4.4 through 4.10, intensity seen on the detector at a given height can be related to the incident angle on the irradiated surface.

4.2.2 Unobstructed Transmission Measurement

To further determine the complete image on the detector, the following subsections address the geometric equations for the remaining two beam paths.

In the case of transmissions that do not interact with an inner surface or in the absence of one, there are two interface refractions: one from the environment ($n_0 = 1 - \delta_0 - i\beta_0$) into the solid ($n_1 = 1 - \delta_1 - i\beta_1$) and one from the solid back into the environment. These refractions follow Snell's law with the recognition that the refractive index for X-rays is always less than one. This will lead to upward refractions as X-rays follow the opposite lensing to visible light; therefore, a constant radius convex lens will cause the beam to diverge. Figure 4.4 traces the rays through the material and depicts the angles that must be solved to find the location of the

transmitted rays at the detector.

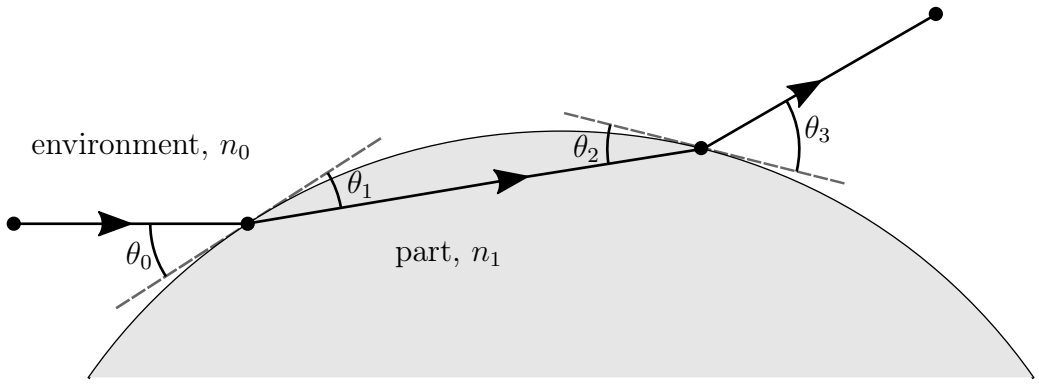

Figure 4.4: Tracing the transmitted ray through the part indicates two surface interactions for which the incident and refracted angles must be calculated. In this system, the index of refraction for the part environment is n_0 and the index of refraction for the homogeneous part material is n_1.

The relationships between θ_1 with respect to θ_0 and θ_3 with respect to θ_2 follow Snell's law:

$$\cos\theta_1 = \frac{n_0}{n_1}\cos\theta_0, \tag{4.11}$$

$$\cos\theta_3 = \frac{n_1}{n_0}\cos\theta_2. \tag{4.12}$$

The vector between the incident position and the output position, shown in Figure 4.5, can be defined as

$$\mathbf{R}_{12} = \mathbf{R}_{01} + \mathbf{r}_1, \tag{4.13}$$

where $\mathbf{R}_{01}$ and $\mathbf{R}_{12}$ are the vectors from the center of the part to the incident and output points, respectively. Additionally, it can be shown that the direction of the X-rays traveling through the material with respect to the x-axis is $\theta_0 - \theta_1$.

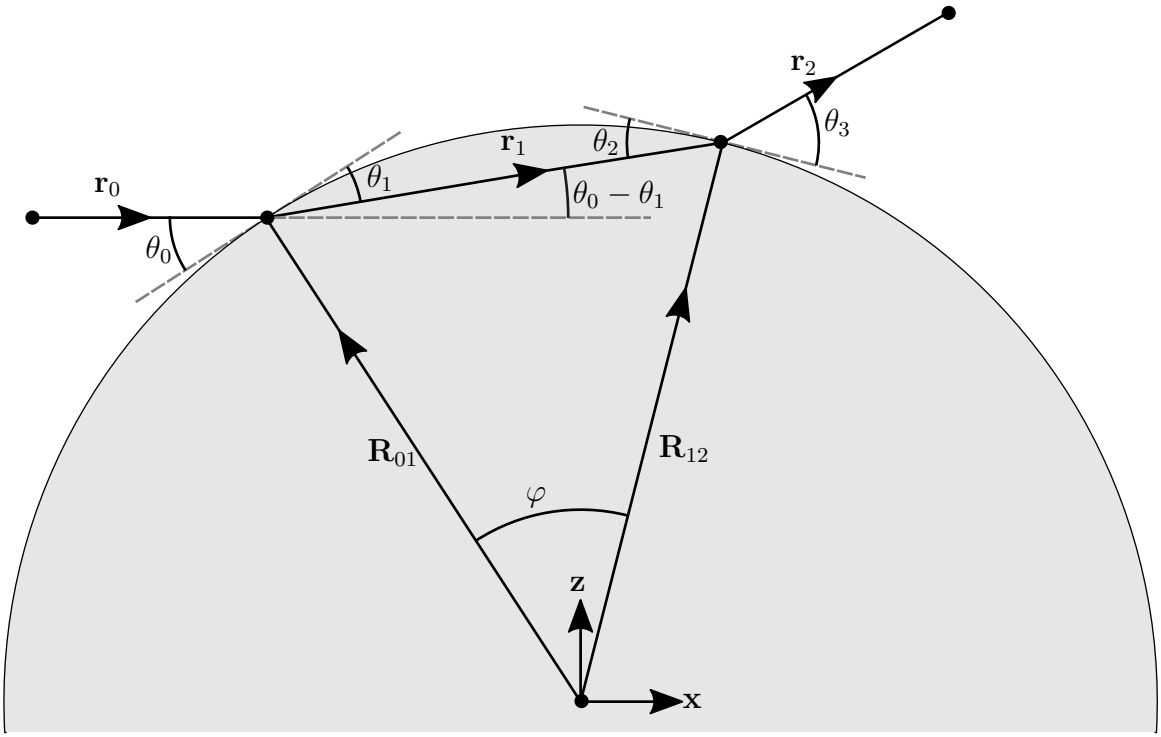

Figure 4.5: The full geometric representation of the transmitted rays; the definition of the vector $\mathbf{r}_1$ is necessary for the calculation of the path length and location of the transmitted X-rays when they interact with the inner surface of the part.

Figure 4.6 isolates the triangle formed by $\mathbf{R}_{01}$, $\mathbf{R}_{12}$, and $\mathbf{r}_1$. The magnitudes of $\mathbf{R}_{01}$ and $\mathbf{R}_{12}$ are the radius R_{outer} and the angle $\frac{\pi}{2} - \theta_1$ is known; therefore, θ_2 can be determined using the law of sines:

$$\begin{aligned} \frac{\mathrm{R}_{01}}{\mathrm{R}_{12}} = \frac{\mathrm{R}_{outer}}{\mathrm{R}_{outer}} = \frac{\sin\left(\frac{\pi}{2} - \theta_2\right)}{\sin\left(\frac{\pi}{2} - \theta_1\right)} = 1. \\ \theta_2 = \theta_1. \end{aligned} \tag{4.14}$$

Having identified the other two angles, the central angle can be defined:

$$\begin{aligned} \varphi &= \pi - \left(\frac{\pi}{2} - \theta_1\right) - \left(\frac{\pi}{2} - \theta_1\right) \\ &= 2\theta_1. \end{aligned} \tag{4.15}$$

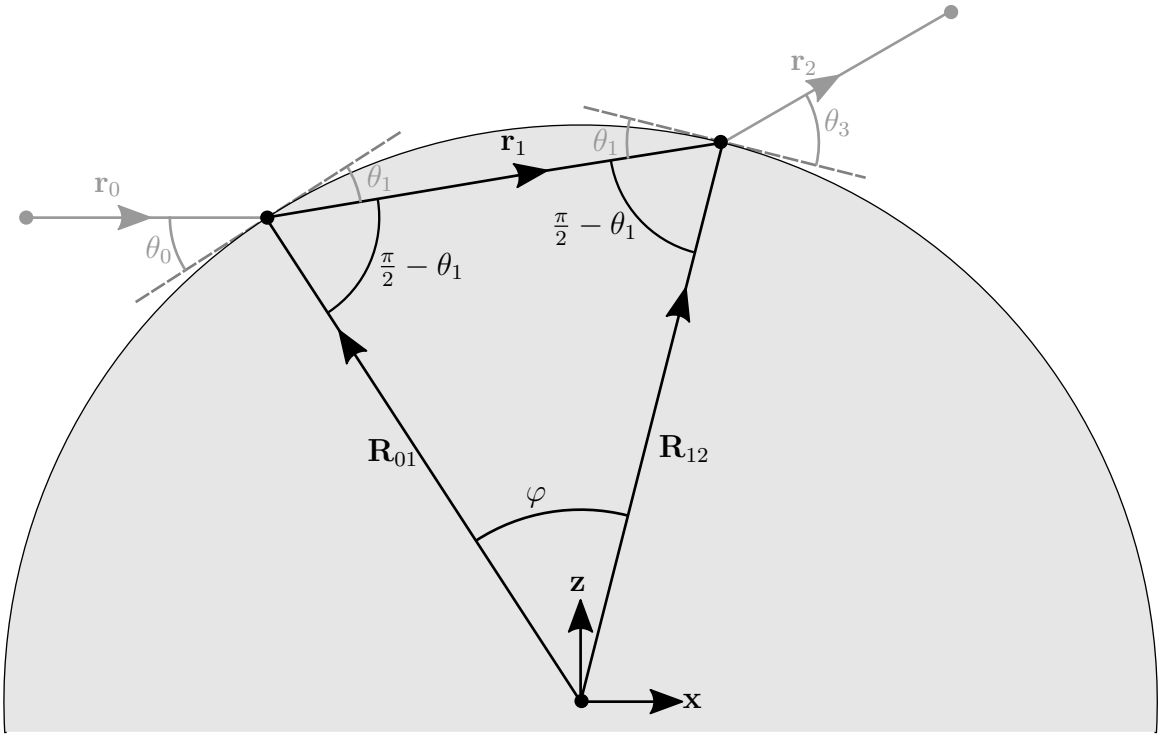

Figure 4.6: Isolating the triangle formed by $\mathbf{R}_{01}$, $\mathbf{R}_{12}$, and $\mathbf{r}_1$ allows for the definition of the subtended angle between the point at which the X-rays transmit into the part and the point at which the X-rays exit the part.

Therefore, the magnitude of $\mathbf{r}_1$ is

$$\mathrm{r}_1 = \mathrm{R}_{outer} \frac{\sin 2\theta_1}{\cos \theta_1} = 2\mathrm{R}_{outer} \sin \theta_1, \tag{4.16}$$

and the vector between the entrance and exit points for unobstructed transmitted X-rays is

$$\mathbf{r}_1 = 2\mathrm{R}_{outer} \sin \theta_1 \begin{bmatrix} \cos(\theta_0 - \theta_1) \\ 0 \\ \sin(\theta_0 - \theta_1) \end{bmatrix}; \tag{4.17}$$

where, the output position for case B is

$$P_{o,B} = P_i + \mathbf{r}_1. \tag{4.18}$$

Using Snell's law, θ_3 can be related to θ_2:

$$n_1 \cos\theta_2 = n_0 \cos\theta_3. \tag{4.19}$$

Additionally, from Equation 4.14, $\theta_2 = \theta_1$; therefore,

$$n_1 \cos\theta_1 = n_0 \cos\theta_3. \tag{4.20}$$

From Equation 4.11, $\cos\theta_1 = \frac{n_0}{n_1}\cos\theta_0$. This yields

$$\begin{aligned} \frac{n_1}{n_0}\frac{n_0}{n_1}\cos\theta_0 &= \cos\theta_3; \\ \theta_0 &= \theta_3. \end{aligned} \tag{4.21}$$

Focusing on the second interface, Figure 4.7, the angle of the X-rays exiting the part with respect to the incident beam (x-axis) for case b $\theta_{out,B}$ can be determined.

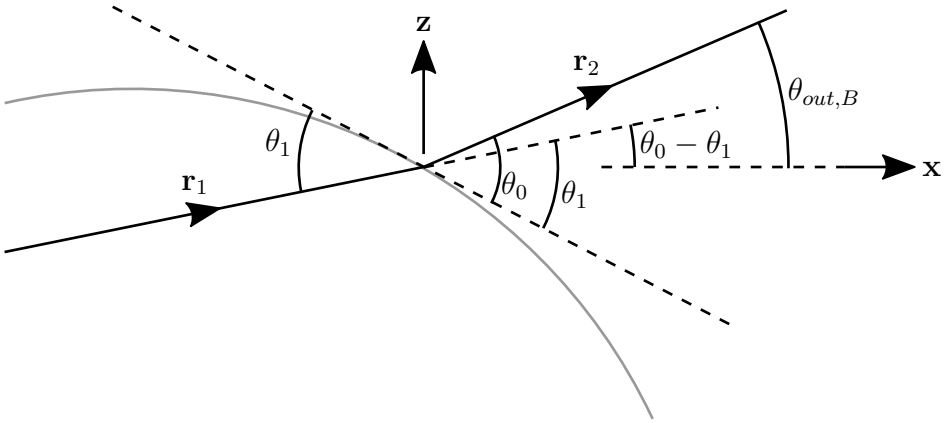

Figure 4.7: An isolated view of the second interface from which the output position for case b can be determined.

It can be seen that

$$\begin{aligned} \theta_{out,B} &= \theta_0 - \theta_1 + \theta_0 - \theta_1 \\ &= 2\theta_0 - 2\theta_1. \end{aligned} \tag{4.22}$$

Figure 4.8 defines the geometry of a transmitted beam as it travels through the part where $P_{d,B}$ is the position of the output X-rays for case B on the detector for a given ODD.

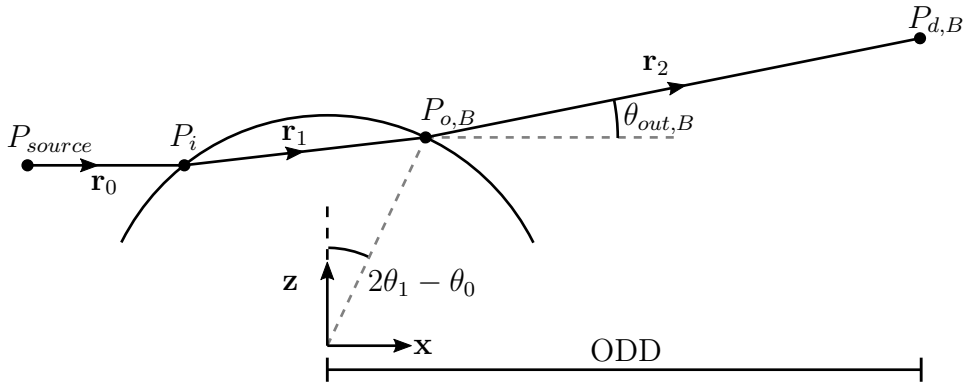

Figure 4.8: Full definition of the path a transmitted X-ray will take through a circular part. To trace the path, the exit point $P_{o,B}$ and the point of interaction with the detector $P_{d,B}$ must be determined.

From Figure 4.8, the location of the unobstructed transmitted X-rays as they arrive at the detector can be determined. The detector is at x-coordinate ODD and the z-component can be found with the position and the angle of the exiting X-rays. The position of the transmitted X-rays for case b on the detector is

$$P_{d,B} = \begin{pmatrix} \text{ODD} \\ 0 \\ P_{o,B(z)} + (\text{ODD} - P_{o,B(x)}) \tan\theta_{out,B} \end{pmatrix}. \tag{4.23}$$

Therefore, the vector from the exit point to the detector is defined

$$\mathbf{r}_2 = P_{d,B} - P_{o,B}. \tag{4.24}$$

4.2.3 Internal Surface Reflections

For a circular part having an internal, concentric shell with material index of refraction $n_2 = 1 - \delta_2 - i\beta_2$, X-rays transmitted into the part may reflect off of this shell and transmit out of the part to the detector. Figure 4.9 depicts the path that

X-rays reflected from the inner surface will follow and the angle definitions needed to determine this path.

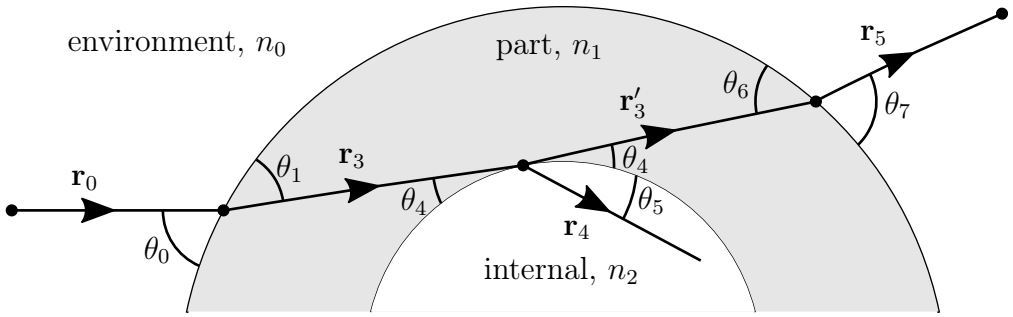

Figure 4.9: The geometric representation of an X-ray reflection from the inner surface of a part of constant curvature. As in the previous sections, the index of refraction of the environment is n_0 and the part is n_1. The index of refraction of the internal material is n_2. Incident X-rays transmit through the outer surface, reflect from the inner surface, and transmit back through the outer surface. Proper modelling of the direction and distance traveled of these rays is required to determine the amplitude, phase, and position of the resulting X-rays at the detector.

The first concern is the condition in which the X-rays will be incident upon the inner surface. Not every transmitted X-ray will interact with a shell of a given radius; only cases for which the angle between the initially transmitted light and the inner surface θ_4 is greater than zero. Figure 4.10 defines the path between the outer interface and the inner face for transmitted X-rays $\mathbf{r}_3$. This path definition can be used to determine θ_4 given the inner radius R_{inner} and outer radius R_{outer} are known.

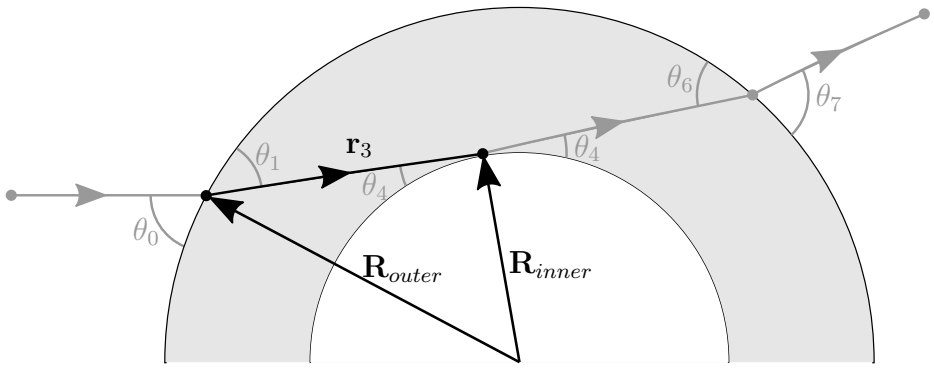

Figure 4.10: The path between the outer surface and the inner surface is defined as $\mathbf{r}_3$. This is only a plausible path if the transmitted ray will be incident upon the inner surface.

The triangle created with $\mathbf{R}_{inner}$, $\mathbf{R}_{outer}$, and $\mathbf{r}_3$ can be isolated to solve for θ_4. This isolation is shown in Figure 4.11.

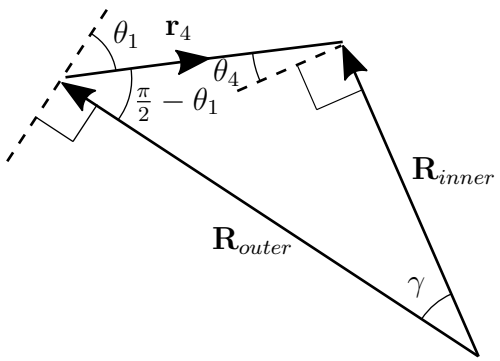

Figure 4.11: An isolated view of the path between the outer surface and the inner surface. To solve for θ_4, the angle subtended by $\mathbf{r}_3$ from the center of the part must be determined.

Employing the law of sines, the relationship for θ_4 is

$$\frac{\mathrm{R}_{outer}}{\mathrm{R}_{inner}} = \frac{\sin\left(\theta_4 + \frac{\pi}{2}\right)}{\sin\left(\frac{\pi}{2} - \theta_1\right)} = \frac{\cos\theta_4}{\cos\theta_1}.$$
$$\cos\theta_4 = \frac{\mathrm{R}_{outer}}{\mathrm{R}_{inner}}\cos\theta_1. \tag{4.25}$$

From Snell's Law, the refracted angle θ_5 is

$$\cos\theta_5 = \frac{n_1}{n_2}\cos\theta_4. \tag{4.26}$$

Solving for θ_4 allows for the condition for internal reflections to be made. The X-rays will be incident upon the inner surface only if $\theta_4 \geq 0$; therefore, the lower-bound of the condition for incidence is

$$\frac{\mathrm{R}_{outer}}{\mathrm{R}_{inner}}\cos\theta_1 = 0$$
$$\cos\theta_0 = \frac{\mathrm{R}_{outer}}{\mathrm{R}_{inner}}\frac{n_1}{n_2}. \tag{4.27}$$

Physically, θ_4 will not exceed $\pi/2$; therefore, the condition for incidence is

$$\arccos\left(\frac{\mathrm{R}_{outer}}{\mathrm{R}_{inner}}\frac{n_1}{n_2}\right) \leq \theta_0 \leq \frac{\pi}{2}. \tag{4.28}$$

From Figure 4.11, it can be seen that the angle spanning $\mathbf{R}_{inner}$ and $\mathbf{R}_{outer}$ is

$$\gamma = \pi - \left(\frac{\pi}{2} - \theta_1\right) - \left(\theta_4 + \frac{\pi}{2}\right) = \theta_1 - \theta_4. \tag{4.29}$$

Again employing the law of sines, the magnitude of the path from the outer surface to the inner surface r_3 can be determined

$$\mathrm{r}_3 = \frac{\sin\gamma}{\sin\left(\frac{\pi}{2} - \theta_1\right)}\mathrm{R}_{inner} = \frac{\sin\left(\theta_1 - \theta_4\right)}{\cos\left(\theta_1\right)}\mathrm{R}_{inner}. \tag{4.30}$$

The direction of $\mathbf{r}_3$ is the same as $\mathbf{r}_1$ from the previous section; therefore,

$$\mathbf{r}_3 = \mathrm{r}_3 \begin{bmatrix} \cos\left(\theta_0 - \theta_1\right) \\ 0 \\ \sin\left(\theta_0 - \theta_1\right) \end{bmatrix}. \tag{4.31}$$

Figure 4.12 defines the exit path between the inner surface and the outer surface for X-rays that scatter from the inner surface.

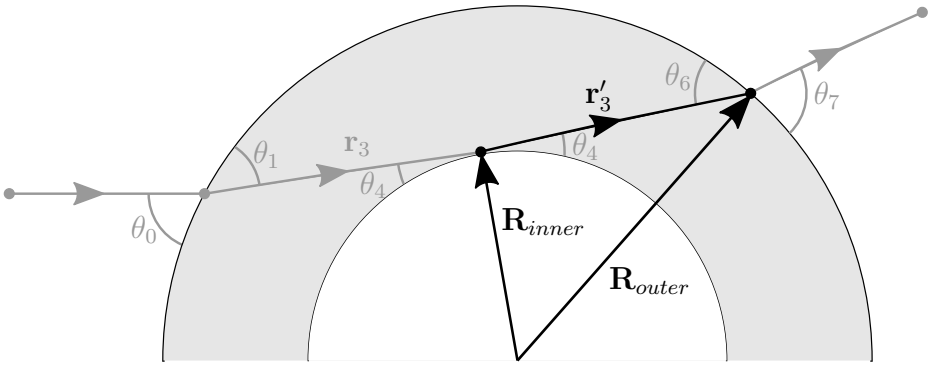

Figure 4.12: For X-rays scattered from the inner surface, the exit path from the inner surface to the outer surface is defined as $\mathbf{r}'_3$.

Figure 4.13 shows an isolated view of the triangle created by $\mathbf{R}_{outer}$, $\mathbf{R}_{outer}$, and $\mathbf{r}'_3$.

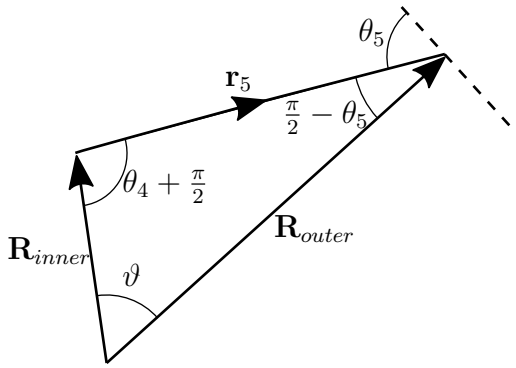

Figure 4.13: An isolated view of the exit path between the inner surface and the outer surface. The magnitude and direction of this exit path can be found by solving for the subtended angle ϑ.

Employing the law of sines, the relationship between θ_4 and θ_6 is

$$\frac{\mathrm{R}_{inner}}{\mathrm{R}_{outer}} = \frac{\sin\left(\frac{\pi}{2} - \theta_5\right)}{\sin\left(\theta_4 + \frac{\pi}{2}\right)} = \frac{\cos\theta_6}{\cos\theta_4}.$$
$$\cos\theta_6 = \frac{\mathrm{R}_{inner}}{\mathrm{R}_{outer}}\cos\theta_4. \tag{4.32}$$

It follows that the angle spanning $\mathbf{R}_{inner}$ and $\mathbf{R}_{outer}$ is

$$\pi = \theta_4 + \frac{\pi}{2} + \frac{\pi}{2} - \theta_6 + \vartheta$$
$$\vartheta = \theta_6 - \theta_4; \tag{4.33}$$

therefore, the magnitude of the exit path from the inner surface to the outer surface r'_3 is

$$\mathrm{r}'_3 = \frac{\sin\vartheta}{\sin\left(\frac{\pi}{2} - \theta_6\right)}\mathrm{R}_{inner} = \frac{\sin\left(\theta_6 - \theta_4\right)}{\cos\left(\theta_6\right)}\mathrm{R}_{inner}. \tag{4.34}$$

The direction of $\mathbf{r}'_3$ is the direction of $\mathbf{r}_3$ increased by $2\theta_4$ in the z-direction. The propagation vector for scattered X-rays from the inner surface to the outer surface is

therefore:

$$\mathbf{r}'_3 = \mathrm{r}'_3 \begin{bmatrix} \cos(\theta_0 - \theta_1 + 2\theta_4) \\ 0 \\ \sin(\theta_0 - \theta_1 + 2\theta_4) \end{bmatrix}. \tag{4.35}$$

From Snell's law, the relationship between θ_6 and θ_7 can be determined:

$$\cos\theta_7 = \frac{n_1}{n_0}\cos\theta_6. \tag{4.36}$$

From Figure 4.14, it can be seen that the output angle for case c between the x-axis and $\mathbf{r}_5$ is

$$\theta_{out,C} = \theta_0 - \theta_1 + 2\theta_4 + \theta_7 - \theta_6. \tag{4.37}$$

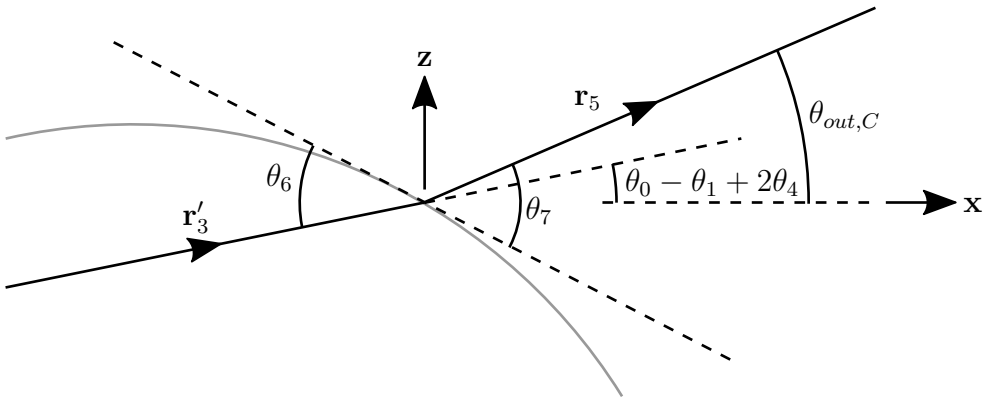

Figure 4.14: An isolated view of the outer interface allows for the determination of the output angle of $\mathbf{r}_5$ with respect to the x-axis.

The position of the X-rays exiting the part can be determined by following the path vectors through the part:

$$P_{o,C} = P_i + \mathbf{r}_3 + \mathbf{r}'_3. \tag{4.38}$$

Additionally, the horizontal distance from the part center to the detector is defined ODD (object detector distance) and can be used to find the height of the X-rays on

the detector

$$P_{d,C} = \begin{pmatrix} \text{ODD} \\ 0 \\ P_{o,C(z)} + \left(\text{ODD} - P_{o,C(x)}\right) \tan\theta_{out,C} \end{pmatrix}. \tag{4.39}$$

The vector from the exit point to the detector is then

$$\mathbf{r}_5 = P_{d,C} - P_{o,C}. \tag{4.40}$$

Finally, Figure 4.15 can be fully defined for the path X-rays will travel through a shell of circular cross-section.

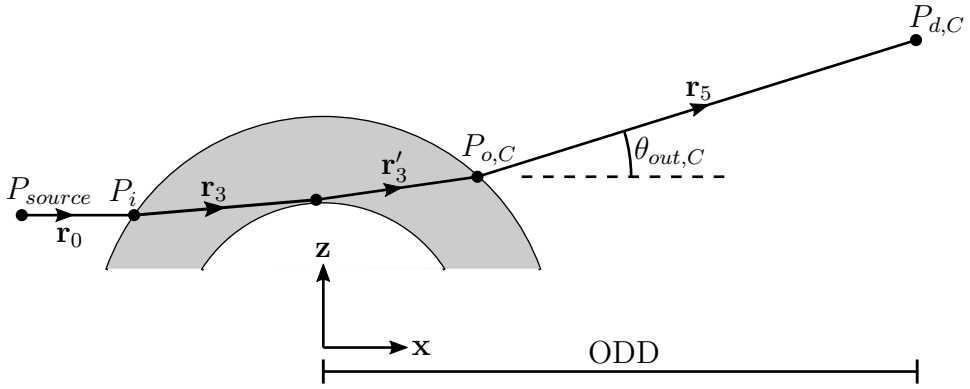

Figure 4.15: Full definition of the path taken by X-rays transmitted into the part and reflected from the inner surface.

4.3 Field Calculations

To determine the intensity of the X-rays at the detector, it is necessary to model the field amplitude and phase for each ray as it interacts with the part. There are three cases considered: case A defines reflections from the exterior surface (interface ^{01}), case B defines transmissions into the part (interface ^{01}) and transmissions back out of the part (interface ^{12}), and case C defines transmissions into the part (interface ^{01}) followed by reflections from an internal surface (interface ^{34}) and transmissions back out of the part (interface $^{3'5}$). Figure 4.16 depicts the electric field definitions for the three cases.

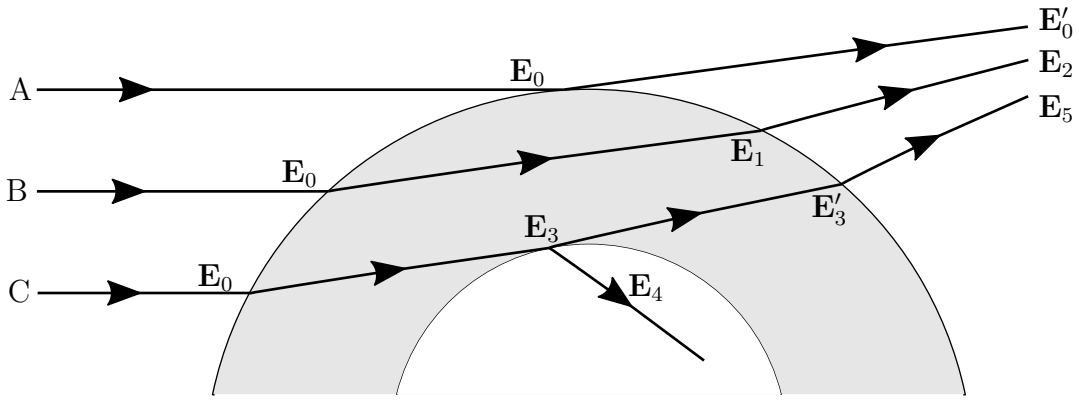

Figure 4.16: As the X-rays propagate through the part, the electric field vector changes. These changes are tracked in the subscripts of the field vector symbol.

4.3.1 External Surface Reflections

First, the reflections from the outer surface can be defined, shown in Figure 4.17. The incident X-ray beam can be defined using the incident wave-vector $\mathbf{k}_0$ and the incident electric field $\mathbf{E}_0$.

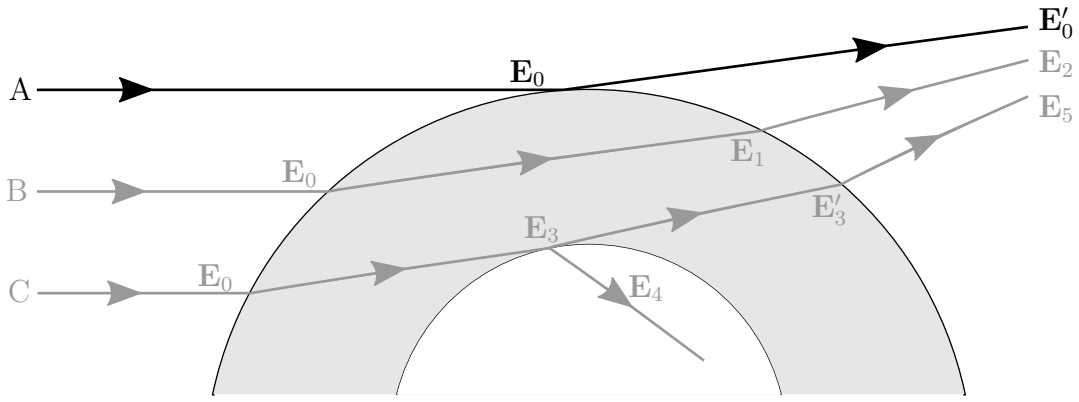

Figure 4.17: Emphasized view of Case A, tracing the path of the reflected X-rays.

Figure 4.18 defines the incident, reflected, and transmitted X-rays for interface ^{01}.

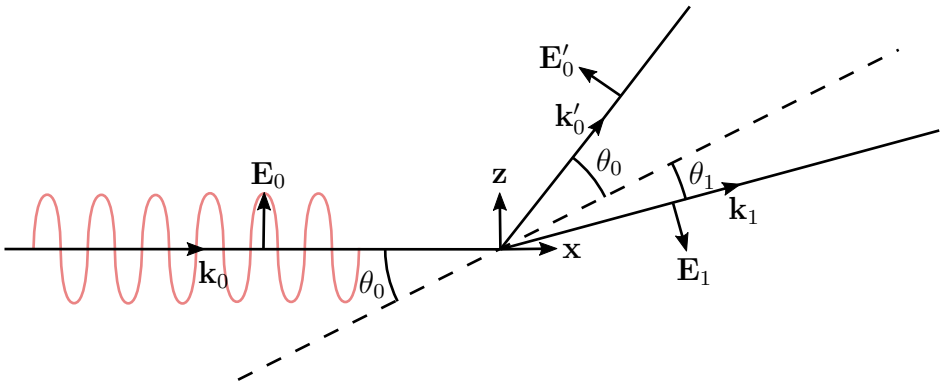

Figure 4.18: Geometric representation of the X-ray interaction with interface ^{01}. $\mathbf{E}_0$ is the electric field of the incident X-rays, $\mathbf{E}'_0$ is the electric field of the reflected X-rays, and $\mathbf{E}_1$ is the electric field of the refracted X-rays. $\mathbf{k}_0$, $\mathbf{k}'_0$, and $\mathbf{k}_1$ are the wave-vectors, and θ_0 is the incident and specular reflection angle with respect to the interface, and θ_1 is the refracted angle.

The electric field vector for the X-rays from the source at the part is given by

$$\mathbf{E}_0 = \mathbf{A}_0 \exp\left(i\,\mathbf{k}_0 \cdot \mathbf{r}_0\right). \tag{4.41}$$

The incident radiation is assumed to be linearly polarized and can be decomposed into electric field components parallel to the scattering plane $E_{0(x)}$ and $E_{0(y)}$ (p-polarization) and perpendicular to the scattering plane $E_{0(z)}$ (s-polarization). Assuming a linear polarization angle of χ, the components of the incident amplitude

are

$$\mathbf{A}_0 = \mathrm{A}_0 \begin{bmatrix} -\sin\chi\sin 2\theta_0 \\ \cos\chi \\ \sin\chi\cos 2\theta_0 \end{bmatrix}. \tag{4.42}$$

From Figure 4.18, the incident wave vector can be defined as

$$\mathbf{k}_0 = \begin{bmatrix} k_{0(x)} \\ k_{0(y)} \\ k_{0(z)} \end{bmatrix} = \begin{bmatrix} k \\ 0 \\ 0 \end{bmatrix}, \tag{4.43}$$

where k is the wave number of the incident radiation given by

$$k = \frac{2\pi}{\lambda} = \frac{\omega}{c}, \tag{4.44}$$

for which λ is the source wavelength, ω is the source frequency, and c is the constant speed of light. The phase of the incident light, given by the second term in Equation 4.41, changes with distance $\mathbf{r}_0$ between the source and the surface.

In general, the wave-vector is related to the refractive index by

$$\frac{\mathbf{k}_j \cdot \mathbf{k}_j}{n_j^2} = \frac{\omega^2}{c^2} = \text{constant}; \tag{4.45}$$

therefore, the magnitude of the transmitted wave-vector, $\mathbf{k}_1$, can be found using the incident wave-vector, the index of refraction of the part, n_1, and the index of refraction of the environment, n_0. Using Equation 4.45,

$$\frac{\|\mathbf{k}_1\|^2}{n_1^2} = \frac{\|\mathbf{k}_0\|^2}{n_0^2}; \tag{4.46}$$

therefore, the magnitude of the transmitted wave-vector is

$$\|\mathbf{k}_1\| = \frac{n_1}{n_0}k, \tag{4.47}$$

and

$$\frac{\|\mathbf{k}_0'\|}{n_0^2} = \frac{\|\mathbf{k}_0\|}{n_1^2} = k. \tag{4.48}$$

From Figure 4.18, and Equations 4.47 and 4.48, the wave-vectors can be defined:

$$\mathbf{k}_0' = k \begin{bmatrix} \cos 2\theta_0 \\ 0 \\ \sin 2\theta_0 \end{bmatrix}, \tag{4.49}$$

$$\mathbf{k}_1 = \frac{n_1}{n_0} k \begin{bmatrix} \cos(\theta_0 - \theta_1) \\ 0 \\ \sin(\theta_0 - \theta_1) \end{bmatrix}. \tag{4.50}$$

The amplitude of the reflected $\mathbf{A}_0'$ and transmitted $\mathbf{A}_1$ components of the incident beam are found using the Fresnel coefficients represented here as a tensor of reflection $\boldsymbol{\Psi}$ and refraction $\boldsymbol{\Phi}$ components. The amplitudes are related by

$$\begin{bmatrix} \mathbf{A}_0' \\ \mathbf{A}_1 \end{bmatrix} = \begin{bmatrix} {}^{01}\boldsymbol{\Psi} & {}^{10}\boldsymbol{\Phi} \\ {}^{01}\boldsymbol{\Phi} & {}^{10}\boldsymbol{\Psi} \end{bmatrix} \begin{bmatrix} \mathbf{A}_0 \\ \mathbf{A}_1' \end{bmatrix}. \tag{4.51}$$

The coefficient superscripts denote the direction of the X-rays with respect to the interface, i.e. $\boldsymbol{\Psi}_{01}$ refers to the reflection coefficient matrix for X-rays travelling from layer "0" (the environment) toward layer "1" (the part). Additionally, $\mathbf{A}_1'$ is considered to be the amplitude of X-rays incident upon the interface from below and is referred to as the *time-reversed scattered beam* which in this case has zero amplitude. Hence, the amplitudes of the reflected and refracted beams are

$$\mathbf{A}_0' = {}^{01}\boldsymbol{\Psi}\mathbf{A}_0; \tag{4.52}$$

$$\mathbf{A}_1 = {}^{01}\boldsymbol{\Phi}\mathbf{A}_0. \tag{4.53}$$

The Fresnel coefficient tensor for the reflection is given by

$$ {}^{01}\mathbf{\Psi} = \begin{bmatrix} {}^{01}\Psi_{(x)} & 0 & 0 \\ 0 & {}^{01}\Psi_{(y)} & 0 \\ 0 & 0 & {}^{01}\Psi_{(z)} \end{bmatrix}, \tag{4.54} $$

with

$$ \begin{aligned} {}^{01}\Psi_{(x)} &= \frac{{}^{01}k_{1(z)}(\mathbf{k}_0 \cdot \mathbf{k}_0) - {}^{01}k_{0(z)}(\mathbf{k}_1 \cdot \mathbf{k}_1)}{{}^{01}k_{0(z)}(\mathbf{k}_1 \cdot \mathbf{k}_1) + {}^{01}k_{1(z)}(\mathbf{k}_0 \cdot \mathbf{k}_0)}, \\ {}^{01}\Psi_{(y)} &= \frac{{}^{01}k_{0(z)} - {}^{01}k_{1(z)}}{{}^{01}k_{0(z)} + {}^{01}k_{1(z)}}, \\ {}^{01}\Psi_{(z)} &= -{}^{01}\Psi_{(x)}. \end{aligned} \tag{4.55} $$

Here, the components of the wave-vectors denoted with a superscript ^{01} refer to the wave-vector *with respect to the first interface*. These wave-vectors are

$$ {}^{01}\mathbf{k}_0 = k \begin{bmatrix} \cos\theta_0 \\ 0 \\ -\sin\theta_0 \end{bmatrix}, \tag{4.56} $$

$$ {}^{01}\mathbf{k}_1 = \frac{n_1}{n_0} k \begin{bmatrix} \cos\theta_1 \\ 0 \\ -\sin\theta_1 \end{bmatrix}. \tag{4.57} $$

Additionally,

$$ \mathbf{k}_0 \cdot \mathbf{k}_0 = k^2 \tag{4.58} $$

$$ \mathbf{k}_1 \cdot \mathbf{k}_1 = k^2 \left(n_1/n_0\right)^2. \tag{4.59} $$

From which the coefficients can be solved

$$ {}^{01}\Psi_{(x)} = \frac{n_0 \sin\theta_1 - n_1 \sin\theta_0}{n_0 \sin\theta_1 + n_1 \sin\theta_0} = -{}^{01}\Psi_{(z)}, \tag{4.60} $$

$$ {}^{01}\Psi_{(y)} = \frac{n_0 \sin\theta_0 - n_1 \sin\theta_1}{n_0 \sin\theta_0 + n_1 \sin\theta_1}. \tag{4.61} $$

Surface roughness will reduce the intensity of the scattered radiation by a factor $f(\sigma)$ where σ is the root-mean-square (RMS) roughness of the interface. The consequence of surface roughness is the scatter is no longer strictly specular but also has an off-specular (diffuse) component. There are many models that can be used to approximate the change in intensity due to surface roughness, Table 4.1 lists a few common factors.

Table 4.1: Common roughness models in literature with the ranges of $\mathbf{k}$ for which they fit best. These factors influence the intensity of the reflected light from a surface having RMS surface roughness σ. The reflected amplitude therefore is reduced by $\sqrt{f(\sigma)}$.

Névot and Croce (NC) [13, 22]	$f(\sigma) = \exp(-2k_{0(z)}k_{1(z)}\sigma^2)$	$k\sigma \leq 1$
Debye-Waller (DW) [36]	$f(\sigma) = \exp(-2{k_{0(z)}}^2\sigma^2)$	$k\sigma >> 1$
second-order distorted wave Born approximation (DWBA) [28]	$f(\sigma) = \exp(1 - 2{k_{0(z)}}^2\sigma^2)$	most $\mathbf{k}_0$
Sinha et al. [18]	$f(\sigma) = \exp(-4k^2 \sin\theta_0 \sin\theta_1 \sigma^2)$	low at small $\mathbf{k}_0$, high at large $\mathbf{k}_0$

The phase of the reflected light at the detector depends on the path length $\mathbf{r}'_0$ of the reflected rays, defined in Equation 4.5. The field of the X-rays reflected from the outer surface is

$$\mathbf{E}'_0 = {}^{01}\boldsymbol{\Psi}\mathbf{E}_0 \exp\left(i\,\mathbf{k}'_0 \cdot \mathbf{r}'_0\right)\sqrt{f(\sigma)}. \tag{4.62}$$

4.3.2 Unobstructed Transmissions

Next, the field at the detector for X-rays that transmit through the part must be found. Figure 4.19 shows the fields that must be defined to determine the final field at the detector $\mathbf{E}_2$. The Fresnel coefficient tensor for refraction at the interface is given by

$${}^{01}\boldsymbol{\Phi}_{01} = \begin{bmatrix} {}^{01}\Phi_{(x)} & 0 & 0 \\ 0 & {}^{01}\Phi_{(y)} & 0 \\ 0 & 0 & {}^{01}\Phi_{(z)} \end{bmatrix}, \tag{4.63}$$

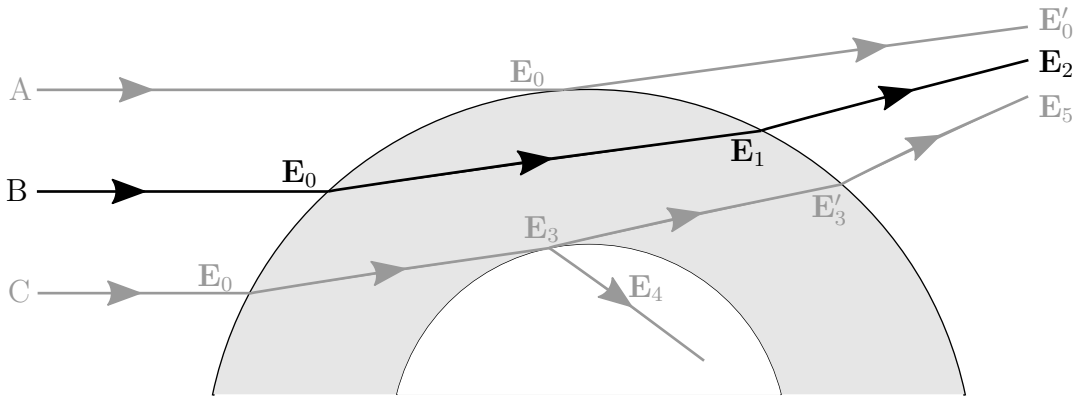

Figure 4.19: Emphasized view of case B, tracing the path of the transmitted X-rays.

for which, using Equations 4.58 and 4.59,

$$ {}^{01}\Phi_{(x)} = 2\,\frac{{}^{01}k_{1(z)}\,(\mathbf{k}_0\cdot\mathbf{k}_0)}{{}^{01}k_{0(z)}\,(\mathbf{k}_1\cdot\mathbf{k}_1)+{}^{01}k_{1(z)}\,(\mathbf{k}_0\cdot\mathbf{k}_0)} = \frac{2n_0\sin\theta_1}{n_0\sin\theta_1+n_1\sin\theta_0}, \tag{4.64} $$

$$ {}^{01}\Phi_{(y)} = 2\,\frac{{}^{01}k_{0(z)}}{{}^{01}k_{0(z)}+{}^{01}k_{1(z)}} = \frac{2n_0\sin\theta_0}{n_0\sin\theta_0+n_1\sin\theta_1}, \tag{4.65} $$

$$ {}^{01}\Phi_{(z)} = 2\,\frac{{}^{01}k_{0(z)}\,(\mathbf{k}_0\cdot\mathbf{k}_0)}{{}^{01}k_{0(z)}\,(\mathbf{k}_1\cdot\mathbf{k}_1)+{}^{01}k_{1(z)}\,(\mathbf{k}_0\cdot\mathbf{k}_0)} = \frac{2(n_0/n_1)\sin\theta_0}{(n_1/n_0)\sin\theta_0+\sin\theta_1}. \tag{4.66} $$

The X-rays that travel through the part in case B uninterrupted by the inner shell (or in the absence of one) will be attenuated as they travel through the material. This attenuation is a function of an absorption coefficient, μ, and the distance the X-rays travel through the material. The absorption coefficient is a function of the radiation wavelength and the material refractive index and is given by

$$ \mu = k\beta_1. \tag{4.67} $$

Recalling that the distance the X-rays travel through the material, r_1, is derived in Equation 4.17, the transmitted *amplitude* attenuation factor is $\exp(-\mu r_1/2)$.

The field at the second interface can now be defined as:

$$ \mathbf{E}_1 = {}^{01}\mathbf{\Phi}\mathbf{E}_0\exp\left(i\,\mathbf{k}_1\cdot\mathbf{r}_1\right)\exp\left(-\mu r_1/2\right). \tag{4.68} $$

To determine the field at the detector for case B, $\mathbf{E}_2$, the field interactions at the ^{12} interface must be determined. Figure 4.20 defines the second interface.

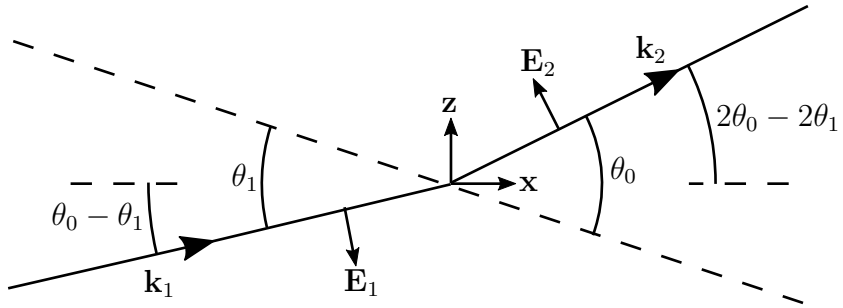

Figure 4.20: Definition of the field interactions at the second interface. The wave-vectors can be defined with the angles of interaction of the incident and refracted X-rays.

From Figure 4.20, the transmitted wave-vector $\mathbf{k}_2$ can be defined

$$\mathbf{k}_2 = k \begin{bmatrix} \cos(2\theta_0 - 2\theta_1) \\ 0 \\ \sin(2\theta_0 - 2\theta_1) \end{bmatrix}. \tag{4.69}$$

As before, the reflection and refraction of the X-rays at the second interface can be found by multiplying by the Fresnel coefficient tensors for the ^{12} interface,

$$\begin{bmatrix} \mathbf{A}_1' \\ \mathbf{A}_2 \end{bmatrix} = \begin{bmatrix} {}^{12}\mathbf{\Psi} & {}^{21}\mathbf{\Phi} \\ {}^{12}\mathbf{\Phi} & {}^{21}\mathbf{\Psi} \end{bmatrix} \begin{bmatrix} \mathbf{A}_1 \\ \mathbf{A}_2' \end{bmatrix}. \tag{4.70}$$

$\mathbf{A}_1'$ is the amplitude of the X-rays reflected from the second interface. These X-rays will not reach the detector and are therefore irrelevant to the measurement. Additionally $\mathbf{A}_2'$ is the *time-reversed scattered beam* and has zero amplitude. Therefore,

$$\mathbf{A}_2 = {}^{12}\mathbf{\Psi}\mathbf{A}_1. \tag{4.71}$$

The coefficient for refraction at the interface is

$$ {}^{12}\mathbf{\Phi} = \begin{bmatrix} {}^{12}\Phi_{(x)} & 0 & 0 \\ 0 & {}^{12}\Phi_{(y)} & 0 \\ 0 & 0 & {}^{12}\Phi_{(z)} \end{bmatrix}. \tag{4.72} $$

The Fresnel coefficients of refraction for the ^{12} interface are

$$ {}^{12}\Phi_{(x)} = 2\,\frac{{}^{12}k_{2(z)}\,(\mathbf{k}_1 \cdot \mathbf{k}_1)}{{}^{12}k_{1(z)}\,(\mathbf{k}_2 \cdot \mathbf{k}_2) + {}^{12}k_{2(z)}\,(\mathbf{k}_1 \cdot \mathbf{k}_1)} \tag{4.73} $$

$$ {}^{12}\Phi_{(y)} = 2\,\frac{{}^{12}k_{1(z)}}{{}^{12}k_{1(z)} + {}^{12}k_{2(z)}}, \tag{4.74} $$

$$ {}^{12}\Phi_{(z)} = 2\,\frac{{}^{12}k_{1(z)}\,(\mathbf{k}_1 \cdot \mathbf{k}_1)}{{}^{12}k_{1(z)}\,(\mathbf{k}_2 \cdot \mathbf{k}_2) + {}^{12}k_{2(z)}\,(\mathbf{k}_1 \cdot \mathbf{k}_1)} \tag{4.75} $$

Here, the superscript ^{12} represents the wave-vector as defined *with respect to the second interface*. The dot product $\mathbf{k}_1 \cdot \mathbf{k}_1$ is solved in Equation 4.59. Furthermore, from Figure 4.20, the wave-vectors with respect to the interface are

$$ {}^{12}\mathbf{k}_1 = \frac{n_1}{n_0} k \begin{bmatrix} \cos\theta_1 \\ 0 \\ \sin\theta_1 \end{bmatrix}, \tag{4.76} $$

$$ {}^{12}\mathbf{k}_2 = k \begin{bmatrix} \cos\theta_0 \\ 0 \\ \sin\theta_0 \end{bmatrix}. \tag{4.77} $$

Thus, the coefficients of $^{12}\mathbf{\Psi}$ can be simplified

$$ {}^{12}\Phi_{(x)} = \frac{2(n_1/n_0)\sin\theta_0}{\sin\theta_1 + (n_1/n_0)\sin\theta_0}, \tag{4.78} $$

$$ {}^{12}\Phi_{(y)} = \frac{2(n_1/n_0)\sin\theta_1}{(n_1/n_0)\sin\theta_1 + \sin\theta_0}, \tag{4.79} $$

$$ {}^{12}\Phi_{(z)} = \frac{2(n_1/n_0)^2\sin\theta_1}{\sin\theta_1 + (n_1/n_0)\sin\theta_0}. \tag{4.80} $$

The field at the detector for the X-rays transmitted through the part and unob-

structed by an inner surface is:

$$\mathbf{E}_2 = {}^{12}\mathbf{\Phi}\mathbf{E}_1 \exp\left(i\,\mathbf{k}_2 \cdot \mathbf{r}_2\right). \tag{4.81}$$

The intensity of the X-rays at the detector is magnitude of the electric field such that the intensity of the reflected radiation is:

$$\mathrm{I}_0' = \mathbf{E}_0' \cdot \mathbf{E}_0', \tag{4.82}$$

and the intensity of the transmitted radiation is

$$\mathrm{I}_2 = \mathbf{E}_2 \cdot \mathbf{E}_2. \tag{4.83}$$

Figure 4.21 presents the intensity of the reflections and the transmission from a Silicon part of 1.5 m radius having no surface roughness. These two component intensities overlap on the detector to give a total measured intensity.

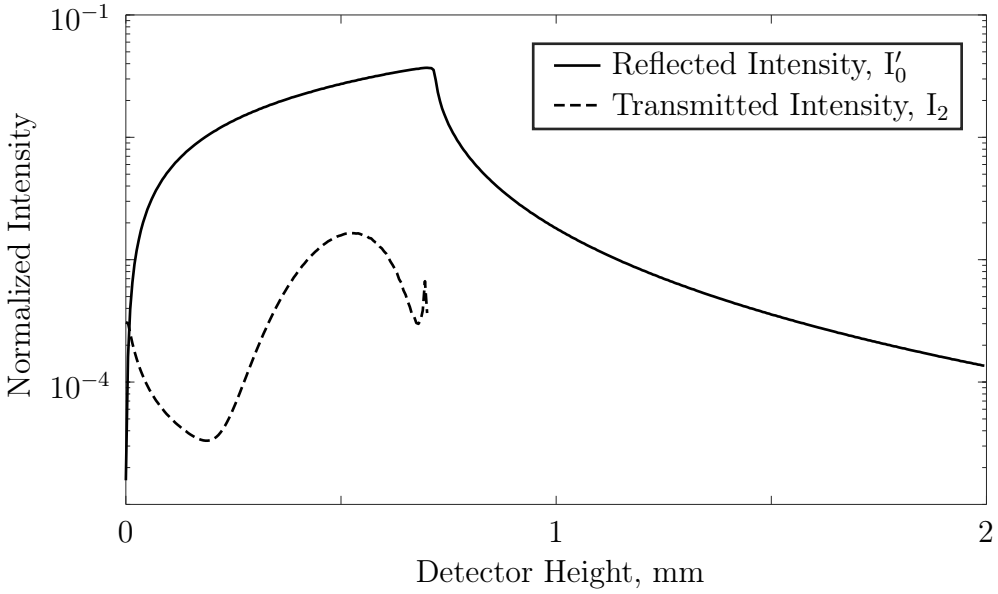

Figure 4.21: Output intensity of the reflected, I_0', and transmitted, I_2 X-rays from a Silicon part of 1.5 m radius with no surface roughness.

From Equation 4.62, surface roughness plays an important role in the intensity of the reflections and therefore the image on the detector. Figure 4.22 depicts the influence of surface roughness on the intensity on the detector. As reflections dominate the intensity on the detector for large detector height, surface roughness contributes to a reduction of the overall intensity.

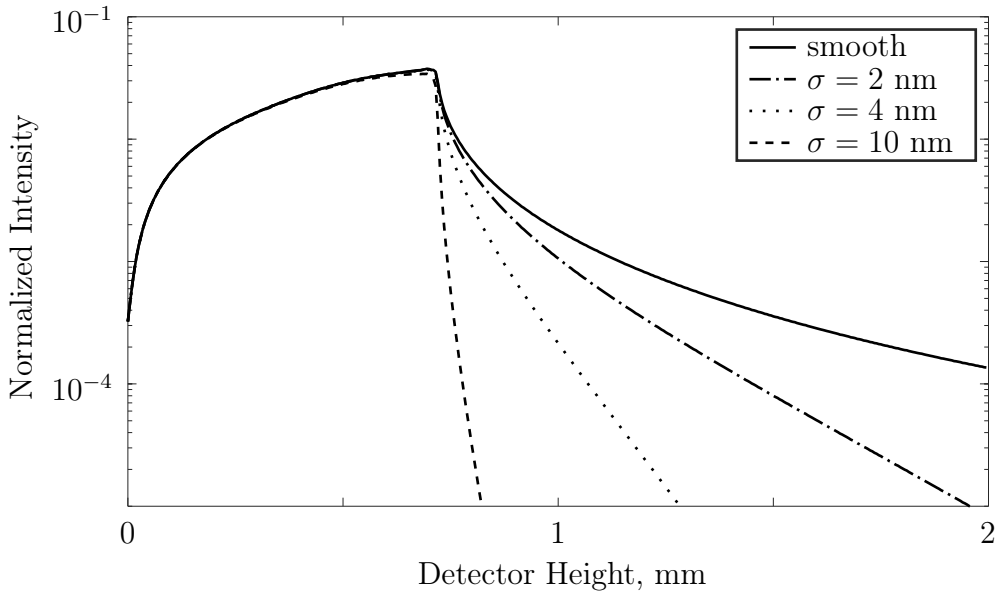

Figure 4.22: The comparison of various surface roughness on a Silicon part of 1.5 m radius. Higher surface roughness contributes to a higher decay rate of reflectivity.

For a part of large radius, finite steps in z result in small steps in incident angle; whereas, for small radii the incident angle changes quickly with z. Hence, the average incident angle for a finite percentage of beam is larger for parts of small radius therefore spreading the same amount of beam over a larger area on the detector and reducing the part's reflectivity. Figure 4.23 depicts the influence of outer radius on the reflectivity of the part. It is noted that for large changes in part radius there are large changes in the reflectivity signal. This is a result of the amount of surface footprint presented to the incident X-ray beam.

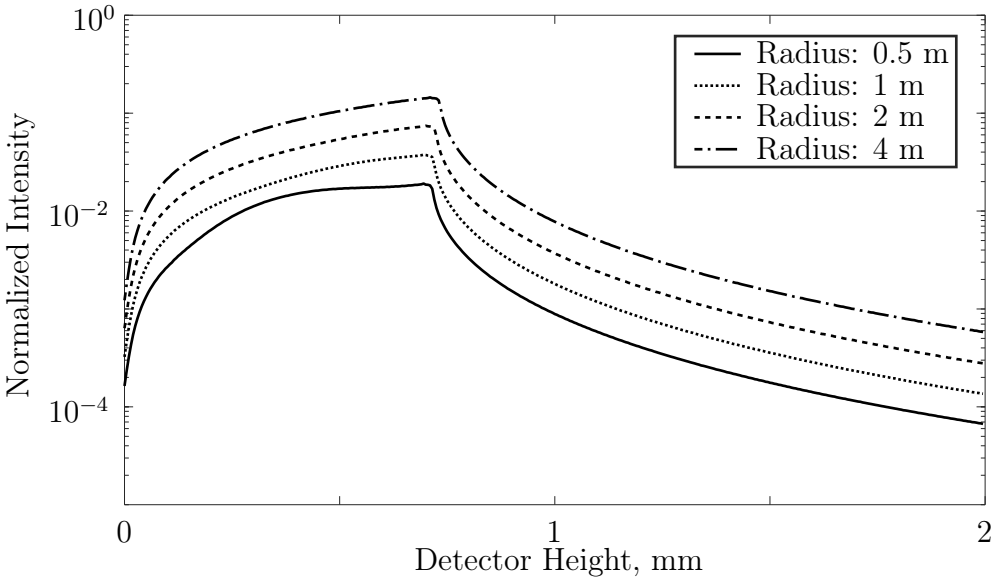

Figure 4.23: The effect of changing external radius is presented. Higher curvature leads to a reduction in reflectivity.

Finally, X-ray wavelength will contribute to the interaction between the X-rays and certain features of similar spatial frequency. Figure 4.24 details the effect that energy has on the reflectivity of a curved part. It can be seen that energy has minor impact on the reflectivity of a surface having evenly distributed surface roughness; however, it is yet to be determined if varying X-ray energy will improve measurement of surfaces having heterogeneous spatial spectral content.

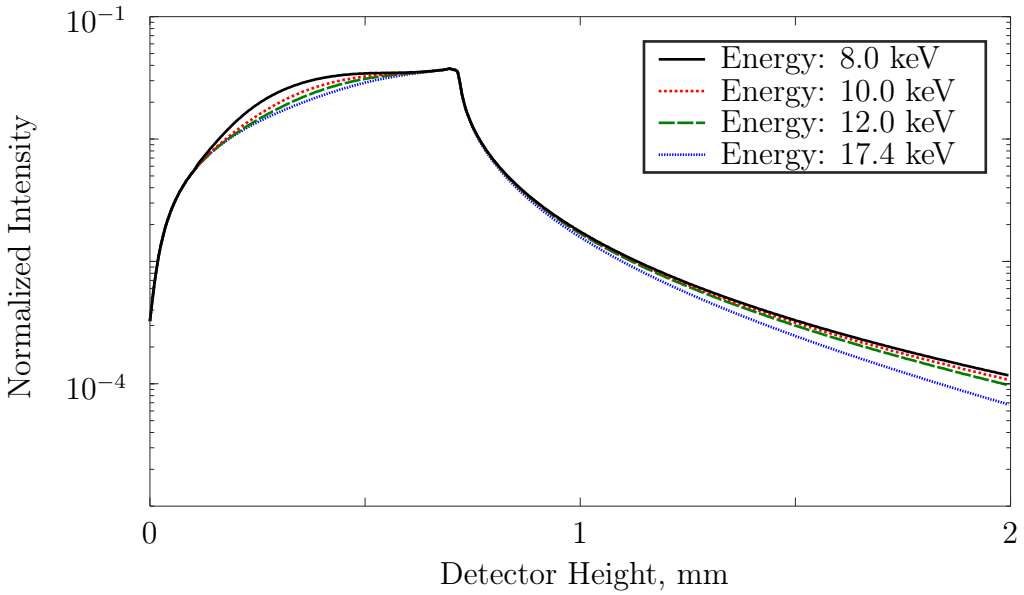

Figure 4.24: The reflectivity of a part having 1 m radius and 1 nm RMS surface roughness for several common X-ray energies: 8 keV (Cu Kα_1), 10 keV, 12 keV, and 17.4 keV (Mo Kα_1).

4.3.3 Internal Surface Reflections

Finally, the field at the detector for X-rays that scatter an internal surface can be found. Figure 4.25 shows the fields that must be solved for to define the final field at the detector $\mathbf{E}_5$. For X-rays that transmit through the part and will be incident

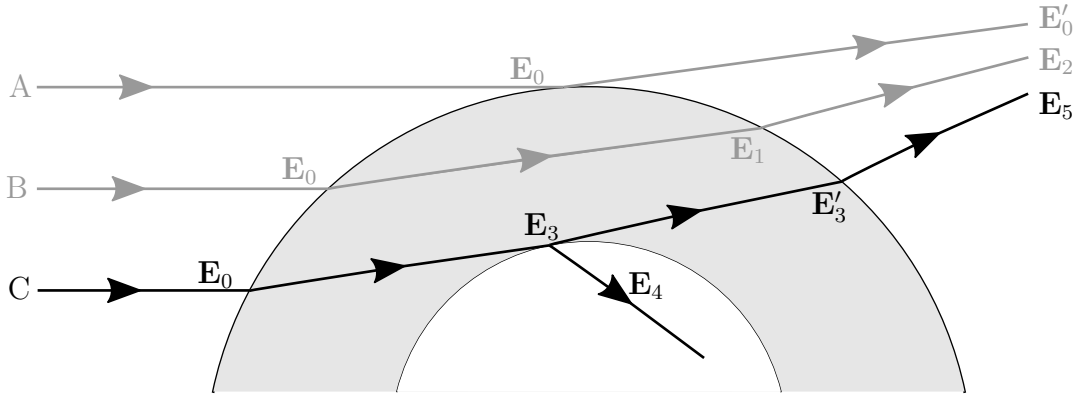

Figure 4.25: Emphasized view of case C, tracing the path of the internally reflected X-rays.

upon an inner surface, recall the condition for incidence from Equation 4.27, there will be a reflection from the inner surface. This interface, noted interface [34], is shown in Figure 4.26.

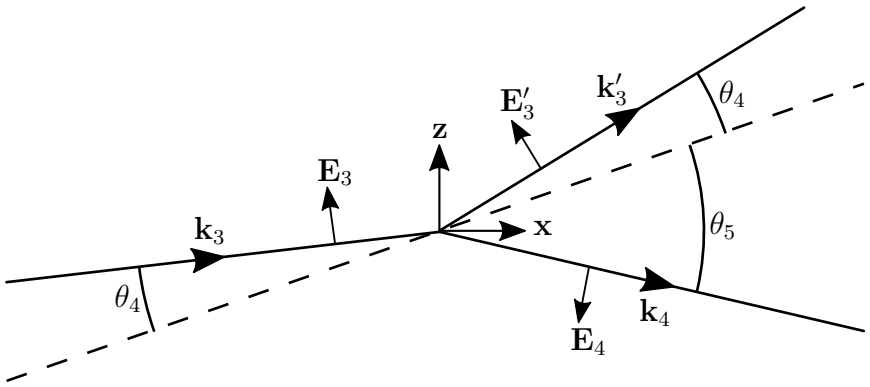

Figure 4.26: Definition of the field interactions at the inner surface interface.

The electric field of X-rays incident upon the inner surface is given by

$$\mathbf{E}_3 = {}^{01}\mathbf{\Phi}\mathbf{E}_0 \exp\left(i\,\mathbf{k_3}\cdot\mathbf{r}_3\right)\exp\left(-\mu r_3/2\right), \tag{4.84}$$

where

$$\mathbf{k}_3 = \mathbf{k}_1. \tag{4.85}$$

The amplitudes of the reflected and refracted X-rays at this interface are given by the Fresnel coefficients

$$\begin{bmatrix} \mathbf{A}'_3 \\ \mathbf{A}_4 \end{bmatrix} = \begin{bmatrix} {}^{34}\boldsymbol{\Psi} & {}^{43}\boldsymbol{\Phi} \\ {}^{43}\boldsymbol{\Phi} & {}^{34}\boldsymbol{\Psi} \end{bmatrix} \begin{bmatrix} \mathbf{A}_3 \\ \mathbf{A}'_4 \end{bmatrix}. \tag{4.86}$$

The Fresnel coefficient of reflection for X-rays incident upon the inner surface is

$${}^{34}\boldsymbol{\Psi} = \begin{bmatrix} {}^{34}\Psi_{(x)} & 0 & 0 \\ 0 & {}^{34}\Psi_{(y)} & 0 \\ 0 & 0 & {}^{34}\Psi_{(z)} \end{bmatrix}, \tag{4.87}$$

where,

$${}^{34}\Psi_{(x)} = \frac{{}^{34}\mathrm{k}_{4(z)} \left(\mathbf{k}_3 \cdot \mathbf{k}_3\right) - {}^{34}\mathrm{k}_{3(z)} \left(\mathbf{k}_4 \cdot \mathbf{k}_4\right)}{{}^{34}\mathrm{k}_{3(z)} \left(\mathbf{k}_4 \cdot \mathbf{k}_4\right) + {}^{34}\mathrm{k}_{4(z)} \left(\mathbf{k}_3 \cdot \mathbf{k}_3\right)} = -{}^{34}\Psi_{(z)} \tag{4.88}$$

$${}^{34}\Psi_{(y)} = \frac{{}^{34}\mathrm{k}_{3(z)} - {}^{34}\mathrm{k}_{4(z)}}{{}^{34}\mathrm{k}_{3(z)} + {}^{34}\mathrm{k}_{4(z)}}. \tag{4.89}$$

The magnitude of the reflected wave-vector will be the same as the magnitude of the incident wave-vector:

$$\mathbf{k}_3 \cdot \mathbf{k}_3 = \mathbf{k}_1 \cdot \mathbf{k}_1 = \left(\frac{n_1}{n_0} k\right)^2, \tag{4.90}$$

and the magnitude of the refracted wave-vector is, from Equation 4.45,

$$\mathbf{k}_4 \cdot \mathbf{k}_4 = \left(\frac{n_2}{n_0} k\right)^2. \tag{4.91}$$

Additionally, from Figure 4.26, the wave-vectors with respect to the ^{34} interface are

$$ {}^{34}\mathbf{k}_3 = \frac{n_1}{n_0} k \begin{bmatrix} \cos\theta_4 \\ 0 \\ -\sin\theta_4 \end{bmatrix}, \tag{4.92} $$

$$ {}^{34}\mathbf{k}_4 = \frac{n_2}{n_0} k \begin{bmatrix} \cos\theta_5 \\ 0 \\ -\sin\theta_5 \end{bmatrix}. \tag{4.93} $$

The Fresnel coefficients can then be simplified to:

$$ {}^{34}\Psi_{(x)} = \frac{n_1 \sin\theta_5 - n_2 \sin\theta_4}{n_1 \sin\theta_4 + n_2 \sin\theta_5} = -{}^{34}\Psi_{(z)}, \tag{4.94} $$

$$ {}^{34}\Psi_{(y)} = \frac{n_1 \sin\theta_4 - n_2 \sin\theta_5}{n_1 \sin\theta_4 + n_2 \sin\theta_5}. \tag{4.95} $$

The reflected field from the inner surface $\mathbf{E}'_3$ will be diffused by the surface roughness and will be attenuated by the part material along the exit path. As before, the attenuation factor for the part material is $\mu = k\beta_1$, and the inner surface roughness is σ_2. Therefore, the reflected field incident upon the outer radius of the part is

$$ \mathbf{E}'_3 = {}^{34}\boldsymbol{\Psi}\mathbf{E}_3 \exp(i\,\mathbf{k}'_3 \cdot \mathbf{r}'_3) \exp(-\mu r'_3/2)\sqrt{f(\sigma_2)}. \tag{4.96} $$

Figure 4.27 shows interface $^{3'5}$ where the reflected X-rays from the inner surface are incident upon the outer surface.

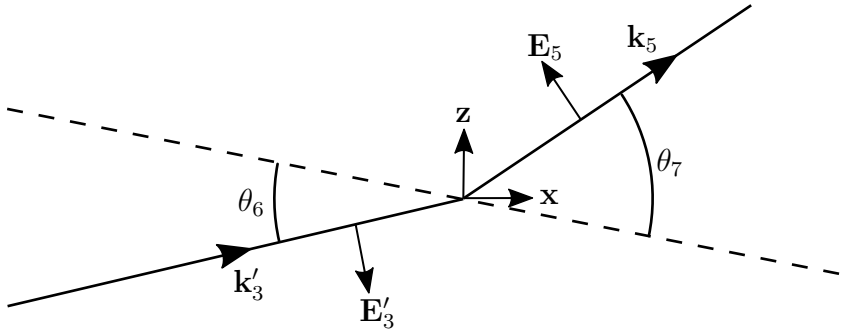

Figure 4.27: Definition of the field interactions at the outer surface interface.

To determine the field at the detector, $\mathbf{E}_5$, the Fresnel coefficients of refraction for this interface must be derived:

$$ {}^{3'5}\mathbf{\Phi} = \begin{bmatrix} {}^{3'5}\Phi_{(x)} & 0 & 0 \\ 0 & {}^{3'5}\Phi_{(y)} & 0 \\ 0 & 0 & {}^{3'5}\Phi_{(z)} \end{bmatrix}, \tag{4.97} $$

where,

$$ {}^{3'5}\Phi_{(x)} = 2\,\frac{{}^{3'5}\mathrm{k}_{5(z)}\,(\mathbf{k}'_3\cdot\mathbf{k}'_3)}{{}^{3'5}\mathrm{k}'_{3(z)}\,(\mathbf{k}_5\cdot\mathbf{k}_5)+{}^{3'5}\mathrm{k}_{5(z)}\,(\mathbf{k}'_3\cdot\mathbf{k}'_3)}, \tag{4.98} $$

$$ {}^{3'5}\Phi_{(y)} = 2\,\frac{{}^{3'5}\mathrm{k}'_{3(z)}}{{}^{3'5}\mathrm{k}'_{3(z)}+{}^{3'5}\mathrm{k}_{5(z)}}, \tag{4.99} $$

$$ {}^{3'5}\Phi_{(z)} = 2\,\frac{{}^{3'5}\mathrm{k}'_{3(z)}\,(\mathbf{k}'_3\cdot\mathbf{k}'_3)}{{}^{3'5}\mathrm{k}'_{3(z)}\,(\mathbf{k}_5\cdot\mathbf{k}_5)+{}^{3'5}\mathrm{k}_{5(z)}\,(\mathbf{k}'_3\cdot\mathbf{k}'_3)}. \tag{4.100} $$

From Equation 4.45,

$$ \mathbf{k}'_3\cdot\mathbf{k}'_3 = {n_1}^2\frac{\mathbf{k}_0\cdot\mathbf{k}_0}{{n_0}^2} = \left(\frac{n_1}{n_0}k\right)^2, \tag{4.101} $$

$$ \mathbf{k}_5\cdot\mathbf{k}_5 = {n_0}^2\frac{\mathbf{k}_0\cdot\mathbf{k}_0}{{n_0}^2} = k^2, \tag{4.102} $$

and, from Figure 4.27, the wave-vectors with respect to the ${}^{3'5}$ interface are

$$ {}^{3'5}\mathbf{k}'_3 = \frac{n_1}{n_0} k \begin{bmatrix} \cos\theta_6 \\ 0 \\ \sin\theta_6 \end{bmatrix}, \tag{4.103} $$

$$ {}^{3'5}\mathbf{k}_5 = k \begin{bmatrix} \cos\theta_7 \\ 0 \\ \sin\theta_7 \end{bmatrix}. \tag{4.104} $$

Recalling Equation 4.37, $\theta_{out,C} = \theta_0 - \theta_1 + 2\theta_4 + \theta_7 - \theta_6$, the exiting wave-vector is

$$ \mathbf{k}_5 = k \begin{bmatrix} \cos\theta_{out,C} \\ 0 \\ \sin\theta_{out,C} \end{bmatrix}; \tag{4.105} $$

therefore, the Fresnel coefficients for refraction can be rewritten

$$ {}^{3'5}\Phi_{(x)} = \frac{2n_1 \sin\theta_7}{n_0 \sin\theta_6 + n_1 \sin\theta_7}, \tag{4.106} $$

$$ {}^{3'5}\Phi_{(y)} = \frac{2n_1 \sin\theta_6}{n_1 \sin\theta_6 + n_0 \sin\theta_7}, \tag{4.107} $$

$$ {}^{3'5}\Phi_{(z)} = \frac{2(n_1/n_0)^2 \sin\theta_6}{\sin\theta_6 + (n_1/n_0)\sin\theta_7}. \tag{4.108} $$

Finally, having defined all of the components of the field at the detector of X-rays reflecting from an inner surface,

$$ \mathbf{E}_5 = {}^{3'5}\mathbf{\Phi}\mathbf{E}'_3 \exp\left(i\,\mathbf{k}_5 \cdot \mathbf{r}_5\right), \tag{4.109} $$

and the intensity of this component is given by

$$ \mathrm{I}_5 = \mathbf{E}_5 \cdot \mathbf{E}_5. \tag{4.110} $$

Naturally, the distance between the inner and outer radii will have an effect on the intensity of the reflections from the inner surface. At small shell thickness, approaching zero thickness, there will be little-to-no transmitted X-rays and, thus, no X-rays reflected from the inner surface. As the shell thickness increases, more X-rays will transmit through the outer surface and reflect from the inner surface; however, the path lengths for internal reflections will become large and approach the extinction length of the material. This gradual increase, then decrease in reflectivity can be seen in Figure 4.28 where the total intensity is affected by the internal reflections.

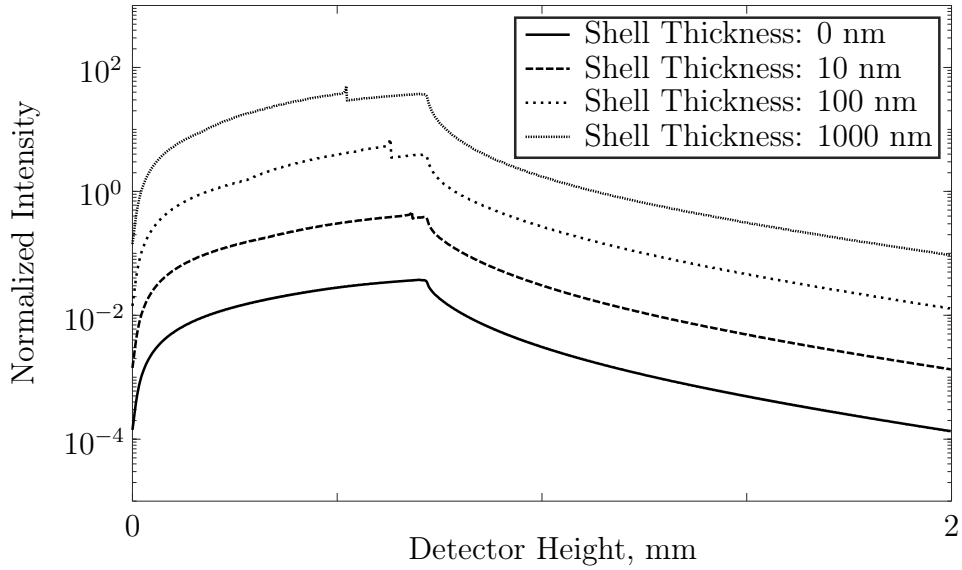

Figure 4.28: Comparison of the effect of shell thickness ($R_{outer} - R_{inner}$) for a 1.5 m outer radius Silicon sample. Curves are offset one order of magnitude for clarity. The intensity of reflections from the inner surface increases as the shell thickness increases until the path lengths for reflections get too large.

As shown in Figure 4.29, the internal surface roughness affects the total intensity by exponentially reducing the reflectivity of the inner surface. Radiograph measurements of shells can be fit to these curves to determine the internal surface roughness.

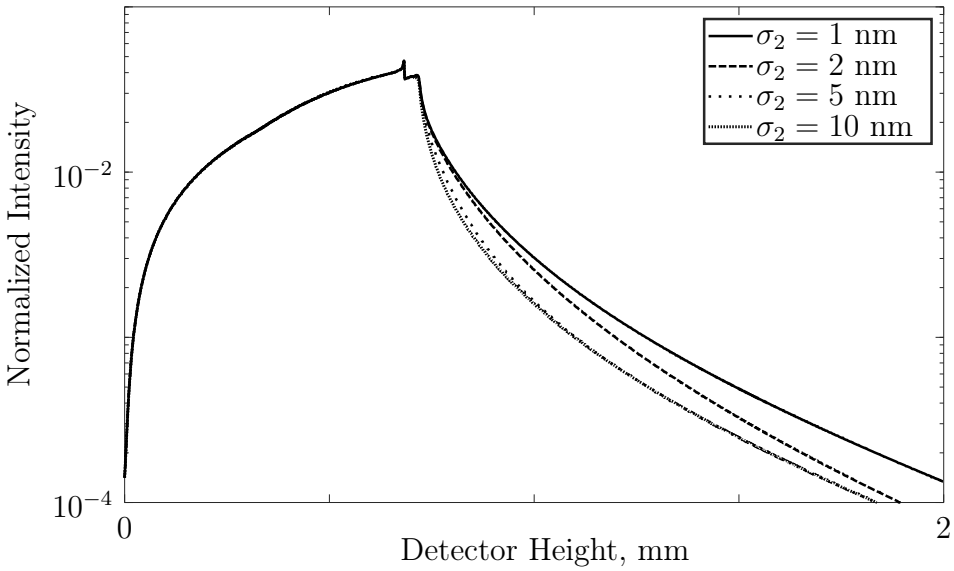

Figure 4.29: Comparison of the implication of various internal surface roughness for a 1.5 m radius Silicon sample having outer roughness $\sigma_1 = 1$ nm.

4.4 Experiments

To verify the model presented in the previous section, experiments are conducted in a purpose built X-ray facility at The University of North Carolina at Charlotte. An overview photograph of the system is shown in Figure 4.30. The experiments are performed on polished Silicon wafers, some of which are coated, that are bent to various curvature to test the robustness of the model.

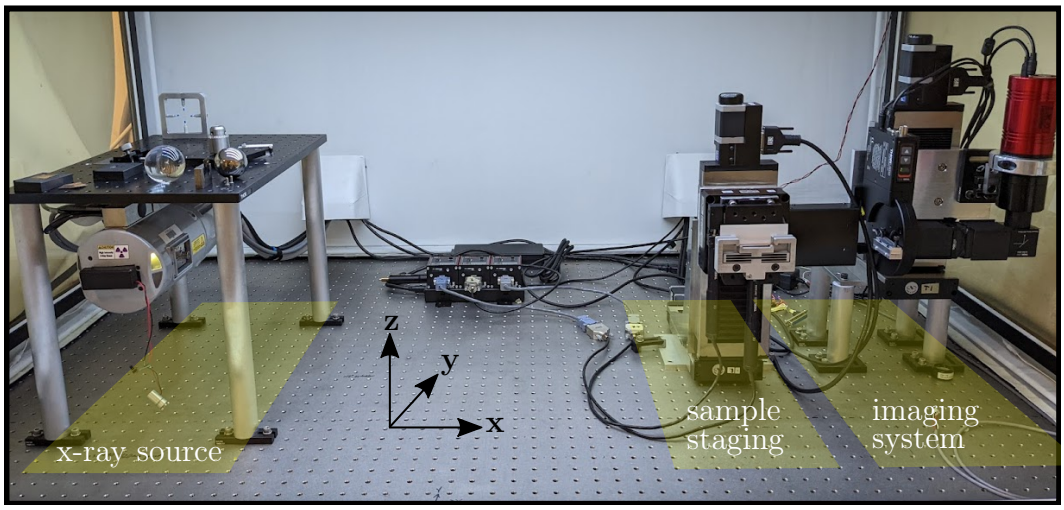

Figure 4.30: Overview of the X-ray facility at The University of North Carolina at Charlotte configured for XRR measurements. From left-to-right is the X-ray source, sample staging with y, z, and θ control, and the imaging system with a scintillator and multipixel CCD camera on y and z stages.

4.4.1 Microsource X-Ray System

The X-ray source is a 25 W microsource (Bede Scientific) with a Molybdenum target having peak output emission along the Kα_1 line (17.4 keV). A polycapillary optic collimates the output beam into a 2 mm diameter, Gaussian beam. A visible light laser aligner on a tip-tilt flexure can be attached to the polycapillary optic housing and aligned to the X-ray beam for easier alignment of optics and samples.

4.4.2 Specimen Handling

All samples are mounted in a flexure guided bending fixture, detailed in Section 4.4.4, that is mounted on a series of alignment and positioning stages. The stages are shown in Figure 4.31.

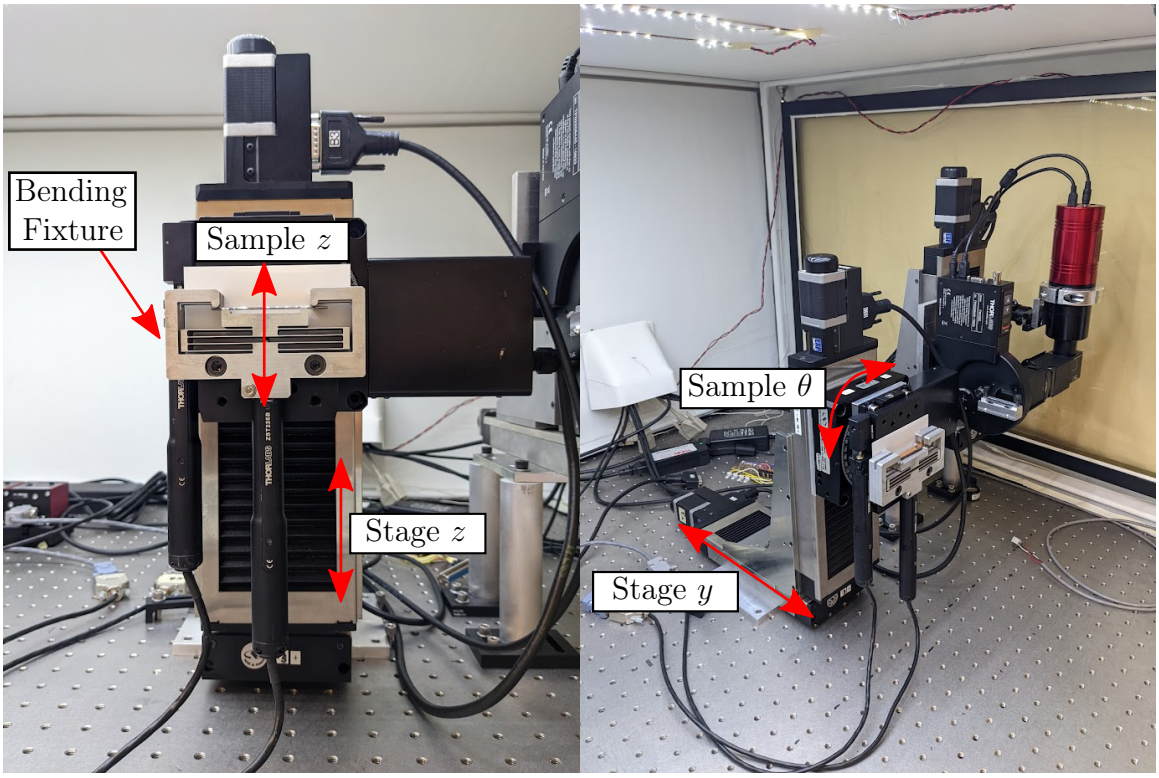

Figure 4.31: A photograph of the sample staging in the X-ray system. Stage y and Stage z are used to position the sample in the X-ray beam. Sample θ is used to align the sample parallel to the beam and Sample z (behind the bending fixture) is used to position the sample in the center of rotation.

Two 150 mm range linear stepper motor translation stages (Newport UTS150PP), "Stage y" and "Stage z" in Figure 4.31, are used to position the sample in the center of the beam in the y and z directions. The "Sample θ" stage (Newport URS100BPP) is a stepper motor rotation stage with 0.017 mrad resolution that is used to align the sample parallel to the beam. The "Sample z" stage is a 25 mm range stepper motorised actuator (Thorlabs ZST225B) on a linear translation stage (Thorlabs XR25P/M) used to align the sample face to the center of rotation of the "Sample θ"

stage. An additional 150 mm linear translation stage can be added to the sample system to provide translation in the x direction to adjust the object-detector-distance and is not shown in the figure. The Newport translation and rotation stages are controlled with two 3-axis motion controllers (Newport ESP301) and the Thorlabs actuators are controlled with Kinesis K-Cube stepper motor controllers (Thorlabs KST101).

4.4.3 X-Ray Imaging System

The imaging system is shown in Figure 4.32. A filter wheel (Thorlabs FW120C) holds several scintillators, a lead shield, and a USAF test target for camera calibration. Each scintillator is fit with a carbon fiber window preceding the crystal to block visible light from leaking into the imaging system.

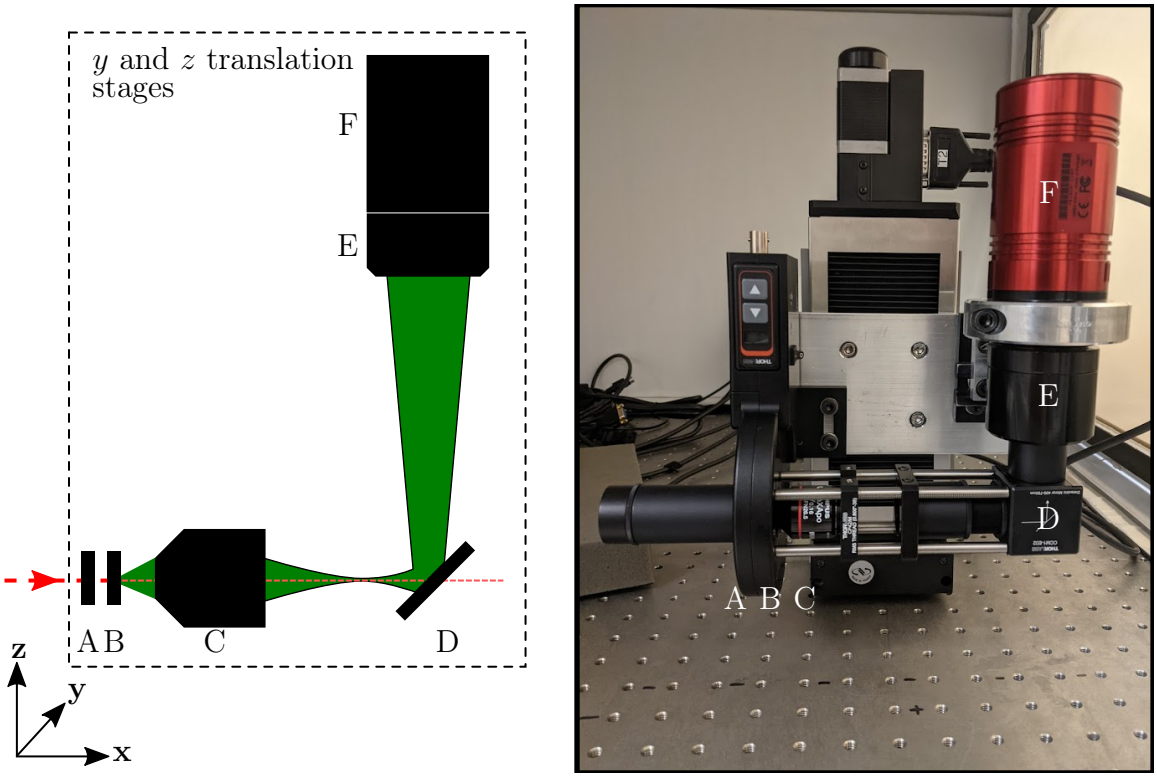

Figure 4.32: Diagram (left) and photograph (right) of the imaging system. Components: (A) carbon fiber window to block visible light, (B) filter wheel for changing various LuAG and LuAg:Ce scintillators, (C) 4X infinity corrected objective lens, (D) dielectric-coated turning mirror, (E) wide field lens, and (F) multipixel CCD camera.

For all measurements a custom 50 μm thick LuAG:Ce scintillator (CRYTUR) is used with a 100 nm Aluminum coating on the X-ray side of the crystal. The Aluminum coating allows the X-rays to pass through to the scintillator but will reflect any emission that scatters away from the objective lens thereby increasing the signal. The wavelength of maximum emission for the LuAG:Ce scintillator is 535 nm. A 4X infinity corrected objective lens (Olympus UPLXAPO) is focused on the scintillator and collects the emission. The image is turned to the camera with a dielectric-coated turning prism mirror (Thorlabs CCM1-E02) with >99 % reflectance between 400 and 750 nm. The purpose of this mirror is to separate any radiation that might have passed through the scintillator from the visible emission. This also protects the camera from any high energy radiation. The image is collected with a wide field tube lens (Olympus SWTLU-C) and is projected onto the multipixel CCD camera. The camera is an Atik 428EX monochromatic CCD camera with 4.54 μm pixels, a resolution of 1932×1452 pixels, and a 16-bit ADC.

4.4.4 A Fixture for Constant Curvature Bending of Silicon Wafers

A flexure-based fixture was designed and manufactured to ensure that Silicon wafer samples are bent at a constant radius. The principle of four point bending is used to ensure that the sample is under a constant bending moment between the loading pins. Figure 4.33 is a CAD drawing of the fixture. A symmetric double compound rectilinear flexure design was chosen to constrain the motion of the lower jaw to the z-direction. Figure 4.33(B) shows the channel cut into the upper, fixed jaw of the fixture which allows reflected X-rays to pass unobstructed. A micrometer or actuator can be fixed in the bottom of the fixture for precise adjustment of the bottom jaw displacement.

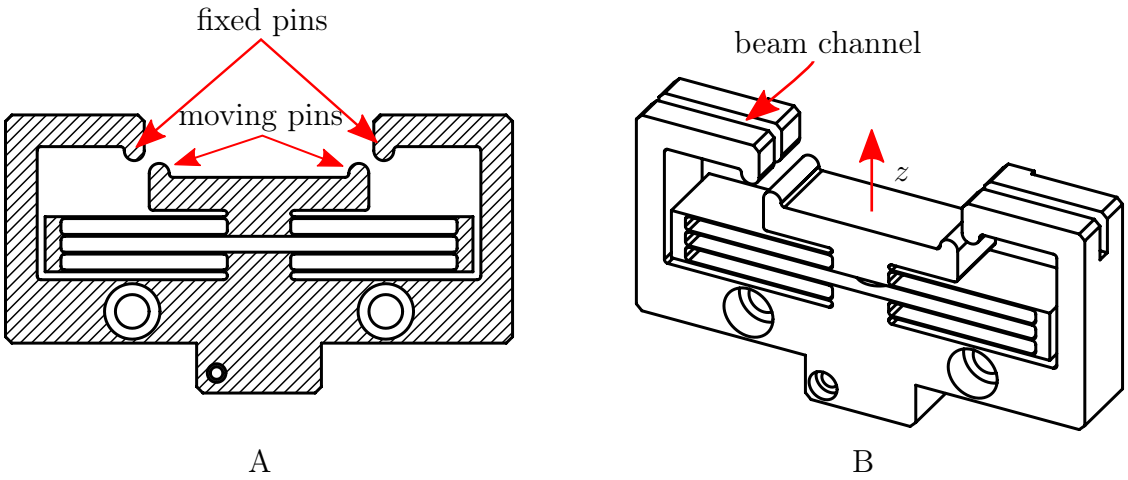

Figure 4.33: Drawing of the flexure based four point wafer bending fixture. View A is the front view of the fixture where the symmetric double-compound rectilinear flexure can be seen. View B is the trimetric view where the channel through the upper jaws can be seen which allows the reflected X-rays to pass.

To determine the relationship between the beam radius and the actuator displacement, Figure 4.34 shows the geometry of the system.

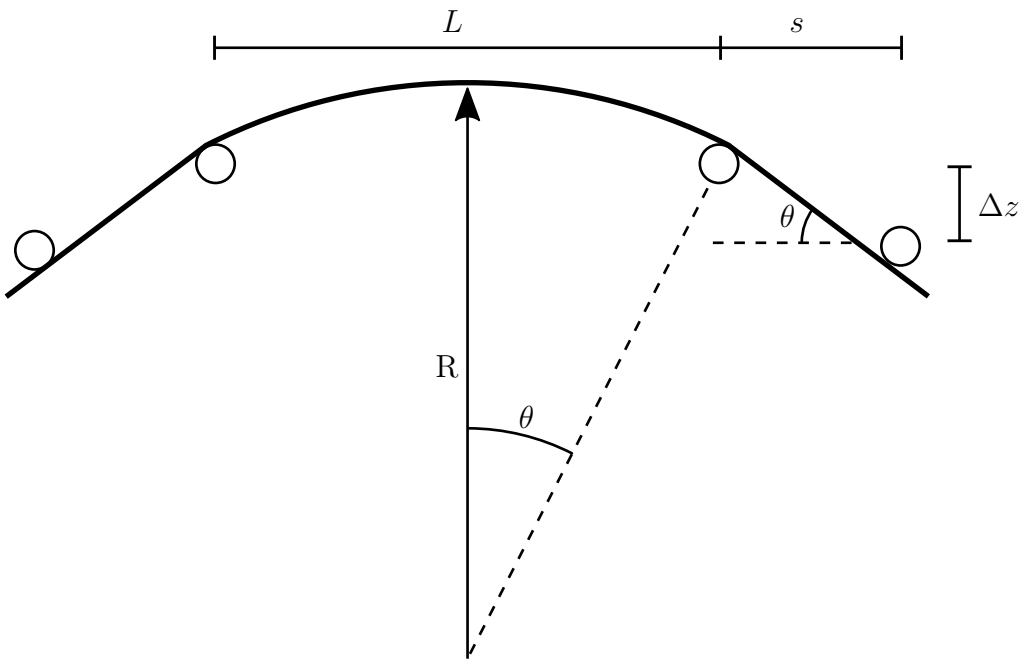

Figure 4.34: Geometric representation of four point beam bending. Adjustment of the distance between the pins, s and L, allows for the change in relationship between the deflection Δz and the beam radius R.

It can be easily seen that

$$\tan\theta = \frac{\Delta z}{s}, \tag{4.111}$$

and the radius,

$$\mathrm{R} = \frac{L}{2\sin\theta}. \tag{4.112}$$

Recognizing that $\sin(\arctan x) = x/\sqrt{x^2+1}$,

$$\mathrm{R} = \frac{Ls}{2\Delta z}\sqrt{\left(\frac{\Delta y}{s}\right)^2 + 1}. \tag{4.113}$$

To determine the pin spacing, the fracture condition for the Silicon samples can be considered. For a beam under bending, recall that

$$\frac{2\sigma}{t} = \frac{E}{\mathrm{R}}, \tag{4.114}$$

where σ is the strength, t is the beam thickness, E is Young's modulus, and R is the bending radius. Therefore, the maximum radius before the wafer breaks is

$$\mathrm{R}_{max} = \frac{Et}{2\sigma_{max}}. \tag{4.115}$$

Relating this condition to Equation 4.113 for small Δz,

$$\mathrm{R}_{max} = \frac{Et}{2\sigma_{max}} \approx \frac{Ls}{2\Delta z}. \tag{4.116}$$

The 1 mm thick Silicon wafers used were diced into 50 mm strips. For constant bending across the entire sample, the ideal distance between the outer jaws ($L + 2s$) would be 50 mm. For this reason, the fixture was designed with $L = 40$ mm and $s = 5$ mm. With these parameters and the material parameters of Silicon, see Chetwynd

and Smith 1990 [69], the maximum displacement before fracture can be determined

$$\Delta z_{max} = \frac{Ls\sigma_{max}}{Et} = \frac{(0.040\text{ m})(0.005\text{ m})(170\times10^6\text{ Pa})}{(140\times10^9\text{ Pa})(0.001\text{ m})} = 210\,\mu\text{m}. \tag{4.117}$$

A photograph of the fixture with a sample loaded is shown in Figure 4.35.

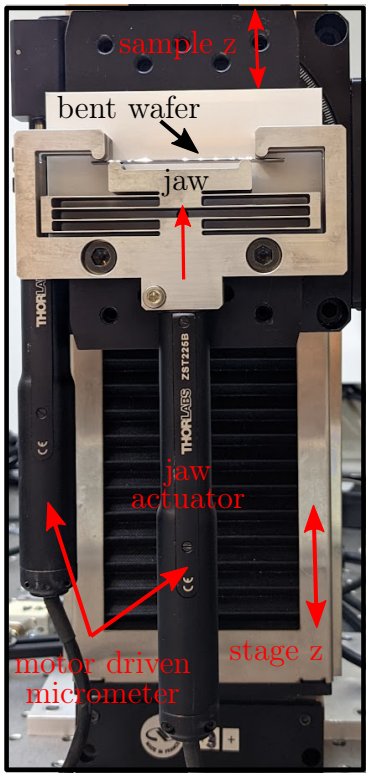

Figure 4.35: Photograph of the wafer bending fixture with motorized stepper actuator.

4.4.5 Silicon Wafer Samples

Experiments were conducted to measure the surface roughness of Silicon wafers as they were bent to various radii with the wafer bending fixture in the previous subsection. Measurements of three samples are presented: a 380 µm thick polished Silicon wafer, a 2 mm thick Chromium coated Silicon wafer, and a 2 mm thick Copper coated Silicon wafer.

Each sample was measured with an atomic force microscope (Nanoscope Dimension 3100) to determine the surface roughness. Measurements were taken over a $5 \times 5\,\mu m$ area. The results from these measurements are presented in Table 4.2.

Table 4.2: Roughness results from AFM measurements of Silicon wafer samples.

Sample	RMS Roughness (nm)
Uncoated Silicon Wafer	0.9
Chromium Coated Silicon Wafer	1.9
Copper Coated Silicon Wafer	6.5

4.4.6 XRR Measurement Setup

XRR measurements were performed on all samples with 60 second exposures. Samples were bent such that the full beam footprint was incident upon the surface. The X-ray source is a collimated microsource (Bede Scientific) with Molybdenum target producing X-rays at 17.4 keV. The beam control is set at 50 kV and 0.50 mA for a total of 25 W. After collimation, the beam diameter is 2 mm and is approximately Gaussian. For more details on the X-ray facility, see [70]. The object to detector distance is 200 mm. Table 4.3 lists the bending deflection and radius for each sample.

Table 4.3: Measurement parameters for the bent wafer samples.

Sample	Deflection, Δz (μm)	Radius (m)
Uncoated Silicon Wafer	40	2.5
Chromium Coated Wafer	67	1.5
Copper Coated Wafer	50	2.0

4.5 Results and Conclusions

Images (I) are corrected for the incident beam and detector with the collection of Flat and Dark images. Flat (F) images are taken of the X-ray beam without the presence of the sample. Dark (D) images are taken of the detector without the presence of the X-ray beam. The corrected images (C) are then determined by

$$C = \frac{I - D}{F - D}. \tag{4.118}$$

When an image is collected, the signal is discretized into bins (pixels) on the detector. This discretization must be modelled to properly fit the experimental data. To do this, the computed heights of the reflections and transmissions on the detector are sorted into bins according to the detector pixels. To include phase information, the field of each ray arriving at overlapping bins are summed and then squared to compute the resulting intensity for each bin (pixel).

Figure 4.36 shows the measurement results from the uncoated Silicon wafer after cleaning using hydroflouric acid (HF) to remove oxide layer and contaminants. Prior to etching, this sample produced no measurable reflections. Computed curves from the model for various RMS surface roughness are superimposed to determine the best fit between the measurement and the model. It can be readily seen that all fits overestimate the image intensity as the incident angle approaches the critical angle for the material. The computed curve for 2 nm RMS surface roughness appears to fit the decay rate of the data the best.

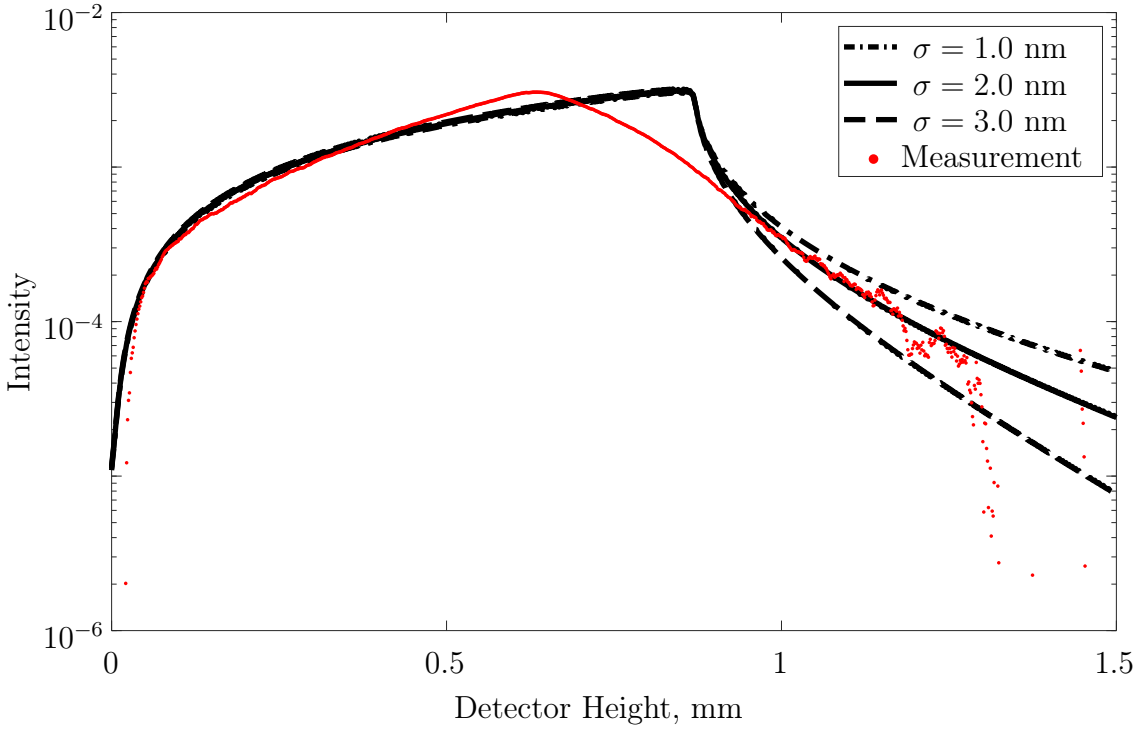

Figure 4.36: Measurement result for an uncoated Silicon wafer bent to 2.5 m radius with computed fits for several RMS surface roughness values. The fit for 2 nm RMS surface roughness appears to match the image intensity best.

The measurement of the Chromium coated wafer, bent to 1.5 m radius, is shown in Figure 4.37. The best fit between the measurement and model-generated curves can be seen to be 3 nm RMS.

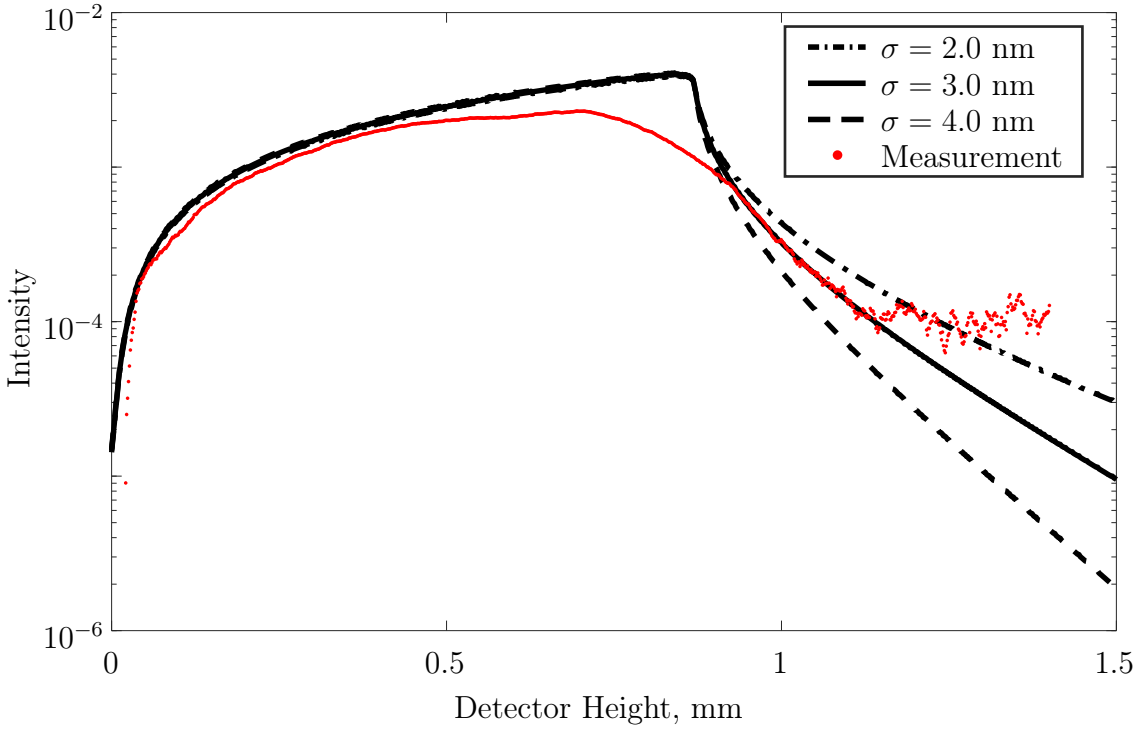

Figure 4.37: Measurement result for a Chromium Coated Silicon wafer bent to 1.5 m radius with computed fits for several RMS surface roughness values. The fit for 3 nm RMS surface roughness appears to match the image intensity best.

A third sample measurement of a Copper coated wafer is shown in Figure 4.38. The best fit between the data and the computed curves is 5 nm RMS.

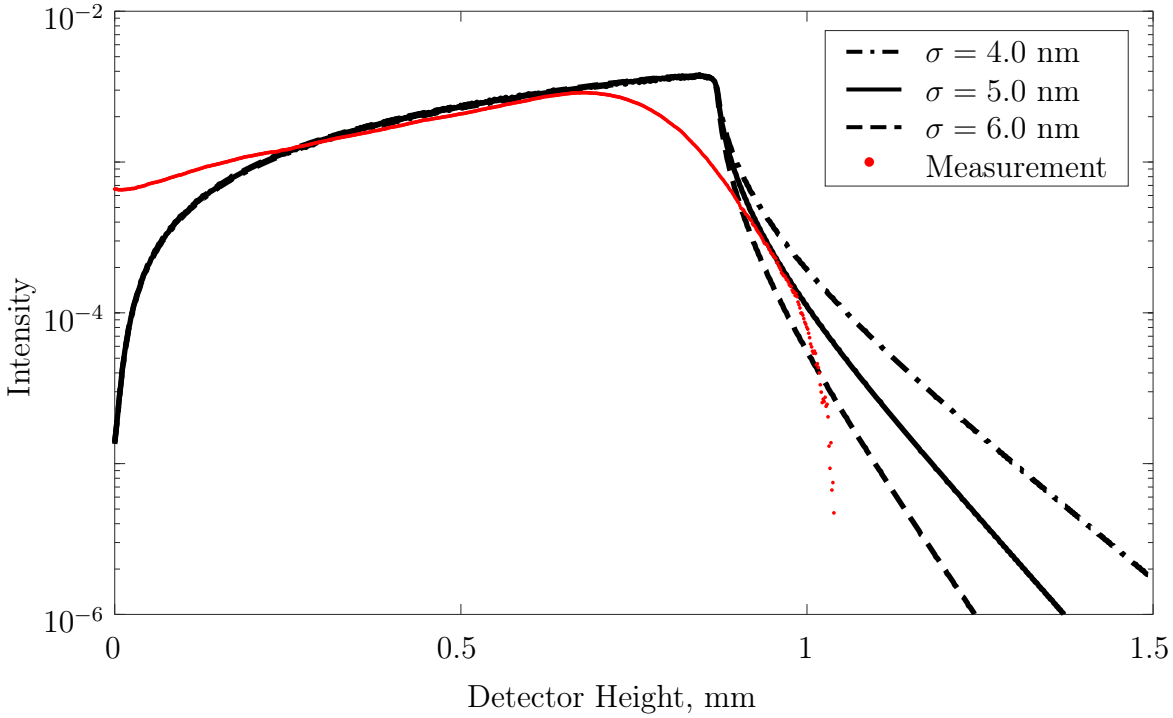

Figure 4.38: Measurement result for a Copper Coated Silicon wafer bent to 2.0 m radius with computed fits for several RMS surface roughness values. The fit for 5 nm RMS surface roughness appears to match the image intensity best.

At present, the "plateau" and rounded appearance of the data around the critical angle in the image is repeatable but not well understood. This is a significant issue as the break point in the intensity and the decay immediately following hold the most valuable surface roughness information and heavily influence the model fitting. An additional area of interest could be effects on the surface of the Silicon wafer due to the strain during bending. This strain could affect the crystal structure at the surface and possibly change the refractive index of the material. Effects of surface reconstruction on the refractive index is not well studied at this time. This effect is expected to be minimal in metals and is not reported in literature; however, there are many studies using XRR to determine the effect of surface contamination and oxide growth/modification under different environmental conditions. In these measurements, the surfaces are clean and mostly free of oxide and stored in a temperature and humidity controlled environment typical of a science laboratory setting. Therefore surface conditions are not expected to change significantly in these measurements. Strain due to bending the wafer will induce Poisson's ratio dependant density change that may also influence specular scatter where density gradients have a direct effect on specular reflection intensity. This effect is expected to be minimal as the strains on the wafer are relatively low (approximately 0.25 millistrain) for maximum bending of the Silicon specimen.

These measurements are obtained using the Bede microsource using a Molybdenum Kα target. This source is not optimized for minimum blur and beam divergence. Additionally, energy contributions from the Kβ line of the source, which is not filtered, are not considered in the models. The use of advanced X-ray sources such as emerging fourth generation synchrotrons will mitigate these source effects.

For the significantly rougher Copper coated specimen, a known issue in literature is the breakdown of common approximation based roughness models, such as the one used here, at high surface roughness. The Copper coated wafer is near the

upper bound of the capability of these models and could explain the departure of the simulated curve from the data at the higher angles.

Table 4.4 summarizes the XRR measurement results and the AFM measurement results for comparison.

Table 4.4: Summary of the XRR RMS roughness measurement results in comparison to the AFM RMS roughness measurement results. The XRR measurement results are higher than the AFM for "smooth" surfaces, but has high departure from the AFM result for the "rough" surface.

Sample	XRR	AFM
Uncoated Silicon Wafer	2 nm	0.9 nm
Chromium Coated Wafer	3 nm	1.9 nm
Copper Coated Wafer	5 nm	6.5 nm

From the XRR and AFM measurement results, it can be speculated that the significantly higher measurement area of XRR could contribute to the higher roughness result. The AFM measurement is of a 5 μm × 5 μm area; whereas, the XRR measurement area is approximately 2 mm × 30 mm. High amplitude surface asperities not included in the AFM measurement would contribute to a reduction in surface reflectivity and a higher roughness result with XRR.

The desired outcome of this work is the measurement of surface roughness of small spheres. For this reason, measurements were attempted on polished spheres of various radii from 2 mm to 5 mm and various materials including steels and ceramics. Measurements on these spheres were attempted using the facilities at The University of North Carolina at Charlotte, The Advanced Light Source (ALS) at Lawrence Berkeley National Laboratory, and The Advanced Photon Source (APS) at Argonne National Laboratory. Experiments at the ALS tomography beamline yielded no measurable reflections from the samples as the radius was too small for adequate reflective surface area. Even with synchrotron radiation intensity the signal to noise was too low to separate reflections from background.

Measurements at the APS grazing incidence small-angle X-ray scattering (GISAXS) beamline did result in measurable scatter from a 5 mm Tungsten Carbide ball, see Figure 4.39.

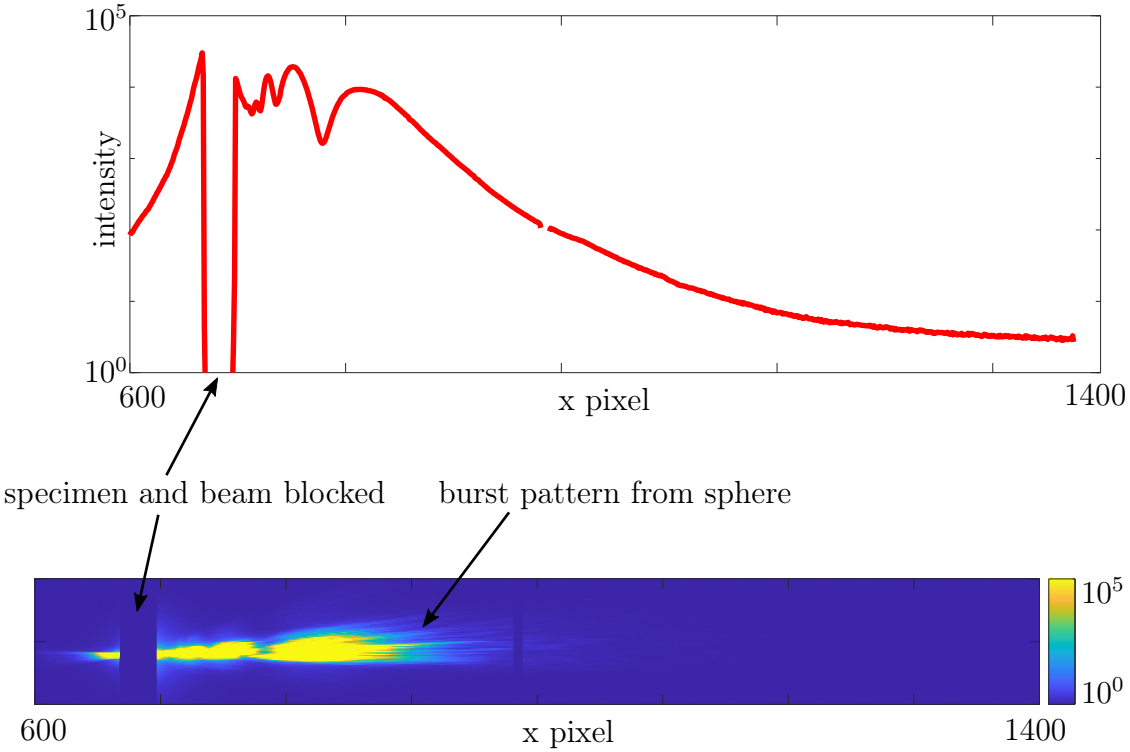

Figure 4.39: Measurement data from APS beamline 12-ID-B. (top) line-out from sector analysis on sphere burst pattern. The gap on the left side corresponds to the beamstop blocking the direct beam and specimen to protect the high sensitivity detector. Intensity oscillations to the right of the beamstop could be near-surface oscillations from reflection-transmission interference. (bottom) image of the sphere measurement. The burst pattern created from reflections off of the sphere can be seen on either side of the sphere resulting in a cone of reflections from the surface.

This measurement was complicated by the need to block the main X-ray beam. The GISAXS beamline consists of a high intensity beam and a sensitive CCD and direct measurement of the beam was not possible. This did not allow for near-surface scatter measurement making it difficult to determine where the sample surface was located in the image. The surface location and the distance of the scattered light from the surface are required for proper analysis. These measurements did show that scatter can be seen from small spheres with very sensitive detectors. With

experimental refinements, this could be a viable path for the measurement of highly curved surfaces using synchrotron radiation.

An effect that can be explored with additional experimental setup is the effect of interference due to the asymmetric path lengths of the reflections and transmissions through the curved part. Potentially, these phase differences should cause fringes in the detector image but they were not observed in current experiments. Additional X-ray flux, source coherence, and detector dynamic range are expected to increase the possibility of observing this effect. The models developed here incorporate phase effects and can be used directly.

In experiments, it is noted that the sample must be aligned parallel to the beam prior to bending. If the sample is facing away from the beam (negative angle), small deflections will be occluded by the tilt of the sample. Furthermore, if the sample is tilted toward the beam (positive angle), the X-rays will reflect from the surface prior to bending the sample and effect the image normalization.

REFERENCES

[1] B. H. Kevles, *X-rays and beyond*. Rutgers University Press, 1997.

[2] J. A. Prins, "Über die Dispersion und Absorption von Röntgenstrahlen," *Zeitschrift für Physik*, vol. 47, no. 7-8, pp. 479–498, 1928.

[3] J. A. Cole, J. A. Cuadra, R. M. Panas, and S. T. Smith, "The effect of longer-range waviness on X-ray reflectivity measurements," *Journal of Synchrotron Radiation*, vol. 28, 2021.

[4] A. P. S. (APS), "APS News Nov2001," *APS News*, vol. 10, p. 8, 2001.

[5] W. C. Rontgen, "The X-Rays," *Annual Report of the board of regents of the smithsonian institution*, 1898.

[6] A. H. Compton, "Total Reflection of X-rays," *Phil. Mag.*, 1923.

[7] R. W. James, *The Optical Principles of the Diffraction of X-rays*. G Bell and Sons, 1 ed., 1948.

[8] V. H. Kiessig, "Untersuchungen zur Totalreflexion von Röntgenstrahlen," *Annalen der Physik*, vol. 402, no. 7, pp. 715–768, 1931.

[9] M. Yasaka, "X-ray thin film measurement techniques," *The Rigaku Journal*, vol. 26, no. 2, pp. 1–9, 2010.

[10] Y. Fujii, "Analysis of surface roughness correlation function by X-ray reflectivity," *Surface and Interface Analysis*, vol. 48, no. 11, pp. 1136–1138, 2016.

[11] L. G. Parratt, "Surface studies of solids by total reflection of x-rays," *Physical Review*, vol. 95, no. 2, pp. 359–369, 1954.

[12] Y. Yoneda, "Anomalous surface reflection of X rays," *Physical Review*, vol. 131, no. 5, pp. 2010–2013, 1963.

[13] P. Croce, L. Névot, and B. Pardo, "Contribution a l'étude des couches minces par réflexion spéculaire de rayons X," *Nouvelle Revue d'Optique Appliquée*, vol. 3, no. 1, pp. 37–50, 1972.

[14] P. Dutta and S. K. Sinha, "Analytic form for the static structure factor for a finite two-dimensional harmonic lattice," *Physical Review Letters*, vol. 47, no. 1, pp. 50–53, 1981.

[15] J. H. Underwood and T. W. Barbee, "Layered synthetic microstructures as Bragg diffractors for X rays and extreme ultraviolet: theory and predicted performance," *Applied Optics*, vol. 20, no. 17, p. 3027, 1981.

[16] G. H. Vineyard, "Grazing-incidence diffraction and the distorted-wave approximation for the study of surfaces," *Physical Review B*, vol. 26, no. 8, pp. 4146–4159, 1982.

[17] B. Vidal and P. Vincent, "Metallic multilayers for x rays using classical thin-film theory," *Applied Optics*, vol. 23, no. 11, p. 1794, 1984.

[18] S. K. Sinha, E. B. Sirota, S. Garoff, and H. B. Stanley, "X-ray and neutron scattering from rough surfaces," *Physical Review B*, vol. 38, no. 4, pp. 2297–2311, 1988.

[19] W. A. Hamilton and R. Pynn, "The effect of surface roughness on the phase of neutrons specularly reflected at grazing incidence," *Physica B*, vol. 173, pp. 71–73, 1991.

[20] B. Lengeler, "X-Ray Reflection, A New Tool for Investigating Layered Structures and Interfaces," *Advances in X-ray Analysis*, vol. 35, no. A, pp. 127–135, 1991.

[21] R. Chiarello, V. Panella, J. Krim, and C. Thompson, "X-ray reflectivity and adsorption isotherm study of fractal scaling in vapor-deposited films," *Physical Review Letters*, vol. 67, no. 24, pp. 3408–3411, 1991.

[22] R. Pynn, "Neutron scattering by rough surfaces at grazing incidence," *Physical Review B*, vol. 45, no. 2, pp. 602–612, 1992.

[23] F. Stanglmeier, B. Lengeler, W. Weber, H. Gobel, and M. Schuster, "Determination of the dispersive correction f'(E) to the atomic form factor from X-ray reflection," *Acta Crystallographica Section A: Foundations of Crystallography*, vol. 48, no. 4, pp. 626–639, 1992.

[24] W. W. Van Den Hoogenhof and D. K. De Boer, "Glancing-incidence X-ray analysis," *Spectrochimica Acta Part B: Atomic Spectroscopy*, vol. 48, no. 2, pp. 277–284, 1993.

[25] B. Lengeler and M. Hüppauff, "Surface analysis by means of reflection, fluorescence and diffuse scattering of hard X-ray," *Fresenius' Journal of Analytical Chemistry*, vol. 346, no. 1-3, pp. 155–161, 1993.

[26] D. Bahr, W. Press, R. Jebasinski, and S. Mantl, "X-ray reflectivity and diffuse-scattering study of CoSi2 layers in Si produced by ion-beam synthesis," *Physical Review B*, vol. 47, no. 8, pp. 4385–4393, 1993.

[27] D. K. Bowen and B. K. Tanner, "Characterization of engineering surfaces by grazing-incidence X-ray reflectivity," *Nanotechnology*, vol. 4, no. 4, pp. 175–182, 1993.

[28] D. K. de Boer, "Influence of the roughness profile on the specular reflectivity of x rays and neutrons," *Physical Review B*, vol. 49, no. 9, pp. 5817–5820, 1994.

[29] W. W. v.d. Hoogenhof and D. K. de Boer, "Glancing incidence X-ray analysis: Forgotten or to be discovered?," 1994.

[30] D. K. de Boer, "X-ray reflection and transmission by rough surfaces," *Physical Review B*, vol. 51, no. 8, pp. 5297–5305, 1995.

[31] K. Sakurai, M. Mizusawa, and M. Ishii, "Recent Novel X-ray Reflectivity Techniques: Moving Towards Quicker Measurement to Observe Changes at Surface and Buried Interfaces," *Transactions-Materials Research Society of Japan*, vol. 32, no. 001, pp. 181–187, 2007.

[32] K. Stoev and K. Sakurai, "Aberration effects in quick X-Ray reflectivity of curved samples," *IOP Conference Series: Materials Science and Engineering*, vol. 24, no. 1, 2011.

[33] K. Stoev and K. Sakurai, "Quick X-ray reflectivity of spherical samples," *Powder Diffraction*, vol. 28, no. 2, pp. 105–111, 2013.

[34] H. Joress, J. D. Brock, and A. R. Woll, "Quick X-ray reflectivity using monochromatic synchrotron radiation for time-resolved applications," *Journal of Synchrotron Radiation*, vol. 25, no. 3, pp. 706–716, 2018.

[35] H. Joress, J. D. Brock, and A. R. Woll, "Quick X-ray reflectivity using monochromatic synchrotron radiation for time-resolved applications," *Journal of Synchrotron Radiation*, vol. 25, no. 3, pp. 706–716, 2018.

[36] P. Beckmann and A. Spizzichino, *The scattering of electromagnetic waves from rough surfaces*. Goford: Pergamon Press, 1963.

[37] C. Heinzel and D. Grimme, "Modeling of surface generation in contour grinding of optical molds," *CIRP Annals - Manufacturing Technology*, vol. 55, no. 1, pp. 581–584, 2006.

[38] M. Cheng, C. F. Cheung, W. B. Lee, and S. To, "A Study of Factors Affecting Surface Quality in Ultra-Precision Raster Milling," *Key Engineering Materials*, vol. 339, no. May, pp. 400–406, 2007.

[39] R. N. Youngworth and B. D. Stone, "Simple estimates for the effects of mid-spatial-frequency surface errors on image quality," *Applied Optics*, vol. 39, no. 13, p. 2198, 2000.

[40] J. M. Tamkin, *A Study of Image Artifacts Caused By Structured Mid-Spatial Frequency Fabrication Errors On Optical Surfaces*. Doctoral dissertation, The University of Arizona, 2010.

[41] R. E. Parks, "Specifications: figure and finish are not enough," *An Optical Believe It or Not: Key Lessons Learned*, vol. 7071, p. 70710B, 2008.

[42] K. N. Stoev and K. Sakurai, "Review on grazing incidence X-ray spectrometry and reflectometry," *Spectrochimica acta, Part B: Atomic spectroscopy*, vol. 54, no. 1, pp. 41–82, 1999.

[43] M. S. Longuet-Higgins, "The Statistical Analysis of a Random , Moving Surface," *Philosophical Transactions of the Royal Society of London*, vol. 249, no. 966, pp. 321–387, 1957.

[44] P. R. Nayak, "Random process model of rough surfaces," *Journal of Tribology*, vol. 93, no. 3, pp. 398–407, 1971.

[45] D. E. Newland, *An Introduction to Random vibrations, spectral and wavelet analysis*. Longman Scientific Technical, 3 ed., 1993.

[46] A. A. MacDowell, D. Y. Parkinson, A. Haboub, E. Schaible, J. R. Nasiatka, C. A. Yee, J. R. Jameson, J. B. Ajo-Franklin, C. R. Brodersen, and A. J. McElrone, "X-ray micro-tomography at the Advanced Light Source," *Developments in X-Ray Tomography VIII*, vol. 8506, no. October 2012, p. 850618, 2012.

[47] H. Shahinian, *Fiber Based Tools for Polishing Optical Materials*. Doctoral dissertation, The University of North Carolina at Charlotte, 2018.

[48] V. L. Mironov, O. G. Udalov, B. A. Gribkov, and A. A. Fraerman, "Comparative x-ray reflectometry and atomic force microscopy of surfaces with non-Gaussian roughness," *Journal of Applied Physics*, vol. 104, no. 6, 2008.

[49] J. Lekner, *Theory of reflection of electromagnetic and particle wavees. Developments in Electromagnetic Theory and Application*. Martinus Nijhoff, 1987.

[50] M. Stedman and K. Lindsey, "Limits Of Surface Measurement By Stylus Instruments," *Surface Measurement and Characterization*, vol. 1009, no. March 1989, p. 56, 1989.

[51] M. Stedman, "Limits Of Surface Measurement By Optical Probes," *Surface Measurement and Characterization*, vol. 1009, no. March 1989, p. 62, 1989.

[52] R. K. Leach, C. L. Giusca, H. Haitjema, C. Evans, and X. Jiang, "Calibration and verification of areal surface texture measuring instruments," *CIRP Annals - Manufacturing Technology*, vol. 64, no. 2, pp. 797–813, 2015.

[53] R. Cook, "Creating microsphere targets for internal confinement fusion experiments," *Energy and Technology Review*, pp. 1–9, 1995.

[54] S. W. Haan, S. M. Pollaine, J. D. Lindl, L. J. Suter, R. L. Berger, L. V. Powers, W. E. Alley, P. A. Amendt, J. A. Futterman, W. K. Levedahl, M. D. Rosen, D. P. Rowley, R. A. Sacks, A. I. Shestakov, G. L. Strobel, M. Tabak, S. V. Weber, G. B. Zimmerman, W. J. Krauser, D. C. Wilson, S. V. Coggeshall, D. B. Harris, N. M. Hoffman, and B. H. Wilde, "Design and modeling of ignition targets for the National Ignition Facility," *Physics of Plasmas*, vol. 2, no. 6, pp. 2480–2487, 1995.

[55] B. Dumay, E. Finot, M. Theobald, O. Legaie, P. Baclet, J. Durand, and J. P. Goudonnet, " Atomic force microscopy investigation of a -C:H films prepared by plasma enhanced chemical vapor deposition for inertial confinement fusion experiments ," *Journal of Vacuum Science Technology A: Vacuum, Surfaces, and Films*, vol. 20, no. 2, pp. 366–374, 2002.

[56] J. Biener, D. D. Ho, C. Wild, E. Woerner, M. M. Biener, B. S. El-Dasher, D. G. Hicks, J. H. Eggert, P. M. Celliers, G. W. Collins, N. E. Jr, B. J. Kozioziemski, S. W. Haan, and A. V. Hamza, "Diamond spheres for inertial confinement fusion," *Nuclear Fusion*, vol. 49, no. 11, 2009.

[57] B. J. Kozioziemski, S. O. Kucheyev, J. B. Lugten, J. A. Koch, J. D. Moody, A. A. Chernov, E. A. Mapoles, A. V. Hamza, and L. J. Atherton, "Plastic deformation of solid hydrogen in fusion targets," *Journal of Applied Physics*, vol. 105, no. 9, 2009.

[58] V. A. Smalyuk, C. R. Weber, H. F. Robey, D. T. Casey, K. C. Chen, D. S. Clark, M. Farrell, S. Felker, J. E. Field, S. W. Haan, B. A. Hammel, A. V. Hamza, D. Hoover, J. J. Kroll, O. L. Landen, A. G. MacPhee, D. Martinez, A. Nikroo, and N. Rice, "Hydrodynamic instability growth of three-dimensional modulations in radiation-driven implosions with "low-foot" and "high-foot" drives at the National Ignition Facility," *Physics of Plasmas*, vol. 24, no. 4, 2017.

[59] D. S. Clark, A. L. Kritcher, S. A. Yi, A. B. Zylstra, S. W. Haan, and C. R. Weber, "Capsule physics comparison of National Ignition Facility implosion designs using plastic, high density carbon, and beryllium ablators," *Physics of Plasmas*, vol. 25, no. 3, 2018.

[60] J. N. Israelachvili, *Intermolecular and Surface Forces*. Academic Press, 3 ed., 2011.

[61] P. J. Van Zwol, G. Palasantzas, M. Van De Schootbrugge, J. T. M. De Hosson, and V. S. Craig, "Roughness of microspheres for force measurements," *Langmuir*, vol. 24, no. 14, pp. 7528–7531, 2008.

[62] J. Dalliant and A. Gilbert, *X-ray and neutron reflectivity: Principles and applications*. Springer, 2009.

[63] M. Marszałek, J. Jaworski, A. Michalik, J. Prokop, Z. Stachura, V. Voznyi, O. Böiling, and B. Sulkio-Cleff, "Structural and magnetoresistive properties of Co/Cu multilayers," *Journal of Magnetism and Magnetic Materials*, vol. 226-230, no. PART II, pp. 1735–1737, 2001.

[64] H. C. Su, C. H. Lee, M. Z. Lin, and T. W. Huang, "A Comparison Between X-ray Reflectivity and Atomic Force Microscopy on the Characterization of a Surface Roughness," *Chinese Journal of Physics*, vol. 50, no. 2, pp. 291–300, 2012.

[65] O. V. Penkov, I. A. Kopylets, M. Khadem, and T. Qin, "X-Ray Calc: A software for the simulation of X-ray reflectivity," *SoftwareX*, vol. 12, p. 100528, 2020.

[66] Y. Fujii, "Recent Developments in the X-Ray Reflectivity Analysis for Rough Surfaces and Interfaces of Multilayered Thin Film Materials," *Journal of Materials*, vol. 2013, pp. 1–20, 2013.

[67] I. Busch, Y. Azuma, H. Bettin, L. Cibik, P. Fuchs, K. Fujii, M. Krumrey, U. Kuetgens, N. Kuramoto, and S. Mizushima, "Surface layer determination for the Si spheres of the Avogadro project," *Metrologia*, vol. 48, no. 2, 2011.

[68] S. Festersen, S. B. Hrkac, C. T. Koops, B. Runge, T. Dane, B. M. Murphy, and O. M. Magnussen, "X-ray reflectivity from curved liquid interfaces," *Journal of Synchrotron Radiation*, vol. 25, no. 2, pp. 432–438, 2018.

[69] D. G. Chetwynd and S. T. Smith, "Strength degradation of ground and etched Si surfaces," in *New Materials and Their Applications* (D. Holland, ed.), vol. 111, pp. 493–495, Inst. Phys. Conf. Ser., 1990.

[70] J. D. Thousand, *DEVELOPMENT OF AN ADAPTIVE X-RAY RESEARCH FACILITY AND A DIRECT SILICON BONDED REFERENCE OBJECT FOR COMPUTED TOMOGRAPHY*. PhD thesis, The University of North Carolina at Charlotte, 2019.

APPENDIX A: BEAM FOOTPRINT CORRECTION IN X-RAY REFLECTIVITY MEASUREMENT

Due to the small angles of incidence in X-ray reflectivity measurements, if a sample face is small, the footprint of the X-ray beam will overfill the surface as illustrated in Figure A.1. The result of this overfill is a reduction in the incident intensity that must be corrected for; otherwise, the reflectivity will erroneously appear too low for incident angles less than the critical angle.

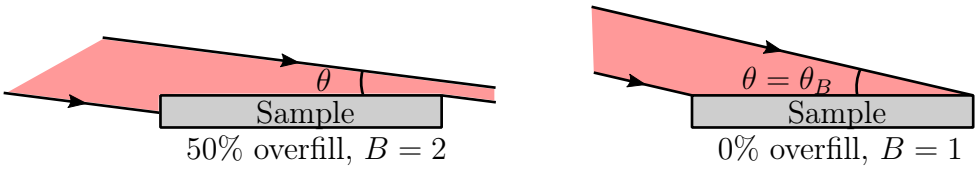

Figure A.1: At low angles of incidence, the beam will overfill the reflector surface resulting in erroneous normalization of the reflectivity curve.

To correct for the beam footprint reduction at low angles, the intensity reduction B must be determined as a function of the incident angle θ. The width of the beam footprint F on the part depends on the beam diameter d, sample reflector length L, and the incident angle θ, see Figure A.2.

The beam footprint is

$$F = \frac{d}{\sin\theta}. \tag{A.1}$$

The incident angle for which the beam is entirely on the sample face θ_B occurs when F is equal to L,

$$\begin{aligned} L &= \frac{d}{\sin\theta_B} \\ \theta_B &= \arcsin\frac{d}{L}. \end{aligned} \tag{A.2}$$

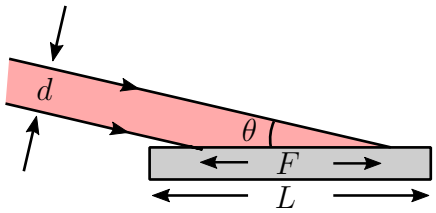

Figure A.2: System diagram of the beam footprint on the sample face as a function of the incident angle. The beam footprint F is a function of the incident angle θ, the beam diameter d, and the sample face length L.

For all angles less than θ_B, the incident beam intensity will be reduced by a factor B that is determined from the ratio of the reflector surface length and the total beam footprint

$$\begin{aligned} B &= \frac{L}{F} = \frac{d\sin\theta}{d\sin\theta_B} \\ &= \frac{\sin\theta}{\sin\theta_B}. \end{aligned} \tag{A.3}$$

APPENDIX B: SUCCESSFUL SYNCHROTRON BEAMLINE PROPOSALS

B.1 Advanced Light Source RAPIDD Proposal: Beamline 8.3.2

Beamline 8.3.2 at the Advanced Light Source is a Synchrotron-based Hard X-ray Micro-Tomography instrument. It allows non-destructive 3-Dimensional imaging of solid objects at a resolution of approximately 1 micron. (microct.lbl.gov)
Proposal Date: September 2021

1. Title of Experiment: Characterization of Curved Surfaces by X-Ray Reflectivity
2. Discipline of your proposal: Physics
3. Indicate the beamline required to perform the work described in your proposal: 8.3.2 (Tomography)
4. Indicate the earliest date you will be ready to collect data. If the beamtime is no longer useful after a certain date, the enter this also: Earliest 2 Sept 2021 - No longer useful after 15 Nov 2021
5. Number of shifts (8 hours beam time) requested: 1

Abstract `600 characters max including spaces`

The proposed research aims to validate a new model for the determination of surface roughness on curved surfaces using X-ray reflectivity. The motivation for this study is to determine surface perturbations on fusion capsule ablator layers that are known to create instabilities that significantly reduce yield in fusion reactions. This model will be evaluated by measuring small, highly polished spheres of known surface roughness. Data from these measurements will provide information spanning all parameters of the model, resulting in a new tool for mapping the roughness of polished spheres.

Proposal

The purpose of this work is to expand and validate a new X-ray reflectivity (XRR) model that includes the effect of high surface curvature; enabling the extraction of

XRR information. Objects having curved surfaces have many applications in optics, biophysics, high energy physics, and chemistry. In all of these fields, surface topography (roughness and waviness) has significant influence on function, often at nanometer scales. An example that forms the motivation for this study is the increasingly stringent functional requirement for fusion target ablator layer surface roughness. Reviews of current literature indicate that the influence of surface roughness on hydrodynamic instabilities during the ablation phase of implosion is a recurring, major factor limiting neutron yield for nuclear fusion energy production.

This model uses a method based on the original Parratt formalism employing Fresnel tensors including the effects of surface roughness induced specular and diffuse scattering. Due to the geometrical effects of curved surfaces, the combination of external surface roughness and transmission through the sample creates interference patterns at the detector; these patterns have been observed in previous experiments. The model developed in our work captures these additional effects and can be used to extract surface roughness from measurements of curved surfaces.

Due to the curvature of the surface, the contents of a single image include reflected and refracted X-rays from a continuum of incident angles. Modelling the surface and acquiring multiple measurements around the specimen provides the unique possibility of mapping localized surface topographic variations.

The proposed experiments will measure two spheres. The first sample is a polished, 2 mm, Silicon sphere provided by the National Ignition Facility and measured by General Atomics. The second sample is a 2 mm, SiC sphere that has been selectively polished to different roughnesses on two hemispheres. By measuring these samples, along with the variable parameters of the beamline, the datasets from these experiments will contain the information needed to fully evaluate the geometric and surface topographic components of the model.

Beamline Justification and Shift Requirement

The Advanced Photon Source has been successfully used in previous experiments for this project. These experiments have provided preliminary data containing interference effects that are predicted by our model; however, limitations at ALS Beamline 7.3.3 and APS Beamline 12-ID-B, which are both grazing-incidence X-ray small angle scattering (GIXSAS) beamlines, required substantial apparatus modifications and were determined to be not ideal for this study. One particular limitation in previous measurements was establishing reference datums due to the type of detector used where the sample surface was occluded; this information is necessary for direct comparison of the data with the model. Beamline 8.3.2 is a tomography beamline with the capability of imaging the direct X-ray beam alongside the sample and therefore does not have this limitation. At Beamline 8.3.2, variable X-ray energies, object-detector-distances (ODD), field of view, and beam size control will also enable a parametric study to evaluate our model. Additionally, we are familiar with the operation of this beamline, and the beamline scientists are familiar with the experimental requirements for this proposal.

The proposed experimental setup will require no modification to the beamline equipment and the samples will be pre-mounted on compatible fixtures to allow for quick set-up. Two samples will be measured, all operations on each sample can be automated, and the only manual interventions will be switching samples. Mounting and alignment is, from previous experience, expected to take approximately 2 hours for each sample. Measurement at 10 orientations, 4 energy levels, and 4 ODD's for a total of 160 images is expected to take 1 hour per sample. We are proposing one, eight-hour shift to complete the measurements.

B.2 Advanced Photon Source General User Proposal (GUP): Beamline 12-ID-B

Beamline 12-ID-B is a dedicated X-ray scattering beamline at APS. It routinely runs simultaneous small- and wide-angle X-ray scattering (SAXS/WAXS), grazing incidence small-angle X-ray (GISAXS), and grazing incidence wide-angle X-ray (GIWAXS). (12id.xray.aps.anl.gov)

Proposal Date: October 2020

Proposal Number: GUP-71407

Grazing Incidence Small-Angle X-ray Scattering Studies on Nanometer Scale Spherical Surface Roughness

Kathryn Harke[1], Jefferson Cuadra[1], Brian Rogers[1], Jacob Cole[2], Stuart Smith[2]

[1]1Nondestructive Evaluation Group, Lawrence Livermore National Laboratory, Livermore, CA

[2]Center for Precision Metrology, University of North Carolina, Charlotte, NC

This work was performed under the auspices of the U.S. Department of Energy by Lawrence Livermore National Laboratory under Contract DE-AC52-07NA27344 and was supported by the LLNL-LDRD Program under Project No. 19-ERD-022.

Proposal Abstract

The purpose of the proposed research is to validate a new model to determine the roughness of a solid, spherical surface using X-ray reflectivity (XRR). Previous XRR work has focused almost exclusively on flat surfaces and has established this method as a powerful tool for extracting the surface statistics of highly polished surfaces and smooth internal interfaces. However, today there are a large number of highly processed curved surfaces (e.g. EUV lithography, freeform, and X-ray optics, precision bearings, and internal confinement fusion targets) that require topographic measurement at the nanometer or sub-nanometer scale. Regarding internal confinement fusion

targets, a spherical shell from each batch is sacrificed to destructive testing to obtain the same information that is aimed be extracted non-destructively using this method. A model has been developed using the propagation of X-rays reflecting from, and refracting through, a specimen of constant curvature. This model will enable extraction of surface finish (roughness and waviness) from the internal and external surfaces of curved solids and shells. Figure B.1.a is a cartoon of the proposed experiment and Figure B.1.b is a simplified diagram of the propagation model that has been developed.

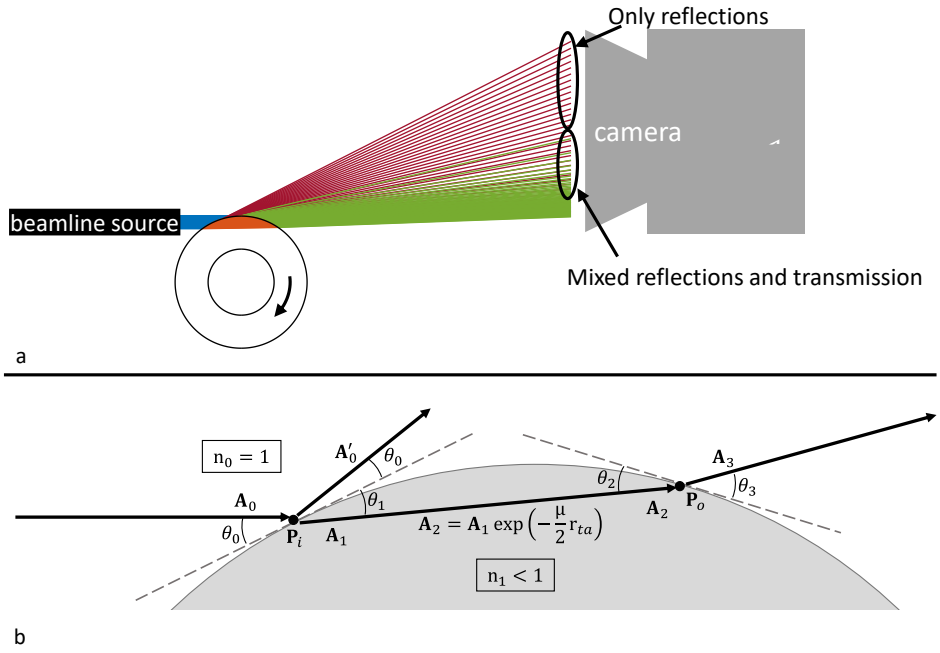

Figure B.1: Overview of experimental and theoretical goals of GISAX measurement. (a) Proposed experimental setup. Due to the constant curvature of the sphere, X-rays will be reflected from varying incident angles. Additionally X-rays will transmit through the sphere creating an interference pattern on the detector. (b) Propagation model diagram.

Beamline 12-ID-B has the capability to perform the proposed experiments which require high-resolution grazing incidence small angle scattering measurements at multiple energies from a high flux source on both solid and hollow spherical and cylindrical

samples. Our samples consist of;

1. one, G25, 2 mm diameter, solid tungsten carbide sphere polished on one hemisphere from UNCC;
2. two, polished 2 mm diameter Silicon spheres from the National Ignition Facility (NIF);
3. two, polished G5, 2 mm diameter 440c stainless steel spheres from Bal-tec;
4. two each, 2 mm diameter, SiC and Si3N4 spheres lapped on one hemisphere (80 nm RMS roughness) and polished on one hemisphere (5 - 10 nm RMS roughness) from Diamond Product Solutions (DPS);
5. two, 10 μm thick, diamond coated SiC spheres from DPS with the same size and surface specifications;
6. two 1 mm diameter epoxy resin hollow cylinders from LLNL NanoScribe;
7. and two, 2 mm diameter, high density carbon spherical shells.

The samples will be characterized using AFM, profilometry, and traditional microscopy. By studying these proposed samples we can validate the XRR method for surface roughness measurements on external curved surfaces at 12-ID-B, which can be used with our model to look at applying the X-ray Reflectivity method to probe internal surface roughness of a thin spherical shell, the ultimate goal of the project, which has never been accomplished before. A related study to determine surface roughness and waviness on a glass optic in which a novel model for extracting these features was developed by the authors and experiments were performed at The Advanced Light Source Beamline 8.3.2, a dedicated tomography beamline [1]. Notwithstanding differing instrument bandwidth capabilities, the XRR model was

validated experimentally with AFM, Fizeau interferometry, and surface profilometry measurements. Synchrotron experiments required non-traditional XRR measurements, and experience with designing and fabricating apparatus for incorporation into synchrotron facilities uniquely prepare us for the proposed experiments.

Table B.1: Summary of results from previous work with XRR on surfaces containing roughness and waviness components. A novel model was developed to extract surface statistics from distinct surface wavelengths.

	Roughness [nm]	Waviness [nm]
XRR	2.9 ± 0.2	14.6 ± 0.5
Profilometry	4.0 ± 0.1	21.4 ± 0.1
AFM	3.4 ± 0.4	
Fizeau		21.6

If this work is a continuation of work done under a previous proposal, give the previous proposal number and indicate what changes have been made. (REQUIRED FIELD)(limit : 3000 characters)

This is a new beamtime proposal.

What is the scientific or technical purpose and importance of the proposed research? (REQUIRED FIELD)(limit : 500 words)

For certain parts where nanometer scale surface roughness directly determines the performance and the potential for failure of a component during application, the measurement of internal and external surface roughness information before subjecting the component to application can have significant and beneficial outcomes. As inertial confinement fusion experiments and studies in high energy density science continue to seek fusion ignition, the inspection requirements of the capsule ablators, i.e. hollow spheres, are becoming more stringent. Qualities such as surface finish and particle contaminants are especially important. Currently, targets are sacrificed to destructive testing to determine a representative measure of the internal surface. This method is undesirable as significant manufacturing resources are lost and the quality of specific targets can only be inferred. Without the knowledge of the quality of each target used, performance metrics such as neutron yield cannot be correlated with direct

measurements.

Traditional, surface metrology measurement tools such as profilometry, atomic force microscopy (AFM), and scanning white light interferometry are limited by finite probe size, and contact-based profiling methods (AFM, stylus) while potentially damaging the surface also require stitching of 2D profiles resulting in slow measurement times for high lateral spatial resolution. These current methods are also only applicable to external sample surfaces, and internal defects and surface structure remain undetected.

To address these issues, we propose a method utilizing X-ray scattering from curved surfaces in the region near grazing incidence. Grazing incidence small angle X-ray scattering has the potential to non-destructively measure the surface structure of both the outside and inside surfaces of hollow spheres. This builds upon current methods of sub-surface X-ray measurement commonly used to evaluate the roughness of layer interfaces in the semiconductor and optical coating industries; almost exclusively on flat surfaces. The detection and characterization of these physical features is on the lateral scale of the X-ray wavelength which can be at ångström levels. The intensity of the scattered light from a surface is directly related to the surface features of the scattering interface.

The development of a model for the extraction of surface features from non-flat specimens represents a novel technique in X-ray reflectometry. This work has the potential to open a field of studies on the extraction of functional measurement information from non-traditional surface shapes in emerging fields. Examples include freeform and engineering surfaces important to defense, virtual and augmented reality systems, and compact smartphone camera optics as well as catadioptric lenses for EUV lithography and X-ray optics for microscopes and telescopes.

Why do you need the APS for this research? (REQUIRED FIELD)(limit:100 words)

While it is possible to obtain preliminary single-energy data from lab-based X-ray facilities, the features of the Advanced Photon Source such as high flux, tunable energy, long flight-path, and high-fidelity detection are necessary for rigorous evaluation of this new model. Additionally, high flux sources enable rapid data collection for numerous measurements. This is often necessary due to the statistical nature of surface roughness and surface roughness variations. Furthermore, long flight paths enable large spread in the scattered light, increasing the effective spatial resolution of measurements.

Why do you need the beamline you have chosen? (REQUIRED FIELD)(limit : 100 words)

Beamline 12-ID-B has the desired angular resolution needed to obtain meaningful data to compare with our models. The angular region of interest for this study is below 3°, with greater importance in the sub 0.5° range. This beamline has the capability to study this angular region of interest with sufficient object-to-detector distance. The energy range, $7.9-14$ keV and the focused beam size, 200 μm x 40 μm, available at 12-ID-B are ideal for this experiment. Previously, preliminary measurements were fixed to 10 keV, 176 μm/pixel, and 0.001° steps to 0.5° at ALS Beamline 8.3.2.

Describe the participants' previous experience with synchrotron radiation and the experimental results obtained. (If you refer to previous publications, be sure to include complete citations.) (REQUIRED FIELD)(limit : 100 words)

After consultation with beamline scientists (Dr's B.Lee and C.Kurtz), two types of experiments will be performed:

The first experiments will perform X-ray reflectivity measurements of outer surfaces of spheres (Samples $1-4$). The experiment will require a rotary stage with angular resolution of **at least** 0.010° ideally with 360° of rotation, a collimated beam with

multiple energies from $7 - 14$ keV, and ODD of at least 3 m. We will scan with fine resolution up to an angle of 3° for each measurement; however, due to the intentionally varied surface of Samples 1 and 4, it will be necessary to coarsely index 360° at approximately 1° increments. If sample rotation is not possible, it would be necessary to measure each side of the sphere, remove and rotate the sample holder 180°, then re-measure the back side of the sphere to obtain two pairs of measurements.

Experimental parameters will be predetermined using our model but may need to be adjusted during experiments. Additionally, we plan to work with the beamline scientists to ensure that sample fixturing will be compatible with the designed sample holder. To avoid damage to the Pilatus 2M detector, the sample must always occlude the direct beam. Initially, the sample will be placed at the center of rotation of the rotary table directly in front of the beam. The sample will be translated across the beam allowing for more scattered light to reach the detector until a maximum intensity is achieved. It is important that there be minimal run-out in the rotation to ensure that the detector is not exposed to the direct beam during sample rotation. To measure this run-out, the beamstop image can be monitored as the sample is rotated and the x-y stages used to correct for position variations.

Additionally, the center-of-the-beam must be aligned to the center of the sphere. This will result in an uneven scattering pattern on the detector. Translation of the z-stage will correct for this error. This alignment process may need to be repeated until the beam-sphere alignment is optimized.

Images will be collected of the scattered light and transferred for post-processing on another computer. Any extraction methods (header files or programs) will need to be made available so that data can be imported into Matlab.

The second experiments will measure both internal and external surfaces of spheres and cylinders (Samples $5 - 7$) and will require the same setup, equipment and alignment requirements as the exterior surface experiments. The measurement process for

Samples 5 and 7 will be the same as before; however, the printed epoxy resin partial hollow cylinders will be pre-mounted to align the arc of the cylinder to the sample holder. The translation across the beam to optimize the inclusion of low angle scatter will be the same for this sample.

All samples, both solid and hollow, will also be measured at LLNL using AFM, white light interferometry and profilometry methods to compare and validate our theoretical X-ray reflectivity models when applied to the experimental data acquired at this beamline.

Provide an overall estimate of the amount of beam time you will need to accomplish the goals of your proposed experimental program. How many visits during the two-year proposal period do you expect to need? How many shifts will you need during each visit (approximately)? (REQUIRED FIELD)(limit : 500 words)

Based on previous experience fielding experiments on similar samples, it is expected that six 8-hour shifts are needed for the full lifetime of the proposal. During the first shift, we aim to establish ideal experimental set-up and procedures ($3-6$ hours) as well as measuring Sample 1. The second shift will use the established parameters and protocols to measure Samples $2-4$. It is possible that upon analysis of data additional measurements for the solid samples might be needed. This could require part of an additional shift. Hollow shells will require significantly more setup and measurement times. We plan to use shift 3 for possible additional measurement of Samples $1-4$ and the remaining of the shift dedicated to shell setup and measurement of Sample 5. The following shift (shift 4) will consolidate measurements on Sample 5 if necessary and complete measurements on Sample 7. Sample 6, the printed partial cylinder, will require the majority of the final two shifts as measurements will need to be acquired from both the front and back sides of the sample.

We are asking for three 8-hour shifts in the first quarter to complete measurement

of the solid samples with a minimum of two 8-hour shifts required should scheduling constraints arise. We are asking for three 8-hour shifts in the second quarter for the measurement of Samples $5-7$ where a minimum of two 8-hour shifts would be required. The minimum times required assume that all experiments work out as planned and there are no interruptions in beamtime.

In summary, the six 8-hr beamtimes would consist of

1. Setup, parameter refinement, measurement of Sample 1;
2. Setup, measurement of Samples $2-4$;
3. Setup, measurement of Sample 5;
4. Setup, measurement of Sample 7;
5. Setup, measurement of Sample 6 front;
6. Setup, measurement of Sample 6 back.

List publications resulting from work done at the APS. Please identify the beamline(s) where the work was done (REQUIRED FIELD)(limit: 2000 characters)

Beamline 16-BM-B:

Publications:

A. Andrew A. Wereszczak, Kathryn J. Ham, Yogesh K. Vohra, Georgiy M. Tsoi, Brian A. Oistad, Brett S. Kuwik, Emily F. Steiner, Osama M. Jadaan, Benjamin L. Hackett. Oak Ridge National Laboratory Report No. ORNL/TM-2018/1019, *High-Pressure Mechanical Response of Two Vitreous Silicates*, (2018).

B. Ham, K. J.; Kono, Y.; Patel, P. J.; Kilczewski, S. M.; Vohra, Y. K. *Pressure Induced Densification and Compression in a Reprocessed Borosilicate Glass*. Materials. 11, 114 (2018). doi: 10.3390/ma11010114

C. Kathryn J. Ham, Yogesh K. Vohra, Yoshio Kono, Andrew A. Wereszczak, and Parimal Patel, "White-beam X-ray diffraction and radiography studies on high-boron-containing borosilicate glass at high pressures", High Pressure Research 2017. http://dx.doi.org/10.1080/08957959.2017.1287263

Manuscript in preparation:

D. Kathryn J. Harke, Rostislav Hrubiak, Curtis Kenney-Benson, and Yogesh Vohra. *High-Pressure, High-Temperature White-Beam X-ray Diffraction and Radiography Studies on a Zr-Based Bulk Metallic Glass.* Journal of Materials Research. (July 2020).

M.S. in Physics thesis:

E. Kathryn Jinae Ham. "White-Beam X-Ray Diffraction and Radiography Studies on High-Boron Containing Borosilicate Glass at High Pressures". (July 14, 2017).

Ph.D. in Physics dissertation:

F. Kathryn Jinae Ham. "High-Pressure Studies on Borosilicate and Bulk Metallic Glasses". (May 16, 2019).

**Kathryn Harke was previously known as Kathryn Ham prior to marriage.*

References (limit : 2000 characters)

1. J. A. Cole, J. A. Cuadra, R. M. Panas, S. T. Smith. The Effect of Longer-Range Waviness on X-Ray Reflectivity Measurements. Journal of Synchrotron Radiation (at press). 2020.

2. K. Mohan, R. Panas, and J. Cuadra. "SABER: A Systems Approach to Blur Estimation and Reduction in X-ray Imaging." arXiv preprint arXiv:1905.03935. (Under Review).

3. B. Liang, J. Cuadra, et al. "Stress field analysis in a stony meteorite under thermal fatigue and mechanical loadings." Icarus 335. 2019.

4. J. Indeck, J. Cuadra, C. Williams, K. Hazeli. "Accumulation and evolution of elastically induced defects under cyclic loading: quantification and subsequent properties." International Journal of Fatigue. 2019.

5. S.K. Saha, J. Oakdale, J. Cuadra, et al. "Radiopaque resists for two-photon lithography to enable submicron 3D imaging of polymer parts via X-Ray computed tomography." ACS Applied Materials & Interfaces 10, no. 1. 2018.

6. S.K. Saha, C. Divin, J. Cuadra, R.M. Panas. "Effect of proximity of features on the damage threshold during submicron additive manufacturing via two-photon polymerization." ASME. J. Micro Nano-Manuf. 2017.

B.3 Advanced Light Source Rapid Access Proposal: Beamline 7.3.3

Beamline 7.3.3 is a SAXS/WAXS/GISAXS/GIWAXS beamline, covering a wide q range (0.004 - 3 $Å^{-1}$) and length scale (2 - 1500 Å). (saxswaxs.lbl.gov)

Proposal Date: February 2020

Nanometer Scale Surface Roughness Measurement of Spherical Surfaces via XRR

As inertial confinement fusion (ICF) experiments and studies in high energy density (HED) science continue to seek fusion ignition, the inspection requirements of the capsule ablators, i.e. hollow spheres, are becoming more stringent, e.g. high surface quality finish and minimal particle contaminants. Traditional, non-destructive measurement techniques such as profilometry, AFM, and scanning white light interferometry are limited due to the high surface slopes and relatively large surface area requirements to map these spheres. To address these needs, a method utilizing X-ray scattering by the modifying existing theories for scattering from flat surfaces is attempted. In particular, the goal is to create and experimentally validate a model that circumvents the challenges of studying reflections from the interior and exterior surfaces of cylindrical and spherical shells. Because the model calculates reflectivity as a function of surface roughness it is necessary to obtain preliminary experimental measurements to evaluate the model's predictive value. **The expected outcome** of the measurement using this beamline is a demonstration of differences in reflectivity for regions of different roughness on a spherical surface. Therefore, during this beamtime, spheres made from SiC and Si, will be studied. These spheres have been selectively polished to optical smoothness (e.g. > 5 nm RMS) on one side while the other side is left rough from the manufacturer (~ 100 nm RMS); and its surface has been characterized using atomic force microscopy.

For each angular position, X-rays will scatter from the surface with their intensity decreasing and take-off angle increasing as the radiation is incident upon the sphere

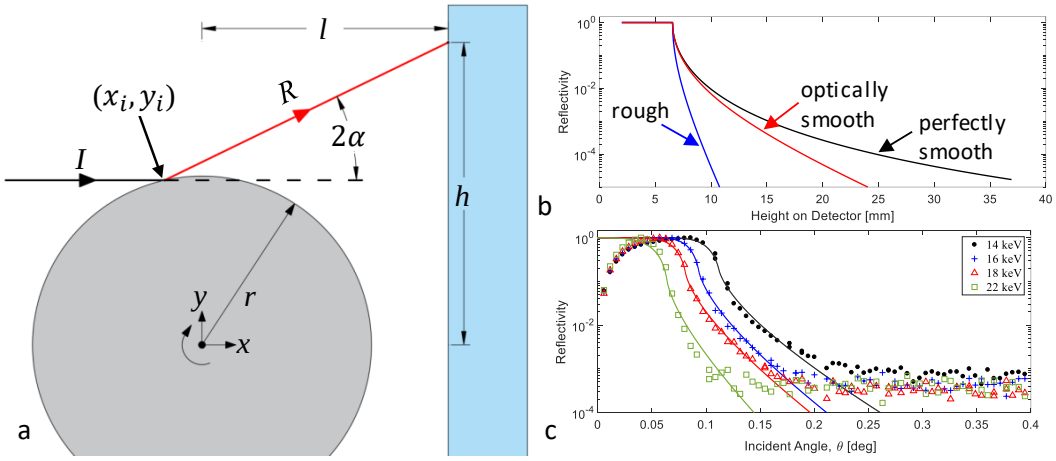

Figure B.2: (a) Simplified diagram of the experimental method depicting only one ray of the X-ray beam. The incident beam I will be incident upon the sphere and the reflected ray R will arrive at the detector at a position h depending on the location of incidence (x_i, y_i) and the sample to detector distance l. (b) By scanning vertically with the detector, the intensity of the reflected X-rays can be mapped as a function of height. The decay of the reflectivity is a function of the roughness of the surface. (c) Experimental reflectivity data obtained at beamline 8.3.2 on a flat surface. Angular resolution and positioning accuracy are major issues as well as low integration times leading to noise floor at low angles.

at higher angles. A scan in the vertical direction will provide a map of the intensity of the reflections as a function of height above the surface (denoted as h in Figure 1a). The intensity of the reflected X-rays will provide information about the surface finish of the sample surface. **The use of beamline 7.3.3** will be crucial for this study since its configuration for reflectivity measurements could potentially provide additional key information for the model under development. Also compared to **previous measurements using beamline 8.3.2**, which produced measurements for flat surfaces [1], the limiting angular resolution and restricted sample to detector distance can be alleviated at beamline 7.3.3 for the curved surface work. This is especially important as measurement ranges are typically $2-3$ deg with the first 0.5 deg having the most signal and information.

Based on previous experience, allowing time for setup and alignment (typically 3 to 4 hours for a new experiment), it is possible to measure around regions of the sphere

with small step sizes **with 2 shifts at the beamline 7.3.3**. The sphere is mounted on a post that must be installed into the system and its central axis aligned to the rotation axis. Once aligned, the measurement will require multiple steps to scan the reflections at several positions around the sphere.

Principle investigator (PI), Dr. K. Aditya Mohan

Dr. Aditya Mohan is a Signal and Image Processing Engineer with the Computational Engineering Division at LLNL and the PI for an LDRD project investigating high resolution inspection methods via X-ray phase contrast imaging and reflectometry, which supports this proposed work. He completed his Ph.D. in electrical and computer engineering from Purdue University. His expertise includes computational imaging, inverse problems, and machine learning.

References (project team members' names underlined)

1. J. A. Cole, J. A. Cuadra, R. M. Panas, and S. T. Smith, "The effect of longer-range waviness on X-ray reflectivity measurements," Journal of Synchrotron Radiation, vol. 28, 2021.

2. K. A. Mohan, R. M. Panas, and J. A. Cuadra. "SABER: A Systems Approach to Blur Estimation and Reduction in X-ray Imaging." in IEEE Transactions on Image Processing, vol. 29, pp. 7751-7764, 2020.

APPENDIX C: MATLAB SCRIPTS AND FUNCTIONS

C.1 Figure 2.3 Multilayer Reflections

```
% ------------------------------------------------------- %
% Jacob Cole -- 7 January 2021                            %
% MATLAB program generating Kiessig fringes from a        %
% multilayer using the Parratt reflectivity model.        %
% Adapted from "Elements of Modern X-Ray Physics" by Als  %
% Nielson and Des Morrow.                                 %
% -------------------------------------------------------%

clearvars
r0 = 2.82e-6; % Thompson scattering length [nm]
theta0 = 20e-6:20e-6:50000e-6; % incident angles [rad]
lambda = 0.12398; % radiation wavelength [nm]
Delta = [1 4]; % Ir and Si bilayer thickness [nm]
k = 2*pi/lambda; % [nm]
beta = [2.3386e-6 7.3544e-8];
mu = 2*k*beta; % absorption coefficient of Ir and Si
rho = [22560 2330]; % Ir and Si density [kg/m^3]

Q = 2*k*sin(theta0); % wavevector transfer [nm]
bl = rho*r0 + 1i*mu; % bilayer scattering vector
% multilayer scattering vector
ml = [bl bl bl bl bl bl bl bl bl bl 0.1e-20];
delta = lambda*lambda*real(ml)/(2*pi);
beta_ml = lambda/(4*pi)*imag(ml);
```

```
25 % multilayer layer thickness
26 Delta_ml = [Delta Delta Delta Delta Delta...
27     Delta Delta Delta Delta Delta];
28 N = length(ml);
29
30 % wavevector transfer for each layer
31 Q = reshape(Q,1,length(Q));
32 for ii = 1:N
33     Qj(ii,:) = sqrt(Q.^2 - 8*k*k*delta(ii) +...
34         1i*8*k*k*beta_ml(ii));
35 end
36 Qj = [Q;Qj];
37
38 % reflectivity coeff
39 for ii = 1:N
40     r(ii,:) = ((Qj(ii,:)-Qj(ii+1,:))./...
41         (Qj(ii,:)+Qj(ii+1,:)));
42 end
43
44 % first layer reflectivity
45 I = r(1,:);
46 if N > 1
47     R(1,:) = (r(N-1,:)+r(N,:).*exp(1i*Qj(N,:)*...
48         Delta_ml(N-1)))./(1+r(N-1,:).*r(N,:)....
49         *exp(1i*Qj(N,:)*Delta_ml(N-1)));
50 end
51
```

```
% reflectivity from other layers
if N > 2
    for ii=2:N-1
        R(ii,:) = (r(N-ii,:)+R(ii-1,:).*...
            exp(1i*Qj(N-ii+1,:)*Delta_ml(N-ii))./...
            (1+r(N-ii,:).*R(ii-1,:).*...
            exp(1i*Qj(N-ii+1,:)*Delta_ml(N-ii)));
    end
end

% reflectivity intensity
if N == 1
    I = r(1,:);
else
    I = R(N-1,:);
end

I = abs(I).^2;
semilogy(theta0*180/pi,I)
ylim([1e-6 1.5])
```

C.2 Figure 2.5 Reflectivity for Various Surface Roughness

```
clearvars
chi = pi/4; % incident radiation polarization
Energy_eV = 17479.34; % MoKa source [eV]
h_pc = 6.62607e-34; % Planks constant [J*s]
eV = 1.602176634e-19; % [J/eV]
c = 299792458; % velocity of light [m/s]
delta=2.3e-6; % real part of refractive index unit
   decrement
beta=1.25e-8; % imaginary part of refractive index unit
   decrement
sigma = 1e-9; % RMS roughness [m]
thetac = sqrt(2*delta);
thetastart = 0;
thetastop = 6*thetac;
N = 1000;

Energy_J = Energy_eV*eV; % incident radiation energy [
   Joules]
frequencyLambda = Energy_J/h_pc; % incident radiation
   frequency [Hz]
omegaL = 2*pi*frequencyLambda; % incident radiation
   frequency [rad/s]
lambda = c/frequencyLambda; % incident radiation
   wavelength (vacuum) [m]
k = 2*pi/lambda; % wave-number [1/m]
```

```
20 n1 = 1 - delta + 1i*beta; % material refractive index (
      complex)
21 theta0 = linspace(thetastart,thetastop,N); % incident
      angle [rad]
22 theta1 = acos(cos(theta0)/n1); % refracted angle [rad] (
      complex)
23 k0z = k*sin(theta0); % z component of the incident
      radiation
24 % wave-vector [1/m]
25 k1z = k*sqrt(n1*n1-cos(theta0).*cos(theta0)); % z
      component of the
26 % transmitted radiation wave-vector [1/m] (complex)
27 Psi_01x = (k1z - n1*n1*k0z)./(n1*n1*k0z + k1z); % x
      component
28 % of the reflection tensor
29 Psi_01y = (k0z - k1z)./(k0z + k1z); % y component of the
      reflection
30 % tensor (compex)
31 f_sigma = @(sigma) exp(-2*k0z.*k1z*sigma*sigma);
32 f_sigma1 = f_sigma(sigma); % surface roughness
33 f_sigma2 = f_sigma(2*sigma); % surface roughness
34 f_sigma4 = f_sigma(4*sigma); % surface roughness
35
36 % reflectivity intensity no roughness
37 R = Psi_01x.*conj(Psi_01x)*sin(chi)*sin(chi) + ...
38     Psi_01y.*conj(Psi_01y)*cos(chi)*cos(chi);
39 T_fujii = 1 - R;
```

```
40 % reflectivity intensity roughness
41 R_rough1 = f_sigma1.*R;
42 R_rough2 = f_sigma2.*R;
43 R_rough4 = f_sigma4.*R;
44
45 figure(1);
46 clf
47 semilogy(theta0/thetac,R,'k','DisplayName','smooth')
48 hold on
49 semilogy(theta0/thetac,R_rough1,'.-k','MarkerIndices'
      ,1:20:N,...
50     'MarkerSize',9,'DisplayName','\sigma = 1 nm')
51 semilogy(theta0/thetac,R_rough2,'o-k','MarkerIndices'
      ,1:20:N,...
52     'MarkerSize',6,'DisplayName','\sigma = 2 nm')
53 semilogy(theta0/thetac,R_rough4,'*-k','MarkerIndices'
      ,1:20:N,'DisplayName','\sigma = 4 nm')
54 hold off
55 legend show
56 ylim([1e-4 1.1])
```

C.3 Figure 2.6 Comparison of Roughness Models

```
clearvars
chi = pi/4; % incident radiation polarization
Energy_eV = 17479.34; % MoKa source [eV]
h_pc = 6.62607e-34; % Planks constant [J*s]
eV = 1.602176634e-19; % [J/eV]
c = 299792458; % velocity of light [m/s]
delta=2.3e-6; % real part of refractive index unit
   decrement
beta=1.25e-8; % imaginary part of refractive index unit
   decrement
sigma = 4e-9; % RMS roughness [m]
thetac = sqrt(2*delta);
thetastart = 0;
thetastop = 6*thetac;
N = 100000;

Energy_J = Energy_eV*eV; % incident radiation energy [
   Joules]
frequencyLambda = Energy_J/h_pc; % incident radiation
   frequency [Hz]
omegaL = 2*pi*frequencyLambda; % incident radiation
   frequency [rad/s]
lambda = c/frequencyLambda; % incident radiation
   wavelength (vacuum) [m]
k = 2*pi/lambda; % wave-number [1/m]
```

```
20 n1 = 1 - delta + 1i*beta; % material refractive index (
   complex)
21 theta0 = linspace(thetastart,thetastop,N); % incident
   angle [rad]
22 theta1 = acos(cos(theta0)/n1); % refracted angle [rad] (
   complex)
23 k0z = k*sin(theta0); % z component of the incident
   radiation
24 % wave-vector [1/m]
25 k1z = k*sqrt(n1*conj(n1)-cos(theta0).*cos(theta0)); % z
   component of the
26 % transmitted radiation wave-vector [1/m] (complex)
27 Psi_01x = (k1z - n1*n1*k0z)./(n1*n1*k0z + k1z); % x
   component
28 % of the reflection tensor
29 Psi_01y = (k0z - k1z)./(k0z + k1z); % y component of the
   reflection
30 % tensor (compex)
31 Psi_01z = -Psi_01x; % z component of the reflection tensor
32
33 Phi_01x = (2*k1z)./(n1*conj(n1)*k0z + k1z); % x component
   of the refraction
34 % tensor
35 Phi_01y = (2*k0z)./(k0z + k1z); % y component of the
   refraction
36 % tensor (compex)
```

```
37 Phi_01z = (2*k0z)./(n1*conj(n1)*k0z + k1z); % z component
      of the refraction
38
39 A0dash = [-Psi_01x*sin(chi).*sin(theta0)
40     Psi_01y*cos(chi)
41     Psi_01z*sin(chi).*cos(theta0)];
42 A1 = [-Phi_01x*sin(chi).*sin(theta0)
43     Phi_01y*cos(chi)
44     Phi_01z*sin(chi).*cos(theta0)];
45 A1 = A1.*sqrt(real(k1z)./k0z);
46
47 f_NC = @(sigma) exp(-2*k0z.*k1z*sigma*sigma);
48 f_DW = @(sigma) exp(-2*k0z.*k0z*sigma*sigma);
49 f_DWBA = @(sigma) exp(1-2*k0z.*k0z*sigma*sigma);
50 f_Sinha = @(sigma) exp(-4*k*k*sin(theta0).*sin(theta1)*
      sigma*sigma);
51 A1_sigma = @(sigma) A1.*exp((k0z-k1z).*sigma*sigma/2);
52
53 R = dot(A0dash,A0dash);
54 R_NC = R.*f_NC(sigma);
55 R_DW = R.*f_DW(sigma);
56 R_DWBA = R.*f_DWBA(sigma);
57 R_Sinha = R.*f_Sinha(sigma);
58
59 figure(1);clf
60 semilogy(theta0/thetac,R_NC,'k','linewidth',1,'DisplayName
      ','NC')
```

```
61 hold on
62 semilogy(theta0/thetac,R_DW,'.-k','linewidth',1,...
63     'MarkerIndices',1:1000:N,'MarkerSize',9,'DisplayName',
         'DW')
64 semilogy(theta0/thetac,R_DWBA,'o-k','linewidth',1,...
65     'MarkerIndices',1:1000:N,'MarkerSize',6,'DisplayName',
         'DWBA')
66 semilogy(theta0/thetac,R_Sinha,'*-k','linewidth',1,...
67     'MarkerIndices',1:1000:N,'DisplayName','Sinha')
68 hold off
69 legend show
70 ylim([1e-4 10])
```

C.4 Figure 3.2 Comparison of Waviness Model with Traditional Model

```
% Effect of surface mosaic on the measured intensity...
% Jacob Cole

clearvars
energies = [14];
for ienergy = 1:length(energies)
    h = 4.136e-15; % planck constant [eV*s]
    c = 3.000e+08; % speed of light [m/s]
    d = @(E) 556.25*E^(-2.01); % delta of BK7
    ac = sqrt(2*d(energies(ienergy)*1000)); % critical
       angle [rad]


    sigma = 2E-9; % RMS surface roughness [m]
    sigmaL = 20E-9; % RMS surface waviness [m]
    w0 = 1/(15e-6); % spectral density filter cutoff
       frequency [m^-1]

    a_start = 0; % starting incident angle [deg]
    a_stop = 0.5; % ending incident angle [deg]
    N_a = 1000; % number of incident angle points to
       calculate

    alpha = linspace(a_start*pi/180, a_stop*pi/180, N_a);
       % vector of incident angles [rad]
```

```
22      lambda = h*c/(energies(ienergy)*1000); % source
           wavelength [m]
23      S0 = sigmaL*sigmaL/(pi*w0); % initial spectral density
24      m2 = 0.429*S0*w0*w0*w0; % mean square surfa ce slope
25
26      tol = 1e-9;
27      lb = -3*sqrt(m2); % lower integration bound
28      ub = -lb; % upper integration bound
29
30      %%%%%%%%%%%%%%%%%%%%%%%%%%%%%%%%%%%%%%%%%%%%%%%%%%%%%%%%%%%%
31      % R(alpha) returns the Bahr reflectivity amplitude for
            a given incident
32      % angle, alpha. Use R(alpha)*conj(R(alpha)) to return
           the reflectivity
33      % intensity.
34
35      ap = @(a) acos(cos(a)./cos(ac)); % refracted angle [
           rad]
36      qz = @(a) 2.*pi.*sin(a)./lambda; % wave-vector
           transform (incident)
37      qzt = @(a) 2.*pi.*sin(ap(a))./lambda; % wave-vector
           transform (inside)
38
39      R = @(a) sinh((pi./2).^1.5 .* sigma .* (qz(a) - qzt(a)
           ))./...
40              sinh((pi./2).^1.5 .* sigma .* (qz(a) + qzt(a)
                   ));
```

```
41
42      %%%%%%%%%%%%%%%%%%%%%%%%%%%%%%%%%%%%%%%%%%%%%%%%%%%%%%%%%%%%%%%%
43      % P(zeta) returns the probability density given a mean
            slope, zeta.
44
45      P = @(zeta) exp(-zeta.*zeta./2./m2)./sqrt(2.*pi.*m2);
46
47      %%%%%%%%%%%%%%%%%%%%%%%%%%%%%%%%%%%%%%%%%%%%%%%%%%%%%%%%%%%%%%%%
48
49      Q = @(a,zeta) R(a + zeta).*conj(R(a + zeta)).*P(zeta);
50      I = @(a) quad(@(zeta) Q(a,zeta),0,ub,tol);
51
52      for i = 1:N_a
53
54          r_bahr = R(alpha(i));
55          R_bahr(i) = r_bahr*conj(r_bahr);
56          R_wav(i) = 2*I(alpha(i));
57
58      end
59      R_wav = R_wav/max(R_wav);
60      alphadeg = alpha.*180/pi;
61      figure
62      semilogy(alphadeg,R_wav,'linewidth',2,'displayname','
            Equation 13')
63      hold on
64      semilogy(alphadeg,R_bahr,'linewidth',2,'displayname','
            Equation 9')
```

```
65      legend show
66      ylabel('Intensity')
67      xlabel('Incident Angle, \alpha [deg]')
68      ylim([0 1.5])
69      savefilename = strcat('wavinessTheory',num2str(
           energies(ienergy)),'keV.mat');
70      save(savefilename,'alphadeg','R_wav');
71  end
```

C.5 Figure 3.4 Profilometer Measurement Data Decomposition

```
clearvars
% load in data from data files
datain = dlmread('12_18_2019_back_morph5.txt',' ',59,2);
hsf_range = [1e-6 16e-3]; % range of roughness spatial
   wavelengths [mm]
msf_range = [16e-3 4]; % range of waviness spatial
   wavelengths [mm]


% split data into x and height
xdata = datain(1+221:end-221,1); % x data [mm]
xdata = xdata - xdata(1); % shift x data to zero [mm]
hdata = datain(1+221:end-221,3); % height data [mm]

hdata_form_removed = dt(xdata,hdata,' ',[0 50 500 500]); %
    remove form [mm]
[h_rough,h_wav] = freq_dom_filt(xdata, hdata_form_removed,
   hsf_range,msf_range); % frequency filter heights

Rq = sqrt(sum(h_rough.^2)/length(xdata));  % RMS Roughness
    [mm]
Wq = sqrt(sum(h_wav.^2)/length(xdata));  % RMS Waviness [
   mm]

fprintf('Rq =   %0.3f nm       \n',Rq*1e6)
fprintf('Wq =   %0.3f nm       \n',Wq*1e6)
```

```
21
22 figure(1);
23 subplot(211)
24 plot(xdata,h_rough*1e6,'k','displayname','roughness');
25 xlabel('x, mm');ylabel('height, nm')
26 title('roughness, \omega < 1/16 \mu{}m^{-1}')
27 ylim([-30 30])
28 subplot(212)
29 plot(xdata,h_wav*1e6,'k','displayname','waviness')
30 xlabel('x, mm');ylabel('height, nm')
31 title('waviness, 1/4 mm^{-1} < \omega > 1/16 \mu{}m^{-1}')
32
33
34
35
36 function [hsf_height,msf_height] = freq_dom_filt(xdata,
      hdata,hsf_range,msf_range)
37
38 dx = xdata(2)-xdata(1);
39 num_points = length(xdata);
40 hf = fft(hdata);
41 lambda = ((1/dx)*(0:floor(num_points/2))/num_points).^-1;
42
43 % roughness exraction
44 Sf = zeros(size(hf,1),1);
45 k = find(lambda >= hsf_range(1) & lambda <= hsf_range(2));
46 Sf(k) = 1;
```

```
47 hsf_heightf = hf.*Sf;
48 hsf_height = real(ifft(hsf_heightf));
49
50
51 % waviness exraction
52 Sf = zeros(size(hf,1),1);
53 k = find(lambda >= msf_range(1) & lambda <= msf_range(2));
54 Sf(k) = 1;
55 msf_heightf = hf.*Sf;
56 msf_height = real(ifft(msf_heightf));
57 end
58
59 function dt_hdata = dt(xdata,hdata,info,outerposition)
60
61 % detrend data
62 polynomial_order = 4;
63 [p,~,mu] = polyfit(xdata,hdata,polynomial_order);
64 f_y = polyval(p,xdata,[],mu);
65 dt_hdata = hdata - f_y;
66
67 end
```

C.6 Figure 3.6 Fizeau Measurement Data Decomposition

```
clearvars
hsf_range = [1e-6 16e-3]; % range of roughness spatial
   wavelengths [mm]
msf_range = [16e-3 4]; % range of waveiness spatial
   wavelengths [mm]
filename = 's10_back_mrfprocessed_1_dec6_pistontiltremoved
   .datx';

% surface data in fringes
surface = h5read(filename,'/Data/Surface/{AE3FB081-FD1A
   -4740-ABE7-7383615C2442}');
% intensity map
intensity = h5read(filename,'/Data/Intensity/{E7567CF2-8
   B6E-4023-AD80-0C5BE0A9398E}');
%% Measurement info
% number of averages
phase_averages = h5readatt(filename,'/Attributes/{A478AA13
   -3F59-4355-8598-A411B75371D2}','Data Context.Data
   Attributes.Phase Averages');
% wavelength
wavelength = h5readatt(filename,'/Data/Surface/{AE3FB081-
   FD1A-4740-ABE7-7383615C2442}','Wavelength');
% from wavelength to fringes
int_scale_factor = h5readatt(filename,'/Data/Surface/{
   AE3FB081-FD1A-4740-ABE7-7383615C2442}','Interferometric
    Scale Factor');
```

```
17 %% trim and add NaN
18 [n,m] = size(surface);
19 for i = 1:n
20     for j = 1:m
21 if surface(i,j) > 1000
22     surface(i,j) = NaN;
23 else
24     surface(i,j) = surface(i,j);
25 end
26     end
27 end
28 %% convert fringes to mm
29 height = wavelength*int_scale_factor*surface;
30
31 %% change to nm from m
32 height = height * 1e9;
33
34 %% select data along a trace
35 trace = height(:,500);
36 trace_start = find(~isnan(trace),1);
37 trace_end = find(~isnan(trace),1,'last');
38 trace = trace(trace_start:trace_end);
39 trace = trace-mean(trace);
40 xdata = trace_start:trace_end;
41 xdata = xdata/10;
42
43 %% detrend trace
```

```
44 trace_dt = dt(xdata,trace',' ',[0 50 500 500]);
45 [h_rough,h_wav] = freq_dom_filt(xdata,trace_dt',hsf_range,
      msf_range);
46 Rq = sqrt(sum(h_rough.^2)/length(xdata));  % [mm]
47 Wq = sqrt(sum(h_wav.^2)/length(xdata));  % [mm]
48
49 fprintf('Rq =   %0.3f nm      \n',Rq)
50 fprintf('Wq =   %0.3f nm      \n',Wq)
51
52 figure(1);clf
53 subplot(211)
54 plot(xdata-xdata(1),h_rough,'displayname','roughness');
55 xlabel('x, mm');ylabel('height, nm')
56 title('roughness, \omega < 16 \mu{}m')
57 ylim([-30 30])
58 subplot(212)
59 plot(xdata-xdata(1),h_wav,'displayname','waviness')
60 xlabel('x, mm');ylabel('height, nm')
61 title('waviness, 4 mm < \omega > 16 \mu{}m')
62
63 function dt_hdata = dt(xdata,hdata,info,outerposition)
64
65 % detrend data
66 polynomial_order = 4;
67 [p,~,mu] = polyfit(xdata,hdata,polynomial_order);
68 f_y = polyval(p,xdata,[],mu);
69 dt_hdata = hdata - f_y;
```

```
70
71 end
72
73 function [hsf_height,msf_height] = freq_dom_filt(xdata,
      hdata,hsf_range,msf_range)
74
75 dx = xdata(2)-xdata(1);
76 num_points = length(xdata);
77 hf = fft(hdata);
78 lambda = ((1/dx)*(0:floor(num_points/2))/num_points).^-1;
79
80 % roughness exraction
81 Sf = zeros(size(hf,1),1);
82 k = find(lambda >= hsf_range(1) & lambda <= hsf_range(2));
83 Sf(k) = 1;
84 hsf_heightf = hf.*Sf;
85 hsf_height = real(ifft(hsf_heightf));
86
87
88 % waviness exraction
89 Sf = zeros(size(hf,1),1);
90 k = find(lambda >= msf_range(1) & lambda <= msf_range(2));
91 Sf(k) = 1;
92 msf_heightf = hf.*Sf;
93 msf_height = real(ifft(msf_heightf));
94
95 end
```

C.7 Figure 4.21 Externally Reflected and Transmitted Intensity

```
%% Frontmatter
clearvars

h = double(4.135667e-15);   % planck constant [eV*s]
c = double(299792458);      % speed of light [m/s]

%% System Parameters and Material Properties
chi = single(pi/4);         % incident radiation
   polarization
E = double(17400.00);       % source energy [eV]

delta1 = double(1.6021E-06); % refractive index unit
   decrement
% of silicon at 17.4 keV
beta1 = double(8.0730E-09);  % absorption part of
   refractive index
% of silicon at 17.4 eV

n0 = 1;                     % external index of refraction
n1 = 1 - delta1 - 1i*beta1;   % internal index of
   refraction
n2 = 1;                     % inner core index of
   refraction
R_outer = double(1.5);        % object radius [m]
ODD = double(0.200);        % object-detector-distance [m]
beamWidth = 0.001;
```

```
22 sigma = double(1e-9);       % RMS surface roughness [m]
23
24 %% Program Parameters
25 thetaStart = 0;
26 thetaStop = 3*sqrt(2*delta1);
27 nDataPoints = 1e5;
28 theta0 = linspace(thetaStart,thetaStop,nDataPoints);
29
30 onesVec = ones(1,nDataPoints);
31 zerosVec = zeros(1,nDataPoints);
32
33
34 %% Geometry
35 z0 = R_outer*cos(theta0);
36 dz = zeros(1,nDataPoints);
37 dz(2:end) = abs(z0(2:end) - z0(1:end-1));
38
39 theta1 = real(acos(n0/n1*cos(theta0)));
40 pSource = R_outer*[-onesVec; zerosVec; cos(theta0)];
41 pIn = R_outer*[-sin(theta0); zerosVec; cos(theta0)];
42 r0 = pIn - pSource;
43 zd_a = pIn(3,:) + (-pIn(1,:) + ODD*onesVec).*tan(2*theta0)
     ;
44 pd_a = [ODD*onesVec; zerosVec; zd_a];
45 r0dash = pd_a - pIn;
46 r1 = 2*R_outer*sin(theta1).*...
47     [cos(theta0-theta1); zerosVec; sin(theta0-theta1)];
```

```
48 pOut_b = pIn + r1;
49 thetaOut_b = 2*theta0 - 2*theta1;
50 zd_b = pOut_b(3,:) + (ODD*onesVec-pOut_b(1,:)).*tan(
      thetaOut_b);
51 pd_b = [ODD*onesVec; zerosVec; zd_b];
52 r2 = pd_b - pOut_b;
53
54 %% Field Calculations
55 a0 = zeros(1,nDataPoints);
56 a0(R_outer-z0 <= beamWidth) = sqrt(4.5*dz(R_outer-z0 <=
      beamWidth)/beamWidth);
57 A0 = a0.*[-sin(chi)*sin(2*theta0)
58     cos(chi)*onesVec
59     sin(chi)*cos(2*theta0)];
60
61 k = 2*pi*E/h/c;
62 k0 = k*[onesVec; zerosVec; zerosVec];
63 k0dash = k*[cos(2*theta0); zerosVec; sin(2*theta0)];
64 k1 = k*n1/n0*[cos(theta0-theta1); zerosVec; sin(theta0-
      theta1)];
65 k2 = k*[cos(2*theta0-2*theta1); zerosVec; sin(2*theta0-2*
      theta1)];
66
67 Psi01x = (n0*sin(theta1)-n1*sin(theta0))./(n0*sin(theta1)+
      n1*sin(theta0));
68 Psi01y = (n0*sin(theta0)-n1*sin(theta1))./(n0*sin(theta0)+
      n1*sin(theta1));
```

```
69 Psi01 = [Psi01x; Psi01y; -Psi01x];
70
71 E0 = A0.*exp(1i*dot(k0,r0));
72 I0 = dot(E0,E0);
73
74 f_sigma = exp(-4*k*k.*sin(theta0).*sin(theta1)*sigma*sigma
   );
75 E0dash = Psi01.*E0.*exp(1i*dot(k0dash,r0dash)).*sqrt(
   f_sigma);
76 I0dash = dot(E0dash,E0dash);
77
78 Phi01x = 2*n0*sin(theta1)./(n0*sin(theta1)+n1*sin(theta0))
   ;
79 Phi01y = 2*n0*sin(theta0)./(n0*sin(theta0)+n1*sin(theta1))
   ;
80 Phi01z = 2*(n0/n1)*sin(theta0)./((n1/n0)*sin(theta0)+sin(
   theta1));
81 Phi01 = [Phi01x; Phi01y; Phi01z];
82
83 mu = k*beta1;
84 E1 = Phi01.*E0.*exp(1i*dot(k1,r1)).*exp(-mu*R_outer*sin(
   theta1));
85
86 Phi12x = 2*(n1/n0)*sin(theta0)./(sin(theta1)+(n1/n0)*sin(
   theta0));
87 Phi12y = 2*(n1/n0)*sin(theta1)./((n1/n0)*sin(theta1)+sin(
   theta0));
```

```
88  Phi12z = 2*(n1/n0)^2*sin(theta1)./(sin(theta1)+(n1/n0)*sin
       (theta0));
89  Phi12 = [Phi12x; Phi12y; Phi12z];
90
91  E2 = Phi12.*E1.*exp(1i*dot(k2,r2));
92  I2 = dot(E2,E2);
93
94  %% discretize data
95  edges = (0:0.002:2)/1000 + R_outer;
96
97  X = discretize(zd_a,edges);
98  Y = discretize(zd_b,edges);
99
100 Itot_a = zeros(1,length(edges));
101 Itot_b = Itot_a;
102 for ii = 1:length(edges)
103
104 Itot_a(ii) = (sum(I0dash(X==ii),2))*(length(edges)-1);
105 Itot_b(ii) = (sum(I2(Y==ii),2))*(length(edges)-1);
106
107 end
108
109 %% plotting
110
111 figure(1);clf
112 plot((edges-R_outer)*1000,Itot_a,'-k','linewidth',2,...
113     'displayname','Reflected Intensity, I_0''')
```

```
114 set(gca, 'YScale', 'log','FontSize',18)
115 xlabel('Detector Height, mm');ylabel('Normalized Intensity
    ')
116 xlim([0 2]);ylim([1e-5 1e-1])
117 legend show
118
119 figure(1);hold on
120 plot((edges-R_outer)*1000,Itot_b,'--k','linewidth',2,...
121     'displayname','Transmitted Intensity, I_2')
122 figure(1);hold off
```

C.8 Figure 4.22 External Roughness Comparison

```
%% Frontmatter
clearvars

h = double(4.135667e-15);   % planck constant [eV*s]
c = double(299792458);      % speed of light [m/s]

%% System Parameters and Material Properties
chi = single(pi/4);         % incident radiation
   polarization
E = double(17400.00);       % source energy [eV]

delta1 = double(1.6021E-06); % refractive index unit
   decrement
% of silicon at 17.4 keV
beta1 = double(8.0730E-09);  % absorption part of
   refractive index
% of silicon at 17.4 eV

n0 = 1;                     % external index of refraction
n1 = 1 - delta1 - 1i*beta1;   % internal index of
   refraction
n2 = 1;                     % inner core index of
   refraction
R_outer = double(1.5);        % object radius [m]
ODD = double(0.200);        % object-detector-distance [m]
beamWidth = 0.001;
```

```
22 sigma = [0 2 4 10]*1e-9;      % RMS surface roughness [m]
23
24 %% Program Parameters
25 thetaStart = 0;
26 thetaStop = 3*sqrt(2*delta1);
27 nDataPoints = 1e5;
28 theta0 = linspace(thetaStart,thetaStop,nDataPoints);
29
30 onesVec = ones(1,nDataPoints);
31 zerosVec = zeros(1,nDataPoints);
32
33
34 %% Geometry
35 z0 = R_outer*cos(theta0);
36 dz = zeros(1,nDataPoints);
37 dz(2:end) = abs(z0(2:end) - z0(1:end-1));
38
39 theta1 = real(acos(n0/n1*cos(theta0)));
40 pSource = R_outer*[-onesVec; zerosVec; cos(theta0)];
41 pIn = R_outer*[-sin(theta0); zerosVec; cos(theta0)];
42 r0 = pIn - pSource;
43 zd_a = pIn(3,:) + (-pIn(1,:) + ODD*onesVec).*tan(2*theta0)
     ;
44 pd_a = [ODD*onesVec; zerosVec; zd_a];
45 r0dash = pd_a - pIn;
46 r1 = 2*R_outer*sin(theta1).*...
47     [cos(theta0-theta1); zerosVec; sin(theta0-theta1)];
```

```
48 pOut_b = pIn + r1;
49 thetaOut_b = 2*theta0 - 2*theta1;
50 zd_b = pOut_b(3,:) + (ODD*onesVec-pOut_b(1,:)).*tan(
      thetaOut_b);
51 pd_b = [ODD*onesVec; zerosVec; zd_b];
52 r2 = pd_b - pOut_b;
53
54 %% Field Calculations
55 a0 = zeros(1,nDataPoints);
56 a0(R_outer-z0 <= beamWidth) = sqrt(4.5*dz(R_outer-z0 <=
      beamWidth)/beamWidth);
57 A0 = a0.*[-sin(chi)*sin(2*theta0)
58     cos(chi)*onesVec
59     sin(chi)*cos(2*theta0)];
60
61 k = 2*pi*E/h/c;
62 k0 = k*[onesVec; zerosVec; zerosVec];
63 k0dash = k*[cos(2*theta0); zerosVec; sin(2*theta0)];
64 k1 = k*n1/n0*[cos(theta0-theta1); zerosVec; sin(theta0-
      theta1)];
65 k2 = k*[cos(2*theta0-2*theta1); zerosVec; sin(2*theta0-2*
      theta1)];
66
67 Psi01x = (n0*sin(theta1)-n1*sin(theta0))./(n0*sin(theta1)+
      n1*sin(theta0));
68 Psi01y = (n0*sin(theta0)-n1*sin(theta1))./(n0*sin(theta0)+
      n1*sin(theta1));
```

```
69 Psi01 = [Psi01x; Psi01y; -Psi01x];
70
71 E0 = A0.*exp(1i*dot(k0,r0));
72 I0 = dot(E0,E0);
73
74 figure(1);clf
75 lineType = ["-k" "-.k" ":k" "--k"];
76 lineName = ["smooth" "\sigma = 2 nm" "\sigma = 4 nm" "\
      sigma = 10 nm"];
77
78 Phi01x = 2*n0*sin(theta1)./(n0*sin(theta1)+n1*sin(theta0))
      ;
79 Phi01y = 2*n0*sin(theta0)./(n0*sin(theta0)+n1*sin(theta1))
      ;
80 Phi01z = 2*(n0/n1)*sin(theta0)./((n1/n0)*sin(theta0)+sin(
      theta1));
81 Phi01 = [Phi01x; Phi01y; Phi01z];
82
83 mu = k*beta1;
84 E1 = Phi01.*E0.*exp(1i*dot(k1,r1)).*exp(-mu*R_outer*sin(
      theta1));
85
86 Phi12x = 2*(n1/n0)*sin(theta0)./(sin(theta1)+(n1/n0)*sin(
      theta0));
87 Phi12y = 2*(n1/n0)*sin(theta1)./((n1/n0)*sin(theta1)+sin(
      theta0));
```

```
88  Phi12z = 2*(n1/n0)^2*sin(theta1)./(sin(theta1)+(n1/n0)*sin
       (theta0));
89  Phi12 = [Phi12x; Phi12y; Phi12z];
90
91  E2 = Phi12.*E1.*exp(1i*dot(k2,r2));
92  I2 = dot(E2,E2);
93
94  for ii = 1:length(sigma)
95
96      f_sigma = exp(-4*k*k.*sin(theta0).*sin(theta1)*sigma(
           ii)*sigma(ii));
97      E0dash = Psi01.*E0.*exp(1i*dot(k0dash,r0dash)).*sqrt(
           f_sigma);
98      I0dash = dot(E0dash,E0dash);
99
100     %% discretize data
101     edges = (0:0.002:2)/1000 + R_outer;
102
103     X = discretize(zd_a,edges);
104     Y = discretize(zd_b,edges);
105
106     Itot = zeros(1,length(edges));
107     for jj = 1:length(edges)
108
109         Itot(jj) = (sum(I0dash(X==jj),2) + sum(I2(Y==jj)
               ,2))*(length(edges)-1);
110
```

```
111     end
112
113     %% plotting
114
115     figure(1);hold on
116     plot((edges-R_outer)*1000,Itot,lineType(ii),'linewidth
            ',2,...
117          'displayname',lineName(ii))
118     set(gca, 'YScale', 'log','FontSize',18)
119     xlabel('Detector Height, mm');ylabel('Normalized
            Intensity')
120     xlim([0 2]);ylim([1e-5 1e-1])
121     legend show
122     drawnow
123
124 end
125 figure(1);hold off
```

C.9 Figure 4.23 External Radius Comparison

```
%% Frontmatter
clearvars

h = double(4.135667e-15);   % planck constant [eV*s]
c = double(299792458);      % speed of light [m/s]

%% System Parameters and Material Properties
chi = single(pi/4);         % incident radiation
   polarization
E = double(17400.00);       % source energy [eV]

delta1 = double(1.6021E-06); % refractive index unit
   decrement
% of silicon at 17.4 keV
beta1 = double(8.0730E-09);  % absorption part of
   refractive index
% of silicon at 17.4 eV

n0 = 1;                     % external index of refraction
n1 = 1 - delta1 - 1i*beta1;   % internal index of
   refraction
n2 = 1;                     % inner core index of
   refraction
R_outer = [0.5 1 2 4];        % object radius [m]
ODD = double(0.200);        % object-detector-distance [m]
beamWidth = 0.001;
```

```
22 sigma = 1e-9;      % RMS surface roughness [m]
23
24 %% Program Parameters
25 thetaStart = 0;
26 thetaStop = 3*sqrt(2*delta1);
27 nDataPoints = 1e5;
28 theta0 = linspace(thetaStart,thetaStop,nDataPoints);
29
30 onesVec = ones(1,nDataPoints);
31 zerosVec = zeros(1,nDataPoints);
32 figure(1);clf
33 lineType = ["-k" "-.k" ":k" "--k"];
34 lineName = ["Radius: 0.5 m" "Radius: 1 m" "Radius: 2 m" "
      Radius: 4 m"];
35
36 for ii = 1:length(R_outer)
37     %% Geometry
38     z0 = R_outer(ii)*cos(theta0);
39     dz = zeros(1,nDataPoints);
40     dz(2:end) = abs(z0(2:end) - z0(1:end-1));
41
42     theta1 = real(acos(n0/n1*cos(theta0)));
43     pSource = R_outer(ii)*[-onesVec; zerosVec; cos(theta0)
         ];
44     pIn = R_outer(ii)*[-sin(theta0); zerosVec; cos(theta0)
         ];
45     r0 = pIn - pSource;
```

```
46      zd_a = pIn(3,:) + (-pIn(1,:) + ODD*onesVec).*tan(2*
           theta0);
47      pd_a = [ODD*onesVec; zerosVec; zd_a];
48      r0dash = pd_a - pIn;
49      r1 = 2*R_outer(ii)*sin(theta1).*...
50          [cos(theta0-theta1); zerosVec; sin(theta0-theta1)
               ];
51      pOut_b = pIn + r1;
52      thetaOut_b = 2*theta0 - 2*theta1;
53      zd_b = pOut_b(3,:) + (ODD*onesVec-pOut_b(1,:)).*tan(
           thetaOut_b);
54      pd_b = [ODD*onesVec; zerosVec; zd_b];
55      r2 = pd_b - pOut_b;
56
57      %% Field Calculations
58      a0 = zeros(1,nDataPoints);
59      a0(R_outer(ii)-z0 <= beamWidth) = sqrt(4.5*dz(R_outer(
           ii)-z0 <= beamWidth)/beamWidth);
60      A0 = a0.*[-sin(chi)*sin(2*theta0)
61          cos(chi)*onesVec
62          sin(chi)*cos(2*theta0)];
63
64      k = 2*pi*E/h/c;
65      k0 = k*[onesVec; zerosVec; zerosVec];
66      k0dash = k*[cos(2*theta0); zerosVec; sin(2*theta0)];
67      k1 = k*n1/n0*[cos(theta0-theta1); zerosVec; sin(theta0
           -theta1)];
```

```
68      k2 = k*[cos(2*theta0-2*theta1); zerosVec; sin(2*theta0
           -2*theta1)];
69
70      Psi01x = (n0*sin(theta1)-n1*sin(theta0))./(n0*sin(
           theta1)+n1*sin(theta0));
71      Psi01y = (n0*sin(theta0)-n1*sin(theta1))./(n0*sin(
           theta0)+n1*sin(theta1));
72      Psi01 = [Psi01x; Psi01y; -Psi01x];
73
74      E0 = A0.*exp(1i*dot(k0,r0));
75      I0 = dot(E0,E0);
76
77      Phi01x = 2*n0*sin(theta1)./(n0*sin(theta1)+n1*sin(
           theta0));
78      Phi01y = 2*n0*sin(theta0)./(n0*sin(theta0)+n1*sin(
           theta1));
79      Phi01z = 2*(n0/n1)*sin(theta0)./((n1/n0)*sin(theta0)+
           sin(theta1));
80      Phi01 = [Phi01x; Phi01y; Phi01z];
81
82      mu = k*beta1;
83      E1 = Phi01.*E0.*exp(1i*dot(k1,r1)).*exp(-mu*R_outer(ii
           )*sin(theta1));
84
85      Phi12x = 2*(n1/n0)*sin(theta0)./(sin(theta1)+(n1/n0)*
           sin(theta0));
```

```
86      Phi12y = 2*(n1/n0)*sin(theta1)./((n1/n0)*sin(theta1)+
           sin(theta0));
87      Phi12z = 2*(n1/n0)^2*sin(theta1)./(sin(theta1)+(n1/n0)
           *sin(theta0));
88      Phi12 = [Phi12x; Phi12y; Phi12z];
89
90      E2 = Phi12.*E1.*exp(1i*dot(k2,r2));
91      I2 = dot(E2,E2);
92
93      f_sigma = exp(-4*k*k.*sin(theta0).*sin(theta1)*sigma*
           sigma);
94      E0dash = Psi01.*E0.*exp(1i*dot(k0dash,r0dash)).*sqrt(
           f_sigma);
95      I0dash = dot(E0dash,E0dash);
96
97      %% discretize data
98      edges = (0:0.002:2)/1000 + R_outer(ii);
99
100     X = discretize(zd_a,edges);
101     Y = discretize(zd_b,edges);
102
103     Itot = zeros(1,length(edges));
104     for jj = 1:length(edges)
105
106         Itot(jj) = (sum(I0dash(X==jj),2) + sum(I2(Y==jj)
               ,2))*(length(edges)-1);
107
```

```
108     end
109
110     %% plotting
111
112     figure(1);hold on
113     plot((edges-R_outer(ii))*1000,Itot,lineType(ii),'
            linewidth',2,...
114          'displayname',lineName(ii))
115     set(gca, 'YScale', 'log','FontSize',18)
116     xlabel('Detector Height, mm');ylabel('Normalized
            Intensity')
117     xlim([0 2]);ylim([1e-5 1])
118     legend show
119     drawnow
120
121 end
122 figure(1);hold off
```

C.10 Figure 4.24 External Energy Comparison

```
%% Frontmatter
clearvars

h = double(4.135667e-15);   % planck constant [eV*s]
c = double(299792458);      % speed of light [m/s]

%% System Parameters and Material Properties
chi = single(pi/4);         % incident radiation
   polarization
E = [8 10 12 17.4]*1000;       % source energy [eV]

delta1 = double(1.6021E-06); % refractive index unit
   decrement
% of silicon at 17.4 keV
beta1 = double(8.0730E-09);  % absorption part of
   refractive index
% of silicon at 17.4 eV

n0 = 1;                     % external index of refraction
n1 = 1 - delta1 - 1i*beta1;   % internal index of
   refraction
n2 = 1;                     % inner core index of
   refraction
R_outer = 1.5;         % object radius [m]
ODD = double(0.200);        % object-detector-distance [m]
beamWidth = 0.001;
```

```
22 sigma = 1e-9;      % RMS surface roughness [m]
23
24 %% Program Parameters
25 thetaStart = 0;
26 thetaStop = 3*sqrt(2*delta1);
27 nDataPoints = 1e5;
28 theta0 = linspace(thetaStart,thetaStop,nDataPoints);
29
30 onesVec = ones(1,nDataPoints);
31 zerosVec = zeros(1,nDataPoints);
32 figure(1);clf
33 lineType = ["-k" "-.k" ":k" "--k"];
34 lineName = ["Energy: 8.0 keV" "Energy: 10.0 keV"...
35     "Energy: 12.0 keV" "Energy: 17.4 keV"];
36
37
38 %% Geometry
39 z0 = R_outer*cos(theta0);
40 dz = zeros(1,nDataPoints);
41 dz(2:end) = abs(z0(2:end) - z0(1:end-1));
42
43 theta1 = real(acos(n0/n1*cos(theta0)));
44 pSource = R_outer*[-onesVec; zerosVec; cos(theta0)];
45 pIn = R_outer*[-sin(theta0); zerosVec; cos(theta0)];
46 r0 = pIn - pSource;
47 zd_a = pIn(3,:) + (-pIn(1,:) + ODD*onesVec).*tan(2*theta0)
    ;
```

```
48 pd_a = [ODD*onesVec; zerosVec; zd_a];
49 r0dash = pd_a - pIn;
50 r1 = 2*R_outer*sin(theta1).*...
51     [cos(theta0-theta1); zerosVec; sin(theta0-theta1)];
52 pOut_b = pIn + r1;
53 thetaOut_b = 2*theta0 - 2*theta1;
54 zd_b = pOut_b(3,:) + (ODD*onesVec-pOut_b(1,:)).*tan(
      thetaOut_b);
55 pd_b = [ODD*onesVec; zerosVec; zd_b];
56 r2 = pd_b - pOut_b;
57
58 %% Field Calculations
59 a0 = zeros(1,nDataPoints);
60 a0(R_outer-z0 <= beamWidth) = sqrt(4.5*dz(R_outer-z0 <=
      beamWidth)/beamWidth);
61 A0 = a0.*[-sin(chi)*sin(2*theta0)
62     cos(chi)*onesVec
63     sin(chi)*cos(2*theta0)];
64
65 for ii = 1:length(E)
66
67     k = 2*pi*E(ii)/h/c;
68     k0 = k*[onesVec; zerosVec; zerosVec];
69     k0dash = k*[cos(2*theta0); zerosVec; sin(2*theta0)];
70     k1 = k*n1/n0*[cos(theta0-theta1); zerosVec; sin(theta0
          -theta1)];
```

```
71      k2 = k*[cos(2*theta0-2*theta1); zerosVec; sin(2*theta0
           -2*theta1)];
72
73      Psi01x = (n0*sin(theta1)-n1*sin(theta0))./(n0*sin(
           theta1)+n1*sin(theta0));
74      Psi01y = (n0*sin(theta0)-n1*sin(theta1))./(n0*sin(
           theta0)+n1*sin(theta1));
75      Psi01 = [Psi01x; Psi01y; -Psi01x];
76
77      E0 = A0.*exp(1i*dot(k0,r0));
78      I0 = dot(E0,E0);
79
80      Phi01x = 2*n0*sin(theta1)./(n0*sin(theta1)+n1*sin(
           theta0));
81      Phi01y = 2*n0*sin(theta0)./(n0*sin(theta0)+n1*sin(
           theta1));
82      Phi01z = 2*(n0/n1)*sin(theta0)./((n1/n0)*sin(theta0)+
           sin(theta1));
83      Phi01 = [Phi01x; Phi01y; Phi01z];
84
85      mu = k*beta1;
86      E1 = Phi01.*E0.*exp(1i*dot(k1,r1)).*exp(-mu*R_outer*
           sin(theta1));
87
88      Phi12x = 2*(n1/n0)*sin(theta0)./(sin(theta1)+(n1/n0)*
           sin(theta0));
```

```
89      Phi12y = 2*(n1/n0)*sin(theta1)./((n1/n0)*sin(theta1)+
           sin(theta0));
90      Phi12z = 2*(n1/n0)^2*sin(theta1)./(sin(theta1)+(n1/n0)
           *sin(theta0));
91      Phi12 = [Phi12x; Phi12y; Phi12z];
92
93      E2 = Phi12.*E1.*exp(1i*dot(k2,r2));
94      I2 = dot(E2,E2);
95
96      f_sigma = exp(-4*k*k.*sin(theta0).*sin(theta1)*sigma*
           sigma);
97      E0dash = Psi01.*E0.*exp(1i*dot(k0dash,r0dash)).*sqrt(
           f_sigma);
98      I0dash = dot(E0dash,E0dash);
99
100     %% discretize data
101     edges = (0:0.002:2)/1000 + R_outer;
102
103     X = discretize(zd_a,edges);
104     Y = discretize(zd_b,edges);
105
106     Itot = zeros(1,length(edges));
107     for jj = 1:length(edges)
108
109         Itot(jj) = (sum(I0dash(X==jj),2) + sum(I2(Y==jj)
               ,2))*(length(edges)-1);
110
```

```
111     end
112
113     %% plotting
114
115     figure(1);hold on
116     plot((edges-R_outer)*1000,Itot,lineType(ii),'linewidth
            ',2,...
117          'displayname',lineName(ii))
118     set(gca, 'YScale', 'log','FontSize',18)
119     xlabel('Detector Height, mm');ylabel('Normalized
            Intensity')
120     xlim([0 2]);ylim([1e-5 1e-1])
121     legend show
122     drawnow
123
124 end
125 figure(1);hold off
```

C.11 Figure 4.28 Shell Thickness Comparison

```
%% Frontmatter
clearvars

h = double(4.135667e-15);   % planck constant [eV*s]
c = double(299792458);      % speed of light [m/s]

%% System Parameters and Material Properties
chi = single(pi/4);         % incident radiation
   polarization
E = 17400;       % source energy [eV]

delta1 = double(1.6021E-06); % refractive index unit
   decrement
% of silicon at 17.4 keV
beta1 = double(8.0730E-09);  % absorption part of
   refractive index
% of silicon at 17.4 eV

n0 = 1;                     % external index of refraction
n1 = 1 - delta1 - 1i*beta1;   % internal index of
   refraction
n2 = 1;                     % inner core index of
   refraction
R_outer = double(1);        % object radius [m]
shellThickness = [0 10 100 1000]*1e-9;
R_inner = R_outer - shellThickness;
```

```
22 ODD = double(0.200);          % object-detector-distance [m]
23 beamWidth = 0.001;
24 sigma = double(1e-9);        % RMS surface roughness [m]
25 sigma2 = double(1e-9);
26
27 %% Program Parameters
28 thetaStart = 0;
29 thetaStop = 3*sqrt(2*delta1);
30 nDataPoints = 1e5;
31 theta0 = linspace(thetaStart,thetaStop,nDataPoints);
32 offset = [1 10 100 1000];
33
34 onesVec = ones(1,nDataPoints);
35 zerosVec = zeros(1,nDataPoints);
36 figure(1);clf
37 lineType = ["-k" "-.k" ":k" "--k"];
38 lineName = ["Shell Thickness: 0 nm" "Shell Thickness: 10
      nm"...
39     "Shell Thickness: 100 nm" "Shell Thickness: 1000 nm"];
40
41 for ii = 1:length(R_inner)
42     %% Geometry
43     z0 = R_outer*cos(theta0);
44     dz = zeros(1,nDataPoints);
45     dz(2:end) = abs(z0(2:end) - z0(1:end-1));
46
47     theta1 = real(acos(n0/n1*cos(theta0)));
```

```
48      theta_c = real(acos(n1/n2*R_outer/R_inner(ii)));
49      theta4 = real(acos(R_outer/R_inner(ii)*cos(theta1)));
50      theta5 = real(acos(n1/n0*cos(theta4)));
51      theta6 = real(acos(R_inner(ii)/R_outer*cos(theta4)));
52      theta7 = real(acos(n1/n0*cos(theta6)));
53      pSource = R_outer*[-onesVec; zerosVec; cos(theta0)];
54      pIn = R_outer*[-sin(theta0); zerosVec; cos(theta0)];
55      r0 = pIn - pSource;
56      zd_a = pIn(3,:) + (-pIn(1,:) + ODD*onesVec).*tan(2*
           theta0);
57      pd_a = [ODD*onesVec; zerosVec; zd_a];
58      r0dash = pd_a - pIn;
59      r1 = 2*R_outer*sin(theta1).*...
60          [cos(theta0-theta1); zerosVec; sin(theta0-theta1)
               ];
61      pOut_b = pIn + r1;
62      thetaOut_b = 2*theta0 - 2*theta1;
63      zd_b = pOut_b(3,:) + (ODD*onesVec-pOut_b(1,:)).*tan(
           thetaOut_b);
64      pd_b = [ODD*onesVec; zerosVec; zd_b];
65      r2 = pd_b - pOut_b;
66      r3 = R_inner(ii)*sin(theta1-theta4)./cos(theta1).*...
67          [cos(theta0-theta1); zerosVec; sin(theta0-theta1)
               ];
68      r3dash = R_inner(ii)*sin(theta6-theta4)./cos(theta6).*
           ...
```

```
69          [cos(theta0-theta1+2*theta4); zerosVec; sin(theta0
               -theta1+2*theta4)];
70      thetaOut_c = theta0-theta1+2*theta4+theta7-theta6;
71      pOut_c = pIn + r3 + r3dash;
72      zd_c = pOut_c(3,:)+(ODD-pOut_c(1,:)).*tan(thetaOut_c);
73      pd_c = [ODD*onesVec; zerosVec; zd_c];
74      r5 = pd_c - pOut_c;
75
76      %% Field Calculations
77      a0 = zeros(1,nDataPoints);
78      a0(R_outer-z0 <= beamWidth) = sqrt(4.5*dz(R_outer-z0
           <= beamWidth)/beamWidth);
79      A0 = a0.*[-sin(chi)*sin(2*theta0)
80          cos(chi)*onesVec
81          sin(chi)*cos(2*theta0)];
82
83
84      k = 2*pi*E/h/c;
85      k0 = k*[onesVec; zerosVec; zerosVec];
86      k0dash = k*[cos(2*theta0); zerosVec; sin(2*theta0)];
87      k1 = k*n1/n0*[cos(theta0-theta1); zerosVec; sin(theta0
           -theta1)];
88      k2 = k*[cos(2*theta0-2*theta1); zerosVec; sin(2*theta0
           -2*theta1)];
89      k3dash = k*n1/n0*[cos(2*theta4); zerosVec; sin(2*
           theta4)];
90      k5 = k*[cos(thetaOut_c); zerosVec; sin(thetaOut_c)];
```

```
91
92      Psi01x = (n0*sin(theta1)-n1*sin(theta0))./(n0*sin(
           theta1)+n1*sin(theta0));
93      Psi01y = (n0*sin(theta0)-n1*sin(theta1))./(n0*sin(
           theta0)+n1*sin(theta1));
94      Psi01 = [Psi01x; Psi01y; -Psi01x];
95
96      E0 = A0.*exp(1i*dot(k0,r0));
97      I0 = dot(E0,E0);
98
99      f_sigma = exp(-4*k*k.*sin(theta0).*sin(theta1)*sigma*
           sigma);
100     E0dash = Psi01.*E0.*exp(1i*dot(k0dash,r0dash)).*sqrt(
           f_sigma);
101     I0dash = dot(E0dash,E0dash);
102
103     Phi01x = 2*n0*sin(theta1)./(n0*sin(theta1)+n1*sin(
           theta0));
104     Phi01y = 2*n0*sin(theta0)./(n0*sin(theta0)+n1*sin(
           theta1));
105     Phi01z = 2*(n0/n1)*sin(theta0)./((n1/n0)*sin(theta0)+
           sin(theta1));
106     Phi01 = [Phi01x; Phi01y; Phi01z];
107
108     mu = k*beta1;
109     E1 = Phi01.*E0.*exp(1i*dot(k1,r1)).*exp(-mu*R_outer*
           sin(theta1));
```

```
110
111     Phi12x = 2*(n1/n0)*sin(theta0)./(sin(theta1)+(n1/n0)*
           sin(theta0));
112     Phi12y = 2*(n1/n0)*sin(theta1)./((n1/n0)*sin(theta1)+
           sin(theta0));
113     Phi12z = 2*(n1/n0)^2*sin(theta1)./(sin(theta1)+(n1/n0)
           *sin(theta0));
114     Phi12 = [Phi12x; Phi12y; Phi12z];
115
116     E2 = Phi12.*E1.*exp(1i*dot(k2,r2));
117     I2 = dot(E2,E2);
118
119     E3 = Phi01.*E0.*exp(1i*dot(k1,r3)).*...
120         exp(-mu*R_inner(ii)*sin(theta1-theta4)./cos(theta1
               )/2);
121
122     Psi34x = (n1*sin(theta5)-n2*sin(theta4))./(n1*sin(
           theta4)+n2*sin(theta5));
123     Psi34y = (n1*sin(theta4)-n2*sin(theta5))./(n1*sin(
           theta4)+n2*sin(theta5));
124     Psi34 = [Psi34x; Psi34y; -Psi34x];
125
126     f_sigma2 = exp(-4*k*k.*sin(theta4).*sin(theta5)*sigma2
           *sigma2);
127     E3dash = Psi34.*E3.*exp(1i*dot(k3dash,r3dash)).*...
128         exp(-mu*R_inner(ii)*sin(theta6-theta4)./cos(theta6
               )/2).*...
```

```
129         sqrt(f_sigma2);
130
131     Phi3dash5x = 2*n1*sin(theta7)./(n0*sin(theta6)+n1*sin(
            theta7));
132     Phi3dash5y = 2*n1*sin(theta6)./(n1*sin(theta6)+n0*sin(
            theta7));
133     Phi3dash5z = 2*(n1/n0)^2*sin(theta6)./(sin(theta6)+(n1
            /n0)*sin(theta7));
134     Phi3dash5 = [Phi3dash5x; Phi3dash5y; Phi3dash5z];
135
136     E5 = Phi3dash5.*E3dash.*exp(1i*dot(k5,r5));
137     I5 = dot(E5,E5);
138
139     %% discretize data
140     edges = (0:0.002:2)/1000 + R_outer;
141
142     X = discretize(zd_a,edges);
143     Y = discretize(zd_b,edges);
144     Z = discretize(zd_c,edges);
145
146     Itot = zeros(1,length(edges));
147     for jj = 1:length(edges)
148
149         Itot(jj) = (sum(I0dash(X==jj),2) + sum(I2(Y==jj)
                ,2) + sum(I5(Z==jj),2))*...
150         (length(edges)-1);
151     end
```

```
152
153     %% plotting
154
155     figure(1);hold on
156     plot((edges-R_outer)*1000,Itot*offset(ii),lineType(ii)
            ,'linewidth',2,...
157          'displayname',lineName(ii))
158     set(gca, 'YScale', 'log','FontSize',18)
159     xlabel('Detector Height, mm');ylabel('Normalized
            Intensity')
160     xlim([0 2]);ylim([1e-5 1e2])
161     legend show
162     drawnow
163
164 end
165
166 figure(1);hold off
```

C.12 Figure 4.29 Internal Roughness Comparison

```
%% Frontmatter
clearvars

h = double(4.135667e-15);   % planck constant [eV*s]
c = double(299792458);      % speed of light [m/s]

%% System Parameters and Material Properties
chi = single(pi/4);         % incident radiation
   polarization
E = 17400;       % source energy [eV]

delta1 = double(1.6021E-06); % refractive index unit
   decrement
% of silicon at 17.4 keV
beta1 = double(8.0730E-09);  % absorption part of
   refractive index
% of silicon at 17.4 eV

n0 = 1;                     % external index of refraction
n1 = 1 - delta1 - 1i*beta1;   % internal index of
   refraction
n2 = 1;                     % inner core index of
   refraction
R_outer = double(1);        % object radius [m]
shellThickness = 10e-9;
R_inner = R_outer - shellThickness;
```

```
22 ODD = double(0.200);          % object-detector-distance [m]
23 beamWidth = 0.001;
24 sigma = double(1e-9);        % RMS surface roughness [m]
25 sigma2 = [1 2 5 10]*1e-9;
26
27 %% Program Parameters
28 thetaStart = 0;
29 thetaStop = 3*sqrt(2*delta1);
30 nDataPoints = 1e5;
31 theta0 = linspace(thetaStart,thetaStop,nDataPoints);
32 offset = [1 10 100 1000];
33
34 onesVec = ones(1,nDataPoints);
35 zerosVec = zeros(1,nDataPoints);
36 figure(1);clf
37 lineType = ["-k" "-.k" ":k" "--k"];
38 lineName = ["\sigma_2 = 1 nm" "\sigma_2 = 2 nm" "\sigma_2
      = 5 nm"...
39     "\sigma_2 = 10 nm"];
40
41 %% Geometry
42 z0 = R_outer*cos(theta0);
43 dz = zeros(1,nDataPoints);
44 dz(2:end) = abs(z0(2:end) - z0(1:end-1));
45
46 theta1 = real(acos(n0/n1*cos(theta0)));
47 theta_c = real(acos(n1/n2*R_outer/R_inner));
```

```
theta4 = real(acos(R_outer/R_inner*cos(theta1)));
theta5 = real(acos(n1/n0*cos(theta4)));
theta6 = real(acos(R_inner/R_outer*cos(theta4)));
theta7 = real(acos(n1/n0*cos(theta6)));
pSource = R_outer*[-onesVec; zerosVec; cos(theta0)];
pIn = R_outer*[-sin(theta0); zerosVec; cos(theta0)];
r0 = pIn - pSource;
zd_a = pIn(3,:) + (-pIn(1,:) + ODD*onesVec).*tan(2*theta0)
   ;
pd_a = [ODD*onesVec; zerosVec; zd_a];
r0dash = pd_a - pIn;
r1 = 2*R_outer*sin(theta1).*...
    [cos(theta0-theta1); zerosVec; sin(theta0-theta1)];
pOut_b = pIn + r1;
thetaOut_b = 2*theta0 - 2*theta1;
zd_b = pOut_b(3,:) + (ODD*onesVec-pOut_b(1,:)).*tan(
   thetaOut_b);
pd_b = [ODD*onesVec; zerosVec; zd_b];
r2 = pd_b - pOut_b;
r3 = R_inner*sin(theta1-theta4)./cos(theta1).*...
    [cos(theta0-theta1); zerosVec; sin(theta0-theta1)];
r3dash = R_inner*sin(theta6-theta4)./cos(theta6).*...
    [cos(theta0-theta1+2*theta4); zerosVec; sin(theta0-
       theta1+2*theta4)];
thetaOut_c = theta0-theta1+2*theta4+theta7-theta6;
pOut_c = pIn + r3 + r3dash;
zd_c = pOut_c(3,:)+(ODD-pOut_c(1,:)).*tan(thetaOut_c);
```

```
72 pd_c = [ODD*onesVec; zerosVec; zd_c];
73 r5 = pd_c - pOut_c;
74
75 %% Field Calculations
76 a0 = zeros(1,nDataPoints);
77 a0(R_outer-z0 <= beamWidth) = sqrt(4.5*dz(R_outer-z0 <=
      beamWidth)/beamWidth);
78 A0 = a0.*[-sin(chi)*sin(2*theta0)
79     cos(chi)*onesVec
80     sin(chi)*cos(2*theta0)];
81
82
83 k = 2*pi*E/h/c;
84 k0 = k*[onesVec; zerosVec; zerosVec];
85 k0dash = k*[cos(2*theta0); zerosVec; sin(2*theta0)];
86 k1 = k*n1/n0*[cos(theta0-theta1); zerosVec; sin(theta0-
      theta1)];
87 k2 = k*[cos(2*theta0-2*theta1); zerosVec; sin(2*theta0-2*
      theta1)];
88 k3dash = k*n1/n0*[cos(2*theta4); zerosVec; sin(2*theta4)];
89 k5 = k*[cos(thetaOut_c); zerosVec; sin(thetaOut_c)];
90
91 Psi01x = (n0*sin(theta1)-n1*sin(theta0))./(n0*sin(theta1)+
      n1*sin(theta0));
92 Psi01y = (n0*sin(theta0)-n1*sin(theta1))./(n0*sin(theta0)+
      n1*sin(theta1));
93 Psi01 = [Psi01x; Psi01y; -Psi01x];
```

```
94
95  E0 = A0.*exp(1i*dot(k0,r0));
96  I0 = dot(E0,E0);
97
98  f_sigma = exp(-4*k*k.*sin(theta0).*sin(theta1)*sigma*sigma
       );
99  E0dash = Psi01.*E0.*exp(1i*dot(k0dash,r0dash)).*sqrt(
       f_sigma);
100 I0dash = dot(E0dash,E0dash);
101
102 Phi01x = 2*n0*sin(theta1)./(n0*sin(theta1)+n1*sin(theta0))
       ;
103 Phi01y = 2*n0*sin(theta0)./(n0*sin(theta0)+n1*sin(theta1))
       ;
104 Phi01z = 2*(n0/n1)*sin(theta0)./((n1/n0)*sin(theta0)+sin(
       theta1));
105 Phi01 = [Phi01x; Phi01y; Phi01z];
106
107 mu = k*beta1;
108 E1 = Phi01.*E0.*exp(1i*dot(k1,r1)).*exp(-mu*R_outer*sin(
       theta1));
109
110 Phi12x = 2*(n1/n0)*sin(theta0)./(sin(theta1)+(n1/n0)*sin(
       theta0));
111 Phi12y = 2*(n1/n0)*sin(theta1)./((n1/n0)*sin(theta1)+sin(
       theta0));
```

```
112 Phi12z = 2*(n1/n0)^2*sin(theta1)./(sin(theta1)+(n1/n0)*sin
    (theta0));
113 Phi12 = [Phi12x; Phi12y; Phi12z];
114
115 E2 = Phi12.*E1.*exp(1i*dot(k2,r2));
116 I2 = dot(E2,E2);
117
118 E3 = Phi01.*E0.*exp(1i*dot(k1,r3)).*...
119     exp(-mu*R_inner*sin(theta1-theta4)./cos(theta1)/2);
120
121 Psi34x = (n1*sin(theta5)-n2*sin(theta4))./(n1*sin(theta4)+
    n2*sin(theta5));
122 Psi34y = (n1*sin(theta4)-n2*sin(theta5))./(n1*sin(theta4)+
    n2*sin(theta5));
123 Psi34 = [Psi34x; Psi34y; -Psi34x];
124
125 for ii = 1:length(sigma2)
126
127     f_sigma2 = exp(-4*k*k.*sin(theta4).*sin(theta5)*sigma2
        (ii)*sigma2(ii));
128     E3dash = Psi34.*E3.*exp(1i*dot(k3dash,r3dash)).*...
129         exp(-mu*R_inner*sin(theta6-theta4)./cos(theta6)/2)
            .*...
130         sqrt(f_sigma2);
131
132     Phi3dash5x = 2*n1*sin(theta7)./(n0*sin(theta6)+n1*sin(
        theta7));
```

```
133     Phi3dash5y = 2*n1*sin(theta6)./(n1*sin(theta6)+n0*sin(
           theta7));
134     Phi3dash5z = 2*(n1/n0)^2*sin(theta6)./(sin(theta6)+(n1
           /n0)*sin(theta7));
135     Phi3dash5 = [Phi3dash5x; Phi3dash5y; Phi3dash5z];
136
137     E5 = Phi3dash5.*E3dash.*exp(1i*dot(k5,r5));
138     I5 = dot(E5,E5);
139
140     %% discretize data
141     edges = (0:0.002:2)/1000 + R_outer;
142
143     X = discretize(zd_a,edges);
144     Y = discretize(zd_b,edges);
145     Z = discretize(zd_c,edges);
146
147     Itot = zeros(1,length(edges));
148     for jj = 1:length(edges)
149
150         Itot(jj) = (sum(I0dash(X==jj),2) + sum(I2(Y==jj)
               ,2) + sum(I5(Z==jj),2))*...
151         (length(edges)-1);
152     end
153
154     %% plotting
155
156     figure(1);hold on
```

```
157     plot((edges-R_outer)*1000,Itot,lineType(ii),'linewidth
           ',2,...
158          'displayname',lineName(ii))
159     set(gca, 'YScale', 'log','FontSize',18)
160     xlabel('Detector Height, mm');ylabel('Normalized
           Intensity')
161     xlim([0 2]);ylim([1e-4 1e-1])
162     legend show
163     drawnow
164
165 end
166
167 figure(1);hold off
```